國 立 交 通 大 學

電子工程學系

電子研究所

碩 士 論 文

以金為基礎的奈米尺度超常介質之光學性質探討

Optical Studies of Au-based Meta-materials on Nano-scale

研 究 生 ：吳旻蓁 Min-chen Wu

指導教授 ：倪衛新 博士 Prof. Wei-xi Ni

中華民國 九十七 年 七 月

以金為基礎的奈米尺度超常介質之光學性質探討

Optical Studies of Au-based Meta-materials on Nano-scale

研 究 生：吳旻蓁　　Min-chen Wu
指導教授：倪衛新 博士　　Prof. Wei-xi Ni

國 立 交 通 大 學
電子工程學系
電子研究所

碩 士 論 文

A Thesis

Submitted to Department of Electronics Engineering & Institute of Electronics
College of Electrical and Computer Engineering
National Chiao Tung University
In Partial Fulfillment of the Requirements
For the Degree of Master
In
Electronics Engineering
July 2008
Hsinchu, Taiwan, Republic of China
中華民國九十七年七月

以金為基礎的奈米尺度超常介質之光學性質探討

研 究 生：吳旻蓁　　指導教授：倪衛新 博士

國立交通大學

電子工程學系　電子研究所碩士班

摘 要

超常介質是週期性金屬結構，具有電漿子共振、人工磁性以及左手特性等，分別對應到某特定波長的電磁波在金屬陣列中傳遞時，材料所呈現的負導電係數(ε)、負導磁係數(μ)，及由此而造成的負折射率現象。

本論文利用電子束微影和舉離技術，成功地在玻璃上製造了線寬120至360奈米等級的三種金基共振還陣列：單裂隙共振環(split ring resonator, SRR)、無裂隙共振環(closed ring resonator, CRR)以及雙裂隙共振環(2-cut split ring resonator, 2-cut SRR)，圖形陣列面積大約是$90\times90\mu m^2$。傅式光學轉換紅外線光譜儀(FTIR)被用於研究超常介質所產生的光學性質。圖形尺度與電性共振頻率的關係，以及裂隙相對於電場的方位對三種共振環反射光譜的影響在本論文中被探討和比較。

Optical Studies of Au-based Meta-materials on Nano-scale

Student: Min-chen Wu Advisor: Prof. Wei-xi Ni

Department of Electronics Engineering
& Institute of Electronics
National Chiao Tung University

ABSTRACT

Meta-materials are periodic metal structures exhibiting plasmonic resonance, artificial magnetism, and/or left-handed behaviors, which correspond to negative values of permittivity (ε), permeability (μ), and consequent refraction index (n), when electromagnetic (EM) waves propagate in these patterned arrays at a certain range of wavelengths.

By using e-beam lithography and lift-off technique, three types of gold ring resonators with line width 120-360 nm were fabricated on glass. The area of the patterned array was about $90\times90\mu m^2$. Fourier transfer infrared spectroscopy (FTIR) measurements were engaged for the study of optical properties of these meta-material structures. The properties of the electric resonance, such as scaling, were observed. The influence of the orientation of the ring resonators with respect to the incident electric field on the reflection spectra were also compared among different ring resonator structures.

Acknowledgement

I would like to show my deepest appreciation to my advisors, Dr. Wei-xi Ni, for his guidance and support on my research and life. I would also like to thank Dr. Min-Hsiung Shih, Dr. Shih-Ying Hsu, Pei-Hsuan Han, Shih-Kuo Tsai, Ting-Yi Chung, Ching-Hsien Chen, Chien-Hua Chen, Yu-Lin Yang, Shih-Hung Chen, and Chin-Tsai Hsu, who assisted me in various ways in solving problems during my thesis work. Finally, I want to express my sincere gratitude for my parents, and my best friend, Chi-Chieh Huang. Without them, I would not be able to overcome the challenges I encountered.

Contents

List of Table

List of Figure

Chapter 1

Introduction

For a finite slab of continuous material, the complex transmission coefficient $\boldsymbol{T}$ and reflection coefficient $\boldsymbol{R}$ are directly related to the refractive index n and impedance z associated with the slab, which can in turn be expressed in terms of permittivity ε and permeability μ:

$$n = \sqrt{\varepsilon\mu} \tag{1.1}$$

$$z = \sqrt{\frac{\mu}{\varepsilon}} \tag{1.2}$$

Thus, ε and μ are often extracted from the experimentally measured refractive index data, and their frequency (or wavelength) dependence is studied using light transmission and reflection spectra.

Electric ε and magnetic μ characterize the macroscopic response of a homogeneous medium to the applied electric and magnetic fields. These are macroscopic parameters because one usually seeks time or spatial response that is averaged over sufficiently long time or sufficiently large space. Therefore only frequency components of the individual (atomic or molecular) resonators driven by the external fields survive in macroscopic measurements. The concept can be extended to inhomogeneous materials if the domain size is much smaller than the wavelength of radiation. The radiation does not necessarily resolve the individual mesostructures, but responds to the macroscopic resonances of the structure. Such materials are called metamaterials, and can be characterized by macroscopic parameters like homogeneous materials.

Usually, optical materials have positive values of ε and μ. Although it was realized that the refractive index would have to be a complex quantity to account for absorption, or even a tensor to describe anisotropic behavior of materials, the question of the sign of the refractive index did not arise. According to the Maxwell's equation for a planar harmonic wave $e^{i(k\cdot r-\omega t)}$:

$$k \times E = \omega \mu_0 \mu H \tag{1.3}$$

$$k \times H = -\omega \varepsilon_0 E \tag{1.4}$$

where ***k*** is the wave vector, ***E*** and ***H*** are the electric and magnetic fields respectively. Using the definition $k = (n\omega / c)\hat{n}$, where $\hat{n}$ is the unit vector along $E \times H$, it appears that the refractive index n with Re(ε)<0 and Re(μ)<0 is also negative. Such materials permit wave to propagate while wave in media with only Re(ε)<0 or Re(μ)<0 decays since k^2<0. Note that in the case of DNGs (double negative metamaterials), the Poynting vector ($S = E \times H$ (W/m^2), representing the energy flux) and the wave vector are anti-parallel. Figure 1-1 shows the four quadrants in the Re(ε)-Re(μ) plane into which we can conveniently classify electromagnetic (EM) materials. The behavior of wave in each of the quadrants is qualitatively different: materials in the first quadrant allow usual right-handed (RH) propagating waves; materials in the second and fourth quadrants do not allow propagating waves inside them; and DNGs in the third quadrant allow "left-handed" (LH) propagating waves.

Metamaterials have recently received a considerable amount of academic attentions owing to their unusual EM properties and promising applications. In 1968, Veselago first introduced the term "left-handed materials (LHMs)" [2]. He suggested that in a medium which the permittivity ε and permeability μ are simultaneously negative, the EM waves would propagate in a direction opposite to that of the energy. In this case, the electric field ***E***, the magnetic field ***H***, and the wave vector ***k*** form a left-handed

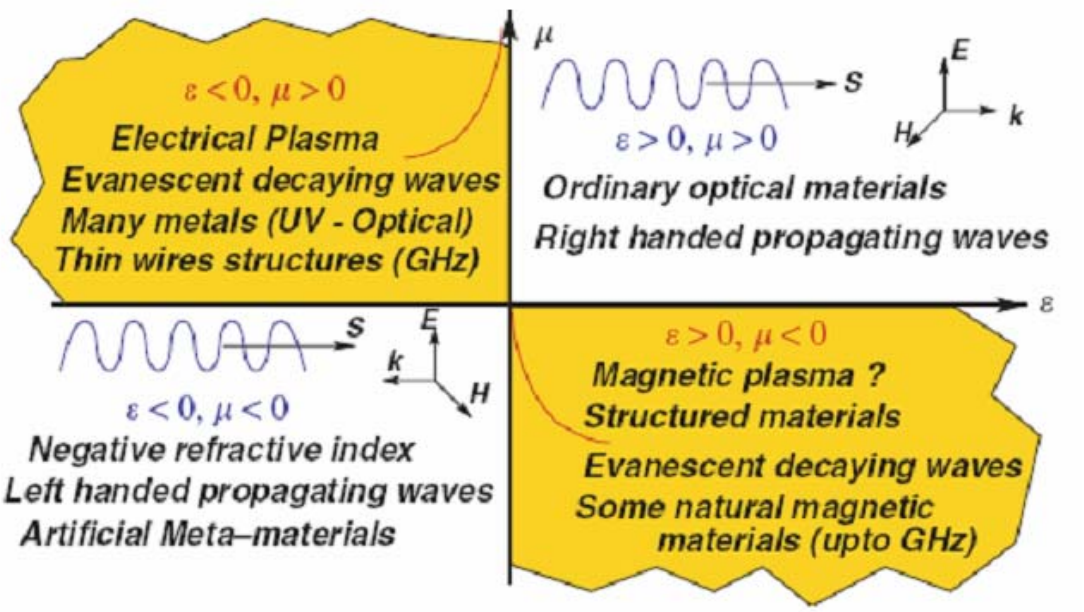

Figure 1-1 A schematic presentation of material classification based on the dielectric and magnetic properties. The wavy lines in quadrants 1 and 3 represent that these materials allow propagating waves, the axes show the right- and left-handed nature of ***E***, ***H***, and ***k***, and *S* is the Poynting vector. In quadrants 2 and 4, waves decay exponentially inside the materials. The figure is imaged from [1].

coordinate system, so the name LHMs has been used to describe these materials. LHMs exhibit reversal of Doppler effects and Cerenkov radiation, and negative refractive index, which would enable some interesting applications such as flat lens focusing and super resolution optics, which breaks the diffraction limit [3].

A negative permittivity is not unusual, and occurs in any metal from zero to the plasma frequency. However, a large magnetic response, in general, and a negative permeability at optical frequency, in particular, does not occur in natural materials. Usual ferromagnetic and antiferromagnetic resonances tend to die out above GHz frequencies, thus one can safely assume that the magnetic permeability of optical materials is unity [4]. The interest in the Veselago's work was renewed when Pendry *et al.* proposed in 1999 an artificial material consisting of the so-called split-ring resonators (SRRs), which respond strongly to an incident magnetic field resulting in negative permeability near the magnetic resonance frequency, and thin metallic wire,

which provide negative permittivity below the cutoff plasma frequency [5]. D. R. Smith *et al.* fabricated the first composite metamaterials (CMM) of SRRs and wires in alternating layers operated at GHz frequencies (the microwave region) in 2000 [6]. Since then, various CMM samples were prepared and shown to exhibit a pass band in which it was assumed that ε and μ were both negative, indicating the existence of media with a negative refractive index.

The realization of negative refractive index media made a great impact on the scientific community, and resulted in the discovery of various novel aspects of left-handed electromagnetism. Efforts are made through analytical modeling, numerical simulations, and experimental studies, especially on SRR to push the operating frequency of metamaterials into the THz region and ultimately to reach optical frequencies. Typically, the occurrence of a CMM pass band within the stop bands of the SRR and wire structures alone was taken as an evidence of the LH behavior. Later this has been proven not always being the case due to the fact that SRR exhibits both electric and magnetic response. Furthermore, there have been experimental verifications of the negative refractive index using Snell's law [7, 8]. The transmission and reflection data can also be calculated using the transfer matrix method for a finite length of metamaterial which a retrieval procedure [9, 10, 11] could be applied to obtain the effective metamaterial parameters ε and μ, under an assumption that it can be treated as homogeneous. Using these analytical expressions one is able to reproduce the low frequency transmission $\boldsymbol{T}$ and reflection $\boldsymbol{R}$, characteristics of LHMs. Even the minor details in $\boldsymbol{T}$ and $\boldsymbol{R}$ observed in the simulations can be analytically explained. This procedure confirmed [12] that a medium composed of SRRs and wires could indeed be characterized by effective ε and μ with negative real parts over a finite frequency band, and its refractive index also has a negative real part.

This thesis work is organized as follow: In Chapter 2, basic theories of the ring resonators are introduced. In Chapter 3, detailed design concepts of the nano-scaled ring resonators are indicated. In Chapter 4, fabrication process and results are presented. In Chapter 5, optical measurement process, data analysis and the spectral result are discussed. And in Chater6, a brief conclusion and future work is given.

Chapter 2

Theory of Metamaterials

Periodically arranged thin metallic wire structures on a sub-wavelength scale are shown to exhibit the plasma frequency ω_p in the microwave regime, below which the material is opaque [13] and the permittivity is considered to be negative.

Split-ring resonators (SRRs) are the main elements used to generate negative permeability. The original form of SRR proposed by Pendry *et al*. [5] consists of two concentric rings separated by a gap, both of which have one split at the opposite sides as shown in Figure 2-1. As scaling down, single-ring SRRs are used instead of double-ring structures for ease of fabrication and reduction of the capacitance. Moreover, SRRs with two or four splits are designed for the sake of symmetric resonator to remove the electric coupling effect. Regardless of the changes in geometry, the SRRs remain a basic form. The key for SRR to exhibit magnetic resonance is the capacitance of the air gap and the inductance of the metallic loop.

In the following sections, we introduce magnetic and electric response of SRR and ways to identify these two responses. Higher order excitation modes of SRR are also shown. And then we discuss the properties of CMM as well as other possible structures generating negative μ or even n.

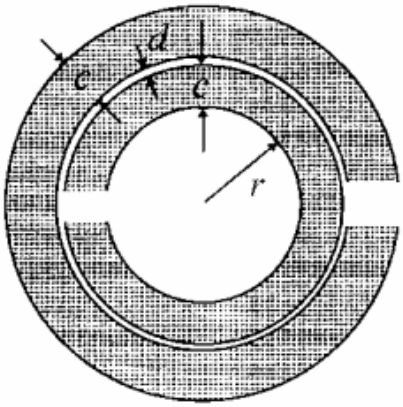

Figure 2-1 Plan view of a conventional double-ring SRR. The figure is imaged from [5].

2.1 Magnetic Response of SRR

The magnetic response of SRR is typically considered a LC resonance with frequency $\omega_{LC} = (L_T C_T)^{-\frac{1}{2}}$, where L_T is the total inductance formed by combination of L_{ring}, the self-inductance of the rectangular SRR loop, and L_{mutual}, the mutual inductance formed between the conductive arms of neighboring SRR elements. An equation describing the self-inductance of a complete rectangular loop made from rectangular cross section wire is given by [14]:

$$L_{ring} = 0.2\mu_0(-\frac{w}{2}\sinh^{-1}1 + \frac{w}{2}\sqrt{2} + (l-\frac{w}{2}) \times \sinh^{-1}(\frac{1-\frac{w}{2}}{\frac{w}{2}}) - \sqrt{(l-\frac{w}{2})^2 + (\frac{w}{2})^2})H \quad (2.1)$$

while the equation for the mutual inductance of two parallel rectangular conductors is given by [15]:

$$L_{mutual} = 0.2l(\ln(\frac{1}{d} + \sqrt{1+\frac{l^2}{d^2}}) - \sqrt{1+\frac{d^2}{l^2}} + \frac{d}{l})\mu H \quad (2.2)$$

where l is the length of the SRR element, w is the width of the wire forming the SRR, and d is the centre-to-centre separation between the arms of adjacent SRR elements.

In order to calculate the total capacitance of the SRR element C_T, it is necessary to

take into account the parallel plate and co-planar capacitances formed by the gap in the SRR structure and between any two individual SRR elements. The parallel plate capacitance can be simply taken as $C = \varepsilon_0 \varepsilon_r \frac{A}{d}$, while the general form of the equation for the co-planar capacitance per unit length for two metal strips of width *p*, separated by distance *q*, is given by [16]:

$$C_{cp} = \frac{(\varepsilon_r + 1)\varepsilon_0}{2} \frac{1}{\pi} \ln(2 \frac{1+\sqrt{k'}}{1-\sqrt{k'}}) \quad \text{F/m} \tag{2.3}$$

where *k'* is a geometrical factor given by: $k' = \sqrt{1 - (\frac{p}{p+2q})^2}$.

2.1.1 Geometric Parameters and Tunable SRR

Since the magnetic response of SRR is due to the LC resonance, it is closely related to the geometry of the unit cell. To achieve a higher operating frequency, the total capacitance and inductance of a SRR array must be reduced. A straightforward way is to scale down the SRR unit size. Applying different designs or carefully tuning the geometric parameters may also result in desired higher operating frequencies. K. Aydin *et al.* found [17] that by engineering the structure design 1) to increase the split width, 2) to enlarge the gap distance between inner and outer rings, and 3) 50 reduce the metal line width of the rings, one would decrease the capacitance or inductance thus give rise to higher resonance frequencies, although the degree of tunability is very limit. In addition, five different resonator structures shown in Figure 2-2 together with a conventional SRR (see Figure 2-1) were studied. In both cases of single-ring and double-ring SRRs, the resonance frequency increases as the number of splits increases. This is because when a second split is placed on the ring, the capacitors are connected in series. Therefore, the total capacitance will decrease approximately by a factor of 2. Due to this great amount of reduction in capacitance of individual ring

resonators, the change in resonance frequency is very large compared to the cases when altering split widths, gap distances and metal widths. Transmission spectra of single-ring SRRs with different numbers of cut are shown in Figure 2-3. Those of double-ring SRRs are not shown here because of the similarity. Note that the experiment was done by measurements of a single resonator, so a dip in the transmission spectrum was attributed to the resonant nature of SRR. Moreover, when increasing the split width, the rate of increase is larger for structures with more splits due to larger variations in capacitance, as depicted in Figure 2-4 (again, only for the single-ring case). The measured magnetic resonance frequencies for six different resonator structures are summarized in Table 2-1. It can be seen that for mm-scaled one-cut and two-cut resonator structures, the amount of decrease in ω_m between single-ring and double-ring SRRs is around 1 GHz. But in the case of a four-cut structure, such behavior is not observed because of its symmetric orientation. The mutual capacitance between inner and outer rings is very small due to the fact that the induced charges along both rings have the same sign and similar magnitude. As a result, addition of a second ring does not affect the overall capacitance of the four-cut single-ring resonator. In turn, the resonance frequency did not change appreciably.

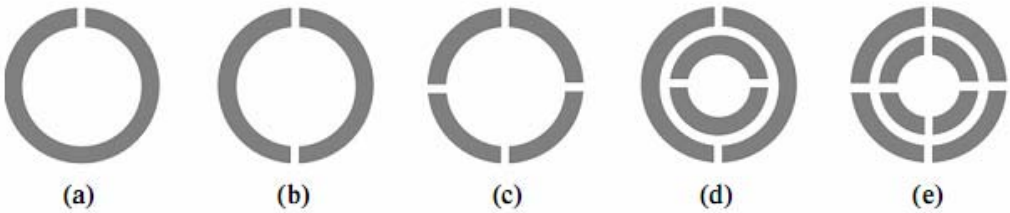

Figure 2-2 Schematic drawings of different resonator structures: (a) single-ring with one cut, (b) single-ring with two cuts, (c) single-ring with four cuts, (d) double-ring with two cuts, and (e) double-ring with four cuts. The figure is imaged from [17].

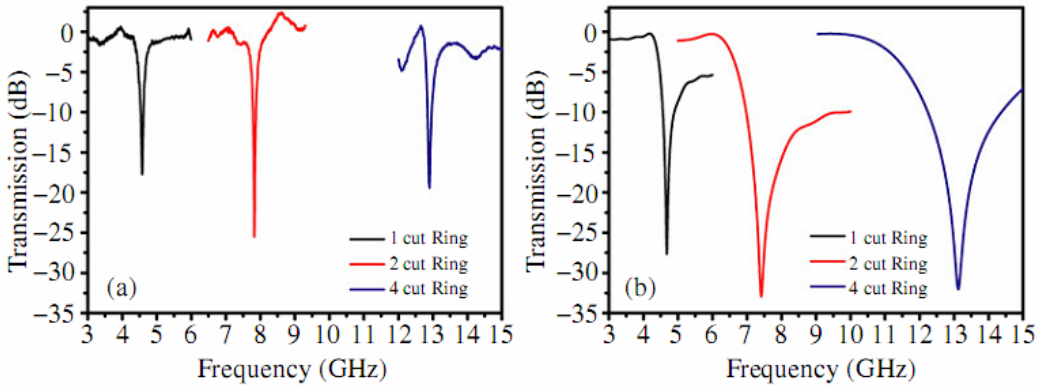

Figure 2-3 Transmission spectra of single-ring resonator with different number of cuts obtained via (a) experiments and (b) simulations. The figure is imaged from [17].

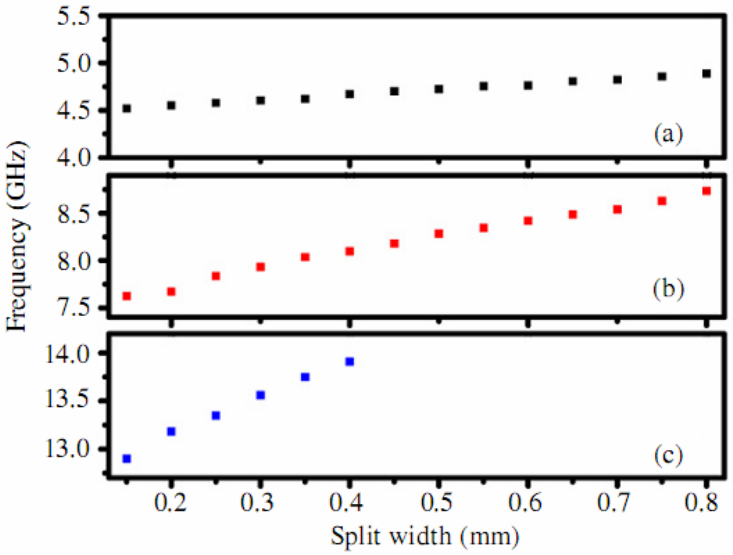

Figure 2-4 Variation of magnetic resonance frequency with the split width for (a) the one-cut, (b) two-cut, and (c) four-cut ring single-ring resonators. The figure is imaged from [17].

Table 2-1 Measured magnetic resonance frequencies (GHz) for six different resonator structures. The table is imaged from [17].

	Single-ring resonator	Double-ring resonator
One cut	4.58 GHz	3.63 GHz
Two cut	7.82 GHz	6.86 GHz
Four cut	12.9 GHz	12.96 GHz

It has been shown that mounting additional capacitance is possible for making tunable SRRs [17, 18]. On the other hand, a study regarding the length of the side arms of SRR is discussed in section 2.2.4 together with higher order excitations [27].

2.1.2 Electric Coupling Effect and Anisotropic Nature of SRR

There are four nontrivial orientation and polarization combinations of SRRs with respect to the incident EM waves that are frequently used when studying the transmission properties of SRR, as shown in Figure 2-5. It was assumed that the SRR exhibits magnetic response only for the in-plane incidence, i.e. the external magnetic field is applied perpendicular to the pattern (Figure 2-5 (a), (b)). During the study of higher dimensional LHMs, N. Katsarakis *et al.* first discovered [19] that besides a magnetic field normal to the SRR the incident electric field $\boldsymbol{E}$ couples to the magnetic resonance of the SRR when the EM waves propagate perpendicular to the SRR plane and the incident $\boldsymbol{E}$ is parallel to the gap-bearing sides of the SRR (see Figure 2-5 (d)). The effect of this electric coupling is a resonance of ε near ω_m. Figure 2-6 present the transmission spectra of the SRR in four orientation and polarization combinations. It can be seen that a stop band exists in (d), which was thought to be magnetically inactive. Note that there is a broadening of the band gap in (b), which is also a result from EEMR (electric excitation coupling to the magnetic resonance). This broader band gap was not associated with a broader LH peak when the SRRs were combined with wires [20]. The phenomenon can also be seen in the reflectance spectra in Figure 2-7, where the TE mode corresponds to (c) in Figure 2-5 and the TM mode corresponds to (d). The EEMR might degrade or even destroy the lift-handed properties of the metamaterial when the SRRs are combined with the wires, since it leads to lowering the effective plasma frequency and adds a RH transmission shoulder close to ω_m. However, it is very valuable for the experimental demonstration of the

magnetic resonance at optical frequencies, because of the difficulty in measuring the transmission and reflection with the incident EM wave parallel to the SRR plane at such frequencies

The origin of this effect is the asymmetric charge distribution (non-zero average electric polarization) in the SRR caused by the external electric field. Numerical simulations using the FDTD method were performed, which allowing visualization of the spatial distributions of the fields and currents inside the system. As shown in Figure 2-8, the SRR will experience different spatial distribution of the induced polarization, depending on the relative orientation of E with the SRR gap. If E is parallel to the no-gap sides of the SRR, its polarization will be symmetric and the polarization current is only flowing up and down the sides of the SRR, as revealed in Figure 2-8 (a). If the SRR is turned by 90° (see Figure 2-8 (b)), the broken symmetry leads to a different configuration of surface charges on both sides of the SRR, connected with a compensating current flowing between the sides. This current then also contributes to the magnetic resonance.

Marques considered the bianisotropy in SRR structures and developed an analytical model for evaluating the magnitude of cross-polarization effects [21]. It has been shown that symmetric SRRs, i.e. SRRs with two or four splits can be used to remove the electric coupling effect [22]. The problem arising from this kind of design is the difficulty of maintaining the capacitance of the single-gap ring, as the gaps act like capacitors in series, leading to a considerable lowering of the total capacitance and thus to an increase of ω_m as discussed in the last section. This might be a disadvantage as it decreases the possibility of ω_m lying below the electric cut-off frequency of the system. One solution to the problem could be decrease of the gap size, although in many cases, this method is limited by the presenting technology. Another solution could be the modification in the design, with the capacitance of the gaps being

increased. The result from such modification is usually a lowering of ω_m but not always an improvement in the transmission picture, as the strength of the magnetic resonance and the width of the $\mu<0$ regime are affected as well. Two examples of symmetric SRR designs and its possible modified forms are shown in Figure 2-9.

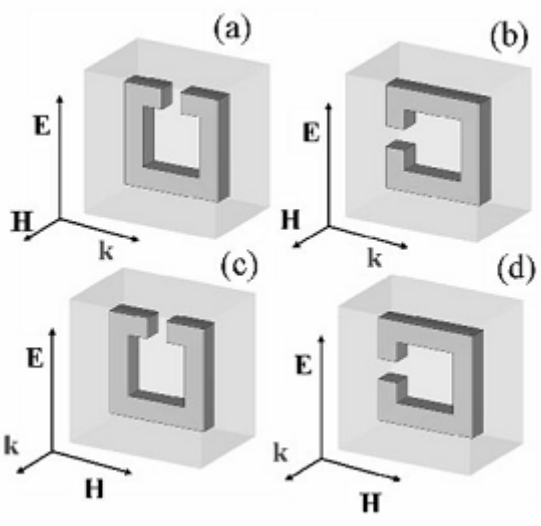

Figure 2-5 SRR in the four nontrivial EM field propagation directions and polarizations. The figure is imaged from [36].

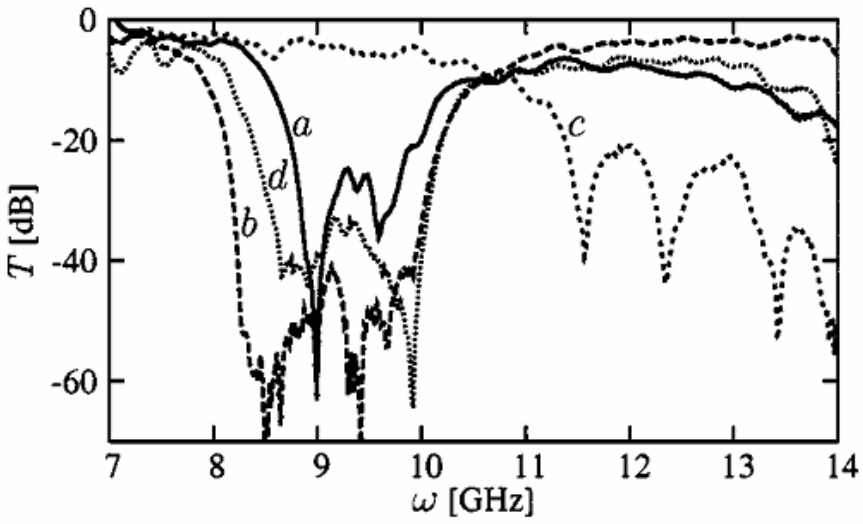

Figure 2-6 Measured transmission spectra of a lattice of SRRs for the four different orientations shown in Figure 2-5. The figure is imaged from [19].

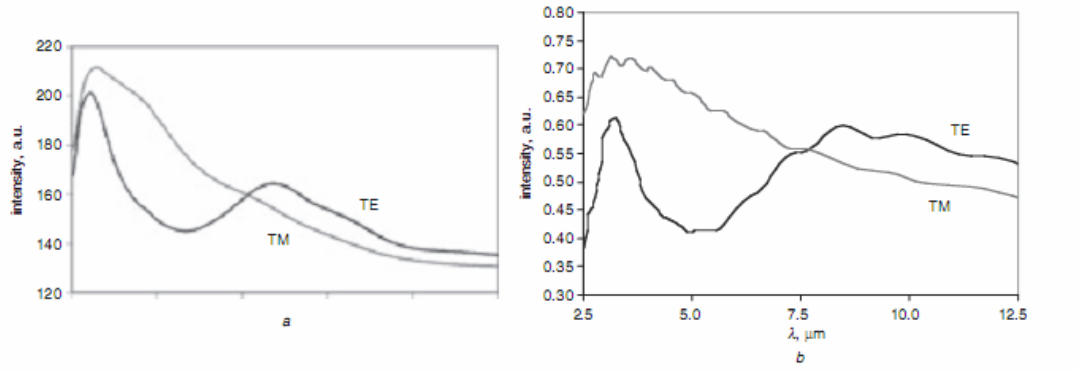

Figure 2-7 Reflectance spectra for aluminum SRR sample showing experimental and simulated TE and TM resonant peaks. The figure is imaged from [23].

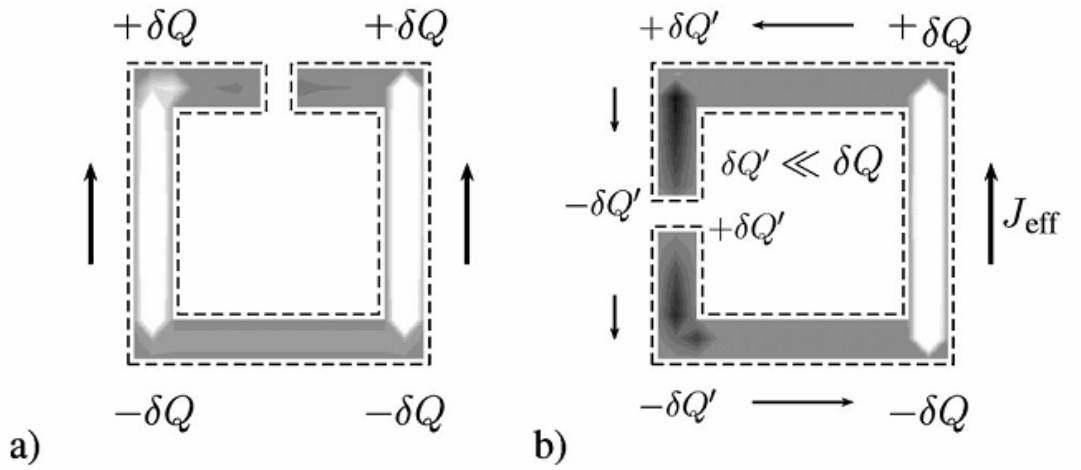

Figure 2-8 Simple drawings for the polarization in two different orientations of a single-ring SRR. The external electric field points upward. Only in case of broken symmetry (b) a circular will appear which excites the magnetic resonance of the SRR. The interior of the ring shows FDTD data for the polarization current component $J_{//E}$ at a fixed time for normal incidence as a gray scale plot. The figure is imaged from [19].

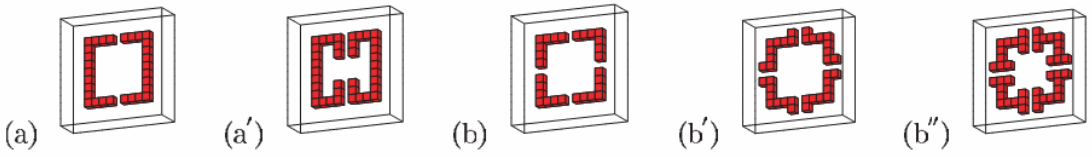

Figure 2-9 Two examples of symmetric SRR designs (a) and (b), and the possible modified forms (a') and (b'), (b'') with lowered magnetic resonance frequencies. The figure is imaged from [20].

2.2 Electric Response of SRR

SRRs have not only magnetic response, but also electric response that adds to the electric response of the wires causing the effective plasma frequency, ω'_p, of the composite medium shift to lower frequencies and differ substantially from that of the wire-only medium.

The SRR has electric response that appears at lower frequency than its magnetic response. This electric resonance is related to the plasma resonance in a thin continuous wire but shifted to nonzero frequency as a result of the additional depolarization field arising from the finite side length of the SRR. It is a collective property of the SRR array, which has a relatively low dependence on shape. At frequencies in the infrared part of the spectrum, it is also not strongly dependent on the particular metal used [23]. In fact, it is basically determined by the size of the SRR in the direction of the electric field [24]. To describe the plasma resonance of SRRs, a factor F is introduced, which is the area of exposed substrate in a unit cell, i.e. the total area of the unit cell minus the area covered by the metallic SRR. A modified equation for the reduced plasma frequency may then be written as:

$$\omega_p^2 = \frac{c^2 \cdot 2\pi}{a^2 \cdot \ln(\frac{a^2}{F}) \cdot n_{eff}^2} \text{ (rad s}^{-1}\text{)} \qquad (2.4)$$

where n_{eff} is the effective refractive index of the dielectric medium at the frequency of the infrared radiation interacting with the SRR array. As the metal area of an individual SRR increases, F decreases for a fixed unit cell area, and then the plasma frequency also decreases.

Theoretically, it might be possible to achieve a LH transmission regime using only an array of SRRs by tuning the magnetic resonance into the negative permittivity band provided by its own electric ct-wire response [20].

2.2.1 Periodic and Disordered SRR Array

In previous work, EM responses were studied for either single or an array of SRR. The sensitivities of resonance frequency to the geometrical arrangement of SRRs were reported [25]. As shown in Figure 2-10 (a), up to four SRRs were placed along the x direction (propagation direction). The decreased transmission power was measured as the number of SRRs increased, while the resonance frequency remained essentially the same. The distance between the four SRRs was then tuned. Splitting of resonance was observed experimentally for short separation distance ($d<\lambda/4$) due to the quality factor Q suddenly explodes and the main resonance frequency shifts towards lower values and become narrower. When additional rows of SRRs are added along the z direction as depicted in Figure 2-10 (b) and (c), the resonance frequencies shifted to lower values and broaden. The frequency shift decreases when more SRR rows are added. Figure 2-11 shows the relation between scattering cross section (SCS) and frequency of the incident light with two different separation distances for 1, 2, and 3 rows of SRRs in Figure 2-10 (a)-(c). It depicts the three above mentioned phenomena clearly. The scattering cross section can be obtained by integrating the scattered field over a large sphere enclosing the system (typical radius100λ). In addition, no resonance splitting occurs when the SRRs are placed side by side in y direction even for extremely small separation (Figure 2-11 (d)). The sensitivity to the geometrical arrangement imposes constraints on the accuracy with which SRR arrays must be fabricated. On the other hand, it also offers the possibility to tune the structure and place the resonance frequency at a specific value. The resonance characteristics of a SRR array depend on the number of elements, which converge with about eight elements in each direction. This is important for the implementation of SRRs in a practical device with finite size.

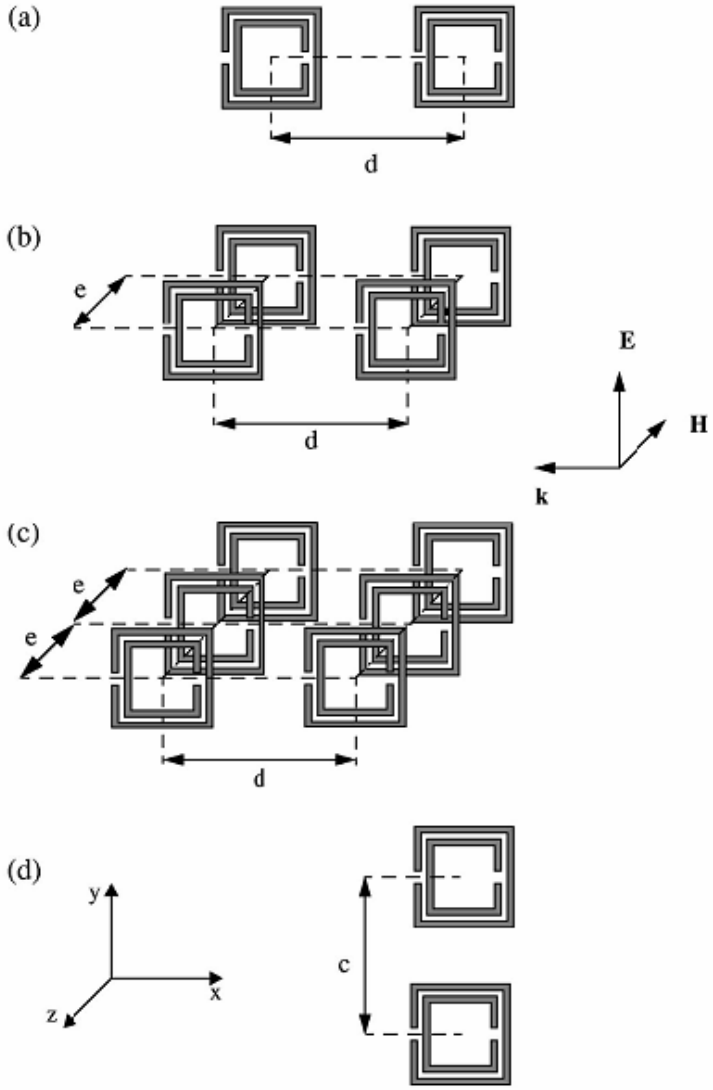

Figure 2-10 Geometries considered for the study of interacting SRRs. (a) Two SRRs in a row; (b) two SRRs rows; (c) three SRRs rows, and (d) two SRRs placed side by side. The figure is imaged from [25].

K. Aydin *et al.* investigated effects of a disordered SRR array on magnetic resonance in detail [26]. In the case of misalignments (inter-plane disorders), the SRRs within each plane are periodic in x and y directions, but the planes themselves are shifted arbitrarily in z (shown in Figure 2-12 (a) with a corresponding transmission spectrum) or x (shown in Figure 2-12 (b) and (c) with corresponding transmission spectrum, respectively) direction. By introducing randomness to the

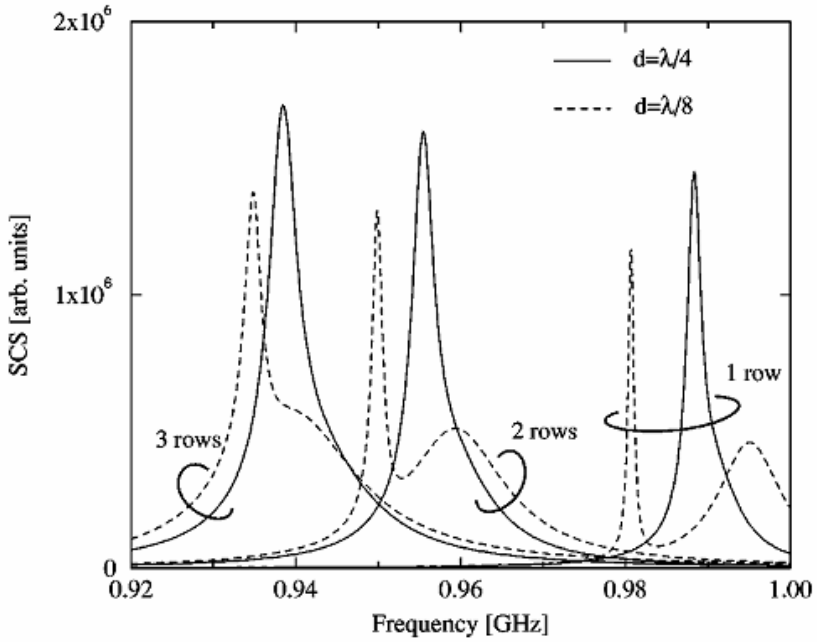

Figure 2-11 Scattering cross section (SCS) computed for 1, 2, and 3 rows of SRRs (Figure 2-10(a)-(c)). Two different separation distances *d* have been selected; the inter-row spacing is *c*=20mm. The figure is imaged from [25].

positions of SRRs along x and y directions within a plane, another type of disorder in SRR layers (intra-plane disorder) can be induced as shown in Figure 2-13 (a) and (b) with corresponding transmission spectra. By combining the inter-plane and intra-plane disorder, one can obtain a structure disordered in all three spatial directions. The transmission spectrum of such fully disordered SRR structure is shown in Figure 2-13 (d). The decreased transmission level and narrower pass band width due to reduced coupling in disordered SRR array may cause an impaired LH behavior of CMMs as presented in Figure 2-14. The dominant coupling occurs between consecutive SRRs along the propagation direction of the EM field, which depends strongly on the distance between any two adjacent SRRs along this direction. Thus, deviations from the periodic arrangement along the propagation direction have more impact on the properties of the negative permeability region.

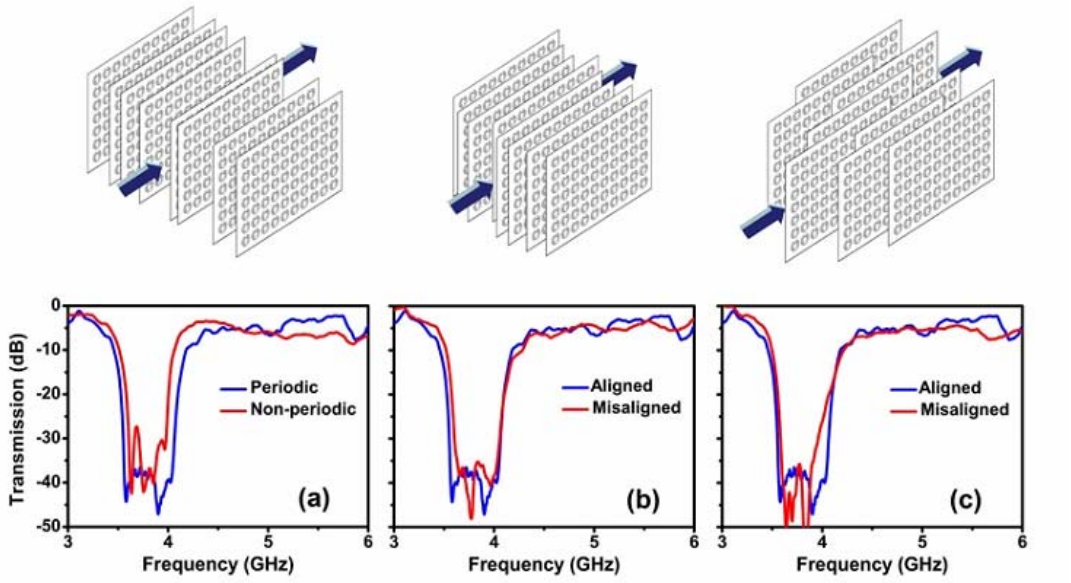

Figure 2-12 Top panel: Schematic drawings of disordered split-ring resonator media with (a) disorder in z direction with randomizing the inter-plane distance $a_z \pm \delta_z$ where $\delta_Z \le \lambda/4$, (b) disorder in x direction with misalignment parameter $|\delta_x| \le \lambda/8$, (c) increased disorder in x direction with parameter $|\delta_x| \le \lambda/2$. Bottom panel: Measured transmission spectra of periodic and ordered SRR medium (blue) and corresponding disordered split-ring resonator media (red). The figure is imaged from [26]

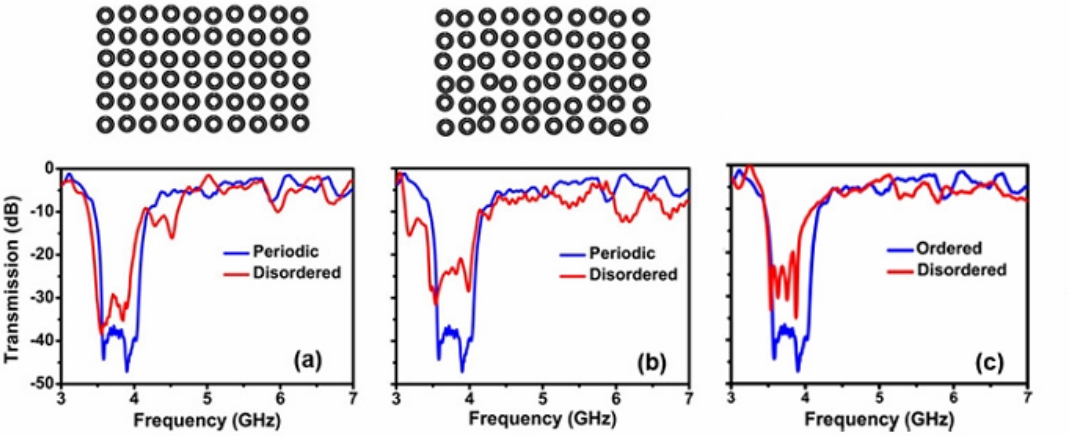

Figure 2-13 Top panel: Schematic drawings of intra-plane disordered SRRs with (a) $|\vec{\delta}_r| \le a/9$, (b) $|\vec{\delta}_r| \le a/5$ where $\vec{\delta}_r$ is the randomness parameter. Bottom panel: Measured transmission spectra of ordered SRR (blue) and disordered SRR media (red), (c) Comparison of the transmission spectra for ordered and disordered SRRs where the disorder is in all 3 spatial directions. The figure is imaged from [26]

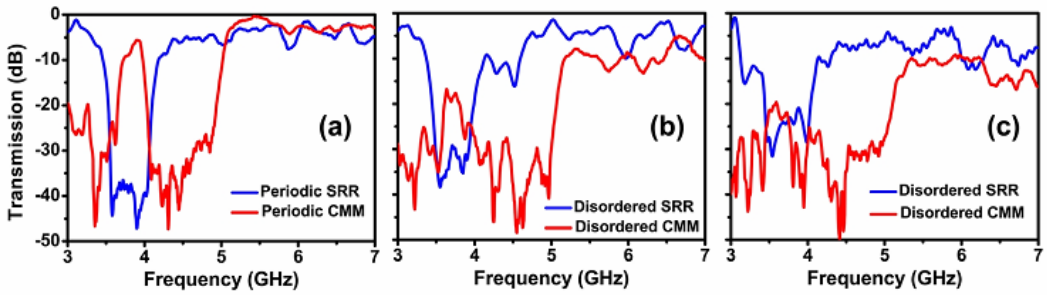

Figure 2-14 Measured transmission spectra of periodic and ordered SRR medium (blue) and corresponding disordered split-ring resonator mediums (red). The figure is imaged from [26]

2.3 Identifying Magnetic Response of SRR

Since SRRs exhibit electric response in addition to magnetic response, identifying magnetic response from transmission spectra of SRR is thus very crucial and valuable in experimental studies. In practice, ε and μ. are difficult to be obtained simultaneously. Some transmission peaks were thought to be LH, but in fact originated with RH.

K. Aydin *et al.* provided four useful experimental methods, in order to identify the magnetic resonance of SRRs at the microwave frequency regime [13]. In their study, transmissions of two orientations of SRR with respect to the incident EM wave were measured. The schematic drawings of the two types of SRR (named SRR (A) and SRR (B) here) are depicted in Figure 2-15, corresponding to Figure 2-5 (a) and (b) respectively. Then the closed ring resonators (CRR) (Figure 2-16) were used to kill the magnetic resonance while retain the electric resonance. The transmission spectra of SRR (A), SRR (B), and CRR are presented in Figure 2-17 at two frequency ranges where the magnetic and electric response were expected to take place. Figure 2-17 (a) shows that the transmission dip caused by magnetic response disappeared in CRR while Figure 2-17 (b) demonstrates that its electric response retained. Note that the electrical resonance frequency for SRR (B) structure is observed at a lower frequency

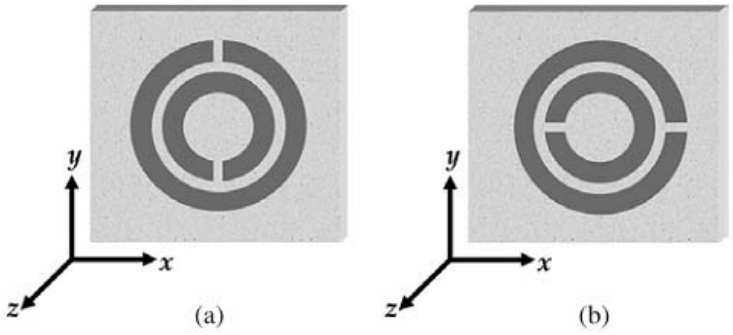

Figure 2-15 Unit cell of split-ring resonators with split-axis along the (A) y direction, (B) x direction. (*k* is along x direction, ***E*** is along y direction and ***H*** is along z direction.) The figure is imaged from [13]

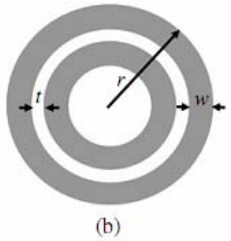

Figure 2-16 Schematic drawing of unit cell of CRR. The figure is imaged from [17].

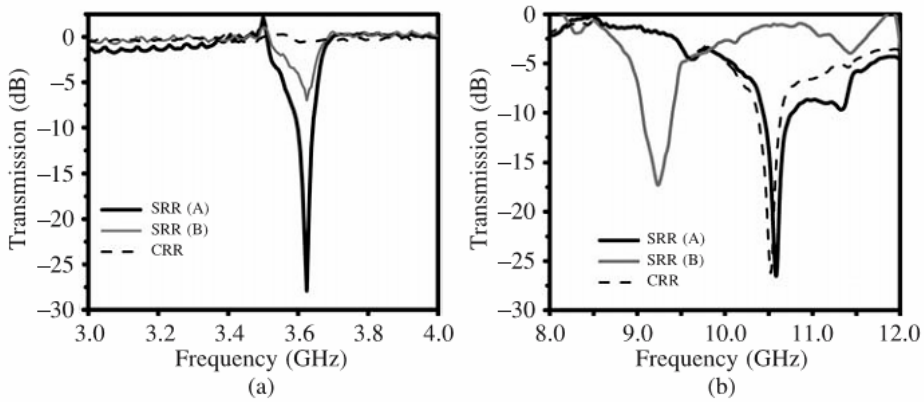

Figure 2-17 Measured transmission spectra of the unit cell of SRR (A), SRR (B), and CRR structures at (a) 3-4 GHz and (b) 8-12 GHz. The figure is imaged from [13]

while electric resonance at same frequency for all structures is expected. This behavior is attributed to the orientation of the splits with respect to the electric field. Many other experimental studies [17, 22] also reported that closing the gap of the SRR can eliminate the capacitor of the SRR, and thus is an efficient way to destroy

the magnetic resonance. One can then identify the magnetic response of SRR by comparing the transmission spectrum to that of CRR.

2.4 Higher Order Excitation Modes of SRR

J. Zhou *et al.* studied numerical simulations of the higher order excitation modes of SRRs, and how the length of the side arms of SRR affects its EM response [27]. The geometrical parameters of a U-shaped SRR unit cell are indicated in Figure 2-18. First, as shown in Figure 2-19, the real part of effective ε and μ were extracted for three orientation and polarization combinations of SRR with respect to the incident EM waves, which represented pure magnetic resonance, EEMR (electric excitation coupling to the magnetic resonance), and short-wire like or electric resonance according (correspond to Figure 2-5 (a), (d) and (c), respectively). It can be seen that the EEMR had a resonance in ε at roughly the same frequency ω_m=55 THz as the magnetic resonance in μ. At a higher frequency, ω_0=135 THz, the short-wire-like electric resonance in ε occurred. Notice that when the lattice constant was comparable to the resonance wavelength (the EEMR in this case), a stronger distortion in negative part of resonance and a more significant anti-resonance could be observed due to the periodicity effect [12].

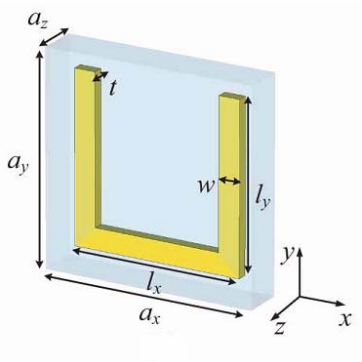

Figure 2-18 A U-shaped SRR unit cell with geometrical parameters. The figure is imaged from [27].

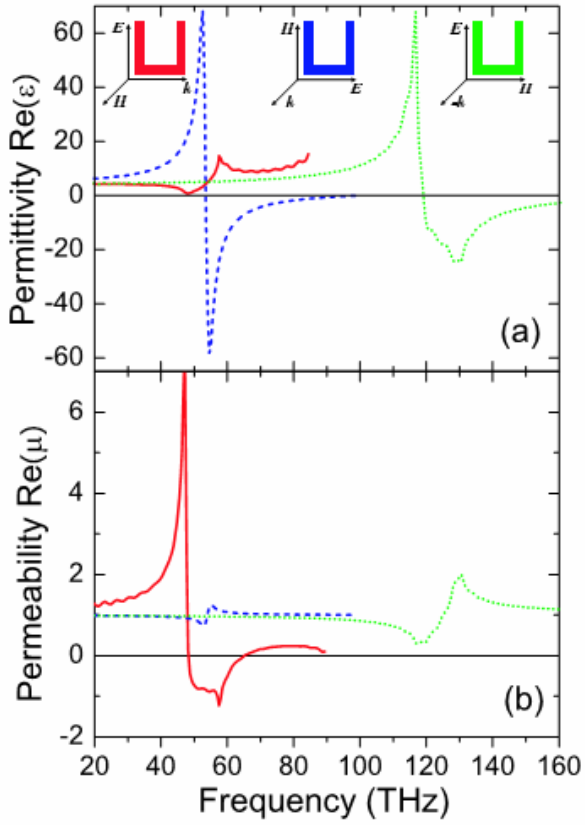

Figure 2-19 Extracted real part of (a) effective permittivity Re($\varepsilon(\omega)$) and (b) effective permeability Re($\mu(\omega)$) for the magnetic resonance (red solid), the electric excitation coupling to the magnetic resonance (EEMR) (blue dashed) and the short-wire-like resonance (green dotted) of U-shaped gold SRRs. The geometric parameters are $a_x = a_y = 1$ μm, $a_z = 0.2$ μm, $l_x = l_y = 0.8$ μm, $w = 0.1$ μm and $t = 0.05$ μm. The U-shaped SRR is described by the Drude model with plasma frequency fp = 2175 THz, and damping frequency $f\tau$ = 6.5THz. The figure is imaged from [27].

Secondly, higher excitation modes were presented for the EEMR and short-wire like resonance through both transmission spectra and extracted Re(ε), as shown in Figure 2-20. As a very crude picture we could imagine the resonance of the SRRs as charge density waves on a rod with the length equal to the arc length of the SRR. This rod supports plasmonic modes, which occur at discrete frequencies whenever there are current nodes at the ends of the rod. Considering that the current distribution is an essential tool for understanding the resonant modes of a SRR at higher THz frequencies while in the microwave region only the remnants of the resonant modes

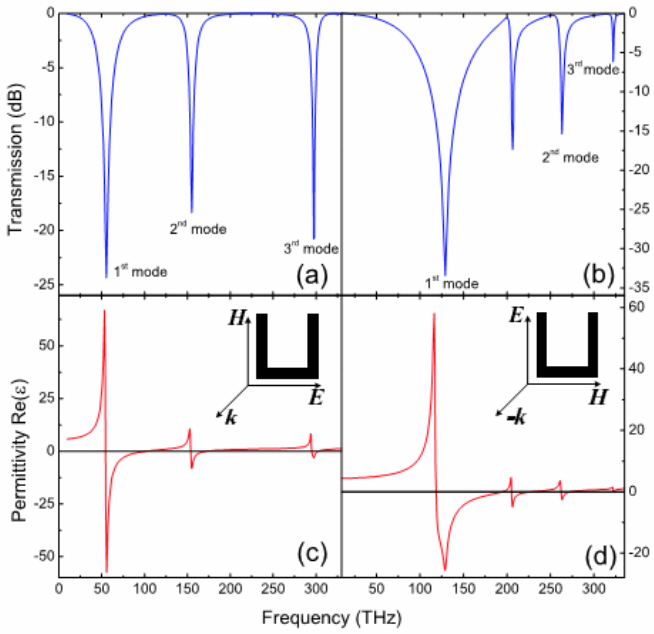

Figure 2-20 (a), (b): Transmission spectra and (c), (d): the extracted Re(ε) of the U-shaped SRRs response to the incident EM wave. The figure is imaged from [27].

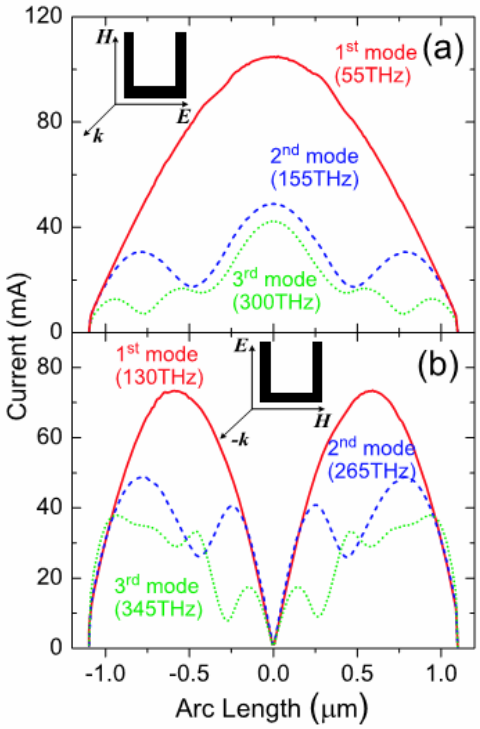

Figure 2-21 Current distribution of the lowest 3 modes. (a) λ /2, 3λ /2, and 5λ /2 mode for the EEMR response; and (b) λ , 2λ , and 3λ mode for the short-wire-like response. Due to the nonzero response of lower order modes, nodes of higher order modes only reach zero at the positions of the lowest nodes. The figure is imaged from [27].

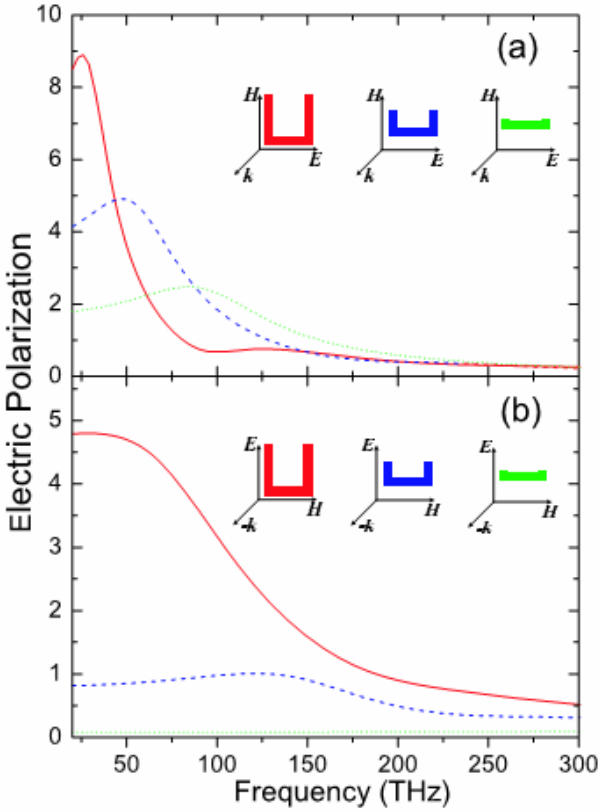

Figure 2-22 Magnitude of the normalized polarization density, P, of the U-shaped SRRs with l_y = 0.8 μm (red solid), 0.4 μm (blue dashed) and 0.11 μm (green dotted), respectively. (a) P_x component as $\boldsymbol{E}$ parallel to the bottom part of SRRs. While the other two components P_y and P_z are nearly zero (not shown in the figure). (b) P_y component as $\boldsymbol{E}$ parallel to the side part of SRRs, while the other two components P_x and P_z are again nearly zero (not shown in the figure). The figure is imaged from [27].

of the lowest order mode survive. However, it is of limited value due to a strong dependence of EM responses and plasmonic dispersion on the geometry which might be very different for SRRs from a rod. Simulations of the current distribution in Figure 2-21 revealed that the magnetic resonances are modes with odd number of half wavelength of the current density wave, i.e. λ/2, 3λ/2, and 5λ/2, while the electric resonances are modes with integer number of whole wavelength the current density wave, i.e. 1λ, 2λ, and 3λ. Note the non-uniform spacing of the nodes or higher orders are different from the straight rod and are due to the curvature of the SRR and the coupling to the bottom arm or side arms only.

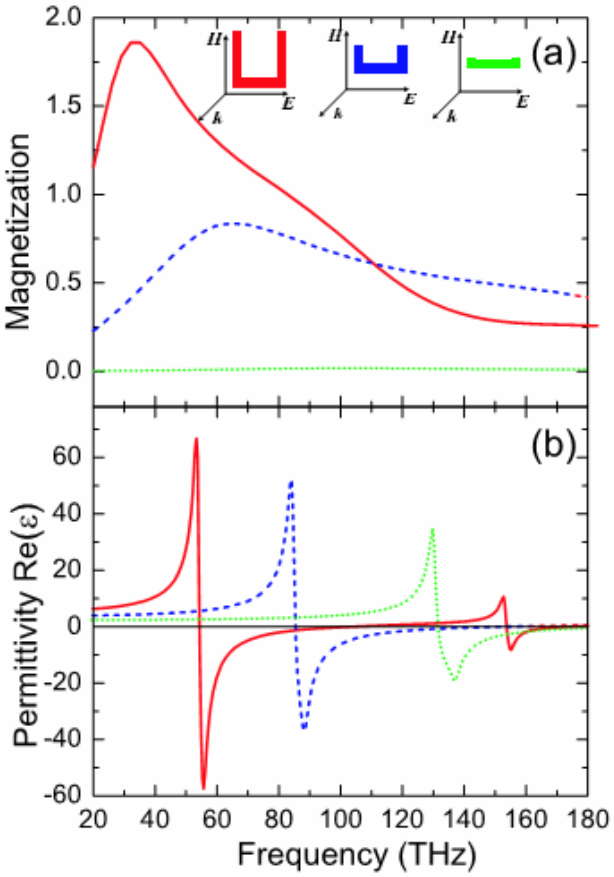

Figure 2-23 (a) Magnitude of the normalized magnetization, M_z, and (b) the extracted real part of permittivity, Re(ε), of the U-shaped SRRs with the length l_y = 0.8 μm (red solid), 0.4 μm (blue dashed) and 0.11 μm (green dotted), respectively. The short-wire-like resonance has zero magnetic moment (not shown in the figure). The figure is imaged from [27].

Finally, the electric polarizations of the EEMR (Figure 2-22 (a)), short-wire-like resonance (Figure 2-22 (b)), as well as the magnetism of the EEMR (Figure 2-23 (a)) of the U-shaped SRRs were calculated for the different length of side arms l_y. In all three cases, the polarization decreased and shifted to higher frequencies as l_y decreased. The EEMR response became weaker and eventually disappeared as l_y reduced to zero. However, P_x did not vanish when l_y=0 because the EEMR degenerated to the short-wire-like resonance of the bottom arm of the SRR which resulted in non-zero electric polarization. In contrast, the magnetic moment of the magnetic resonance vanishes as the length of side arms of the SRR reduces to zero, i.e.

a rod does not give any magnetic moment or magnetic resonance. Figure 2-23 (b) shows that the magnitude of the resonance in Re(ε) decreases much slower than the magnetic moment dose as the arm length decreases. The reason is that the magnetic moment vanishes immediately as the side arms disappear, but the resonance in Re(ε) always exists as long as the short-wire-like electric resonance exists in the bottom part of the SRR.

2.5 Properties of CMM

M. Kafesaki *et al.* gave parametric studies of LHMs that aimed at optimum parameters for obtaining a true broad LH transmission band with large transmitted power [20]. The optimum position of the wires found in the study is at the back of the dielectric boards, just behind the cuts of the rings, while the distance of the wire to the SRR plane does not influence the LH peak very much. In fact, there are typically two arrangements of SRRs and wires when making CMMs. One is by stacking layers of SRRs and wires alternatively (off-plane), and another is by placing SRRs and wires side by side (in-plane). It is found that for in-plane CMMs, the left-handed transmission peak is much narrower and ω'_p is higher than that for off-plane ones. The reduction in ω'_p suggests that there is a significant coupling between the electric response of the wires and that of the SRRs in the off-plane case [24]. This makes the off-plane CMMs more preferable for obtaining LHMs. Nevertheless, the fabrication process could be complex, and an alignment problem might occur. In-plane and off-plane configurations of CMMs and comparison of their transmission spectra are shown in Figure 2-24.

The effective medium theory proposed by T. Koschny *et al.* gave analytical equations for the effective ε of wires and SRRs as well as for the effective μ of SRRs

are given [24]:

$$\varepsilon_{eff}^{wire}(\omega) = 1 - \frac{\omega_p^2}{\omega^2 + i\omega\gamma} \tag{2.5}$$

$$\mu_{eff}^{SRR}(\omega) = 1 - \frac{\omega'^2_m \quad \omega_m^2}{\omega^2 - \omega_m^2 + i\omega\gamma} \tag{2.6}$$

$$\varepsilon_{eff}^{SRR}(\omega) = 1 - \frac{\omega_p^2 \quad \omega_0^2}{\omega^2 - \omega_0^2 + i\omega\gamma} \tag{2.7}$$

The response of various components of a metamaterial of SRRs and wires to an EM field was presented in a compact schematic form as shown in Figure 2-25. This response is shown through the frequency dependence of the transmission coefficient (left panels), dielectric function (middle panels), and magnetic permeability (right panels). The first row shows the response of a periodic system of infinite wires. This response is analogous to that of a bulk metal, i.e. there is a cut-off frequency ω_p above which $\varepsilon(\omega)$ becomes positive from negative, and thus the system becomes "transparent" to the EM radiation. The system does not have any magnetic response. The second row shows the response of a system of cut-wires (with the wire length much shorter than the EM wavelength), or CRRs. Different from the continuous wires, here the negative ε regime has also a lower edge $\omega_0 \neq 0$, due to the finite nature of the wires. The $\varepsilon(\omega)$ has the form shown in the middle graph. Again there is no magnetic response. The third row shows the response of a periodic system of (single-ring) SRRs. Their electric response is cut-wire-like (as in the second row) and their magnetic response has a resonance frequency at ω_m where μ jumps from positive to negative values. The transmission (left panel) becomes finite in the regions of positive product $\varepsilon\mu$, and goes to zero for negative $\varepsilon\mu$. The relative order of the characteristic frequencies (ω_m, ω_p, ω_0) depends on the parameters of each specific system. The forth row shows the response of a system of infinite wires plus cut-wires

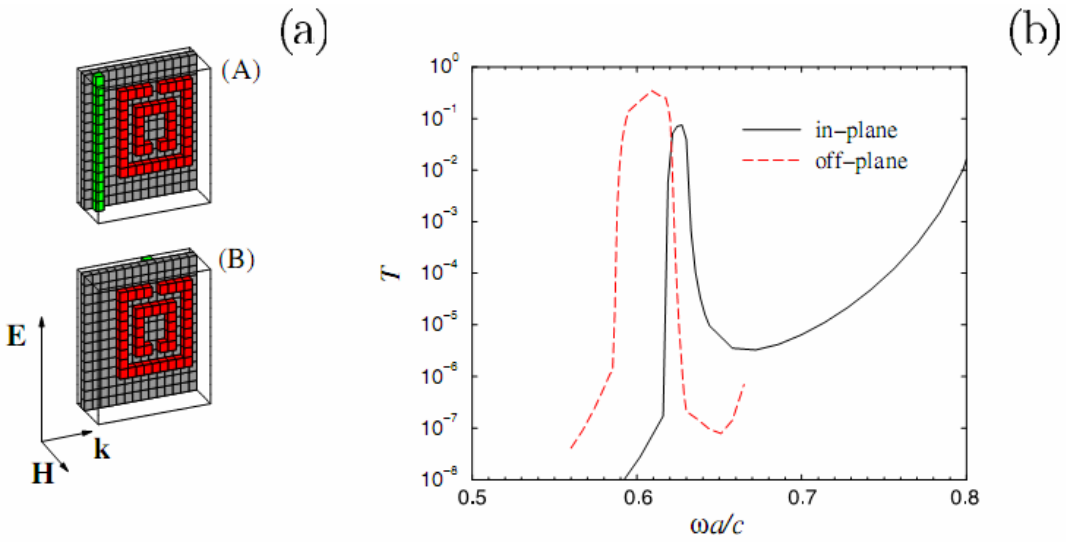

Figure 2-24 (A) In-plane and (B) off-plane configurations of CMMs. (b): Transmission coefficient (T in dB) versus the dimensionless frequency for the structures shown in (a). The solid curve showed T for the configuration (A), i.e. wires next to the SRRs, and the dashed curve was for the configuration (B), i.e. wires at the back of the board. The board was a thin dielectric layer (thickness=a/14) of dielectric constant ε_b=12.3. The rest of the background material was air. The unit cell was a cube, with the lattice constant a; the SRR had an outer side length of 9a/14 and other characteristic lengths were a/14. The wire has a cross-section at the ***H***–k plane of $(a/14) \times (a/14)$. The figure is imaged from [20].

(CRR). This system contains, in fact, all the electric response of the LHM, without its magnetic response. The combined electric response of combined wires and cut-wires has a new cut-off frequency, ω'_p, which is much lower than ω_p. The last row shows the full response of the LHM. Its electric response is that of a system of wires plus cut-wires (the forth row), and its magnetic response is that of a periodic system of SRRs (the third row).

The most important issue aroused from combining SRRs and wires is the lowing of the effective cut-off frequency ω'_p due to interaction between electric responses of SRRs and wires. In some cases it is possible that ω'_p is lower than ω_m, and transmission peaks appear at low frequencies would be RH rather than LH. A simple way to study the combined electric response of the LHMs is to close the gaps in the

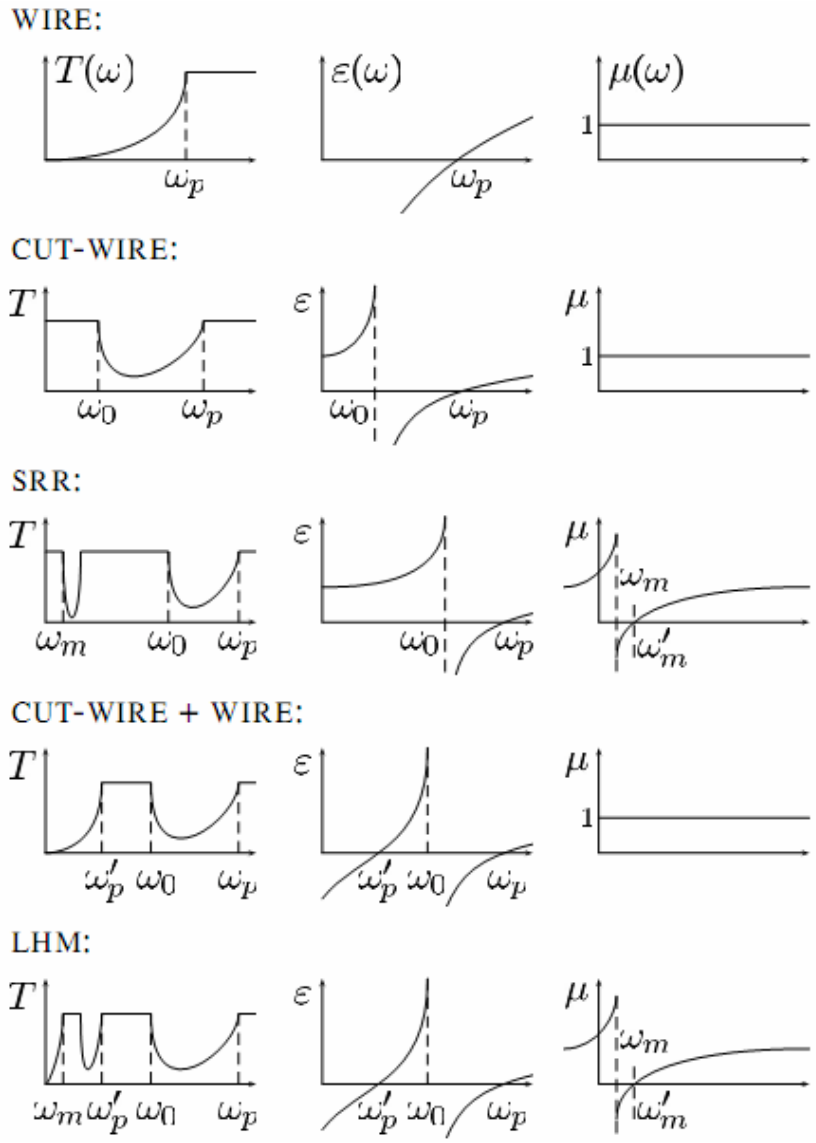

Figure 2-25 Each row shows the response of one of five periodic systems to electromagnetic wave. This response is shown through the frequency dependence of transmission coefficient (left panels), dielectric function (middle panels), and magnetic permeability (right panels). The figure is imaged from [24].

rings of the SRRs and kill the magnetic resonance without substantially affecting their electric response. This also gives an easy criterion to identify whether an experimental transmission peak is LH or RH: If closing the gaps of the SRRs in a given LHM structure removes the peak close to the position of the SRR dip from the ***T*** spectrum, this implies that the ***T*** peak is indeed left-handed.

It is shown that ω_p increases as the width of the metallic wires increase [20].

Calculations of the transmission coefficient through the combined system of closed SRRs and wires showed that ω'_p also increases, although it depends on the relative position and distance of ω_p and ω_0 as well. The thickness of the wires has an effect similar to that of the width on ω'_p. On the other hand, both the width and thickness of the SRR rings have almost no effect on ω'_p. This is of great importance as the thickness and width of the SRRs have considerable effects on ω_m. Thus, since ω_m is controlled only by the SRRs while ω'_p is controlled also by the wires, one may has the ability to control the electric and magnetic response of the LHMs "independently".

2.6 Other Structures Generating Negative μ or n

To date, besides the early invented SRR, many different structures have been reported by several groups of researchers for achieving $\mu<0$ such as the S-shaped [10], H-shaped [53], paired-rod [9] or double-wire [54], and π-shaped [55] structure. Among these works, the S-shaped SRR is able to yield negative ε and μ at the same frequency range and thus is worth mentioning here.

SRRs exhibit a frequency band of negative ε that is higher than that of negative μ, and they do not overlap in general. A previously purposed structure of two SRRs printed on the opposite sides of the substrate has been proven to avoid bianisotropy, and has the same magnetic effect as the conventional SRR structures. The geometry of this structure is shown in Figure 2-26 (a) and its Re(ε) and Re(μ) are plotted in Figure (b) and (c). One can clearly see that negative μ happens at a lower frequency range than that of negative ε, thus there is no overlap. The structure was constructed where the branches of a single SRR are shaped like a squared S and two SRRs were printed on each side of the substrate, yielding an eight-like pattern when viewed from

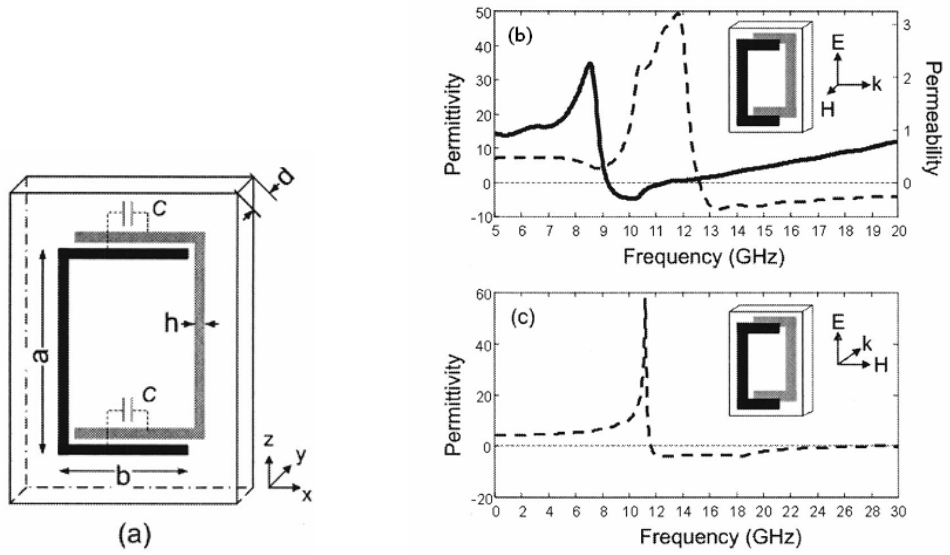

Figure 2-26 (a) is the simplified ring geometry as first building block toward S structure. Metalization is applied on each side of the substrate, and the capacitances C enables current to flow around the ring under magnetic induction. (b) and (c) are the real parts of permittivity (dashed line, left axis) and permeability (solid line, right axis). Responses are the function of frequency for SRR structures and incidence, as shown in the insets. The figure is imaged from [28].

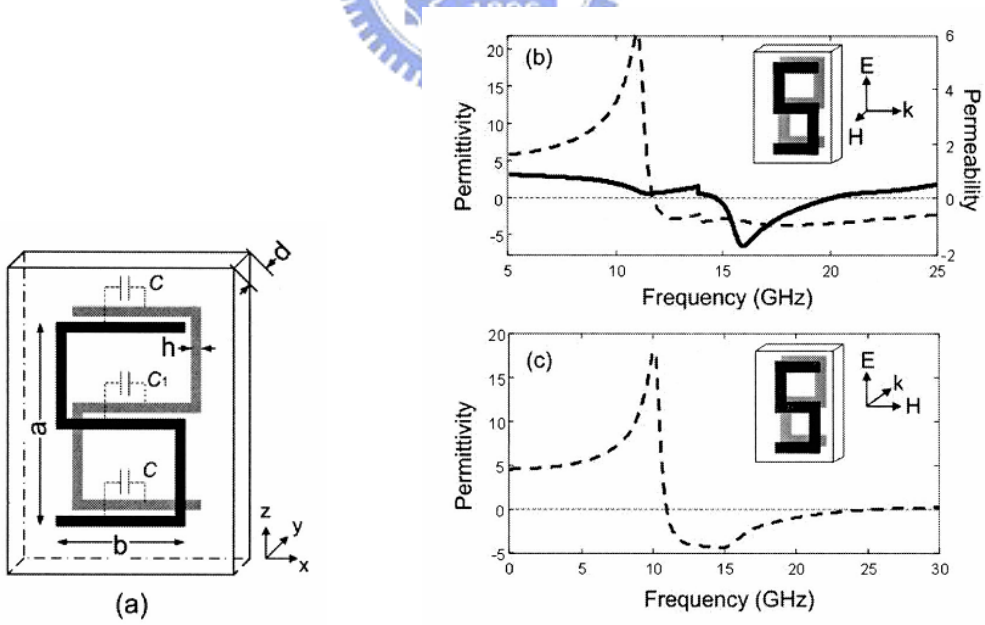

Figure 2-27 (a) is a schematic drawing of the S-shaped resonator. Note the additional capacitance *C*1 when compared to Figure 2-28 (a). (b) and (c) are the real parts of permittivity (dashed line, left axis) and permeability (solid line, right axis). Responses are the function of frequency for S-shaped resonator structures and incidence, as shown in the insets. The figure is imaged from [28].

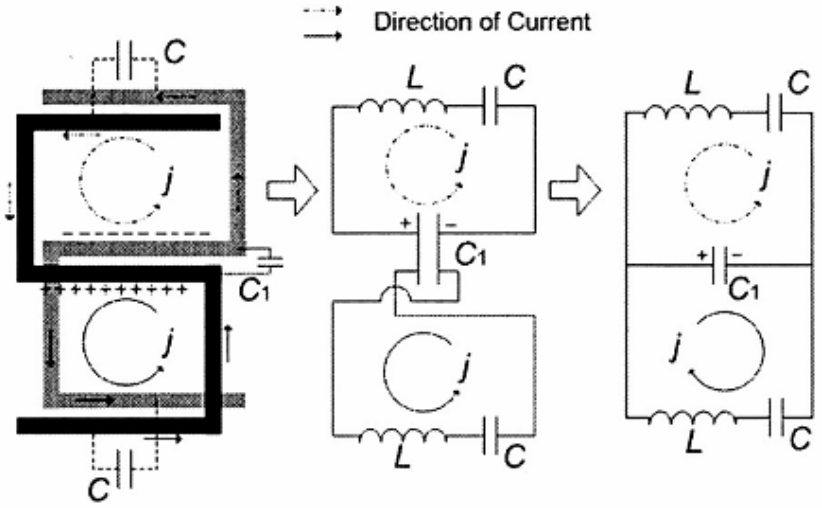

Figure 2-28 Equivalent circuit for the geometry shown in Figure 2-29 (a). Capacitance *C*1 enables current to flow in each half ring when a magnetic field is applied. The figure is imaged from [28].

top (see Figure 2-27 (a)). Again, Re(ε) and Re(μ) are plotted. As can be seen from Figure 2-27 (b) and (c), the S-shaped resonator lowered the electric resonant frequency from 12 GHz to 11 GHz and increased the magnetic resonant frequency from 9 GHz to 15 GHz, and therefore made the two frequency bands overlap from 10.9 GHz to 13.5 GHz (i.e., about 2.6 GHz bandwidth). The losses (-1.75 dB/cm) are also proven to be significantly less than that of the standard split ring and rod designs (-6.53 dB/cm). An equivalent circuit is presented in Figure 2-28. Besides the two capacitances C between the top and bottom metallic strips, there is another capacitance C1 between the center metallic strips. With C1 being large and equal to C, the S-shaped resonator has a magnetic resonant frequency $\sqrt{3}$ times that of the SRR in Figure 2-26 (a), while exhibiting the same electric property. Yet the extra lengths of wire introduce an extra inductance, and the effect is to decrease the overall plasma frequency.

Chapter 3

Design of Nano-scaled SRR

LHMs were first realized at frequencies around 10 GHz (3 cm wavelength) and fabricated mostly on stacked printed circuit boards. These samples allowed a broad tunability of patterns and arrangements thus enabled investigation in several different properties. Then, microstructures with magnetic resonance frequencies at about 1 THz (300μm wavelength) were fabricated by microlithography. Using nanofabrication techniques, the LC resonance frequency could increase to about 100 THz (3 μm wavelength) [4], bringing optical frequencies into research for obtaining negative index of refraction.

Mean-field theoretical consideration indicates that the characteristic scale of SRRs should be at least tens or few hundred times smaller than the incident wavelength. In fact, previous studies have shown that by employing the SRR with a size $1/11^{th}$ of the incident wavelength, magnetic resonance can be obtained [13]. Thus, SRRs are designed with a typical size that is about one tenth the wavelength of the desired operating frequency [23]. In the microwave region, the mm-scaled SRR cell is easily fabricated, but fabrication in the optical wavelength region is difficult since the SRR pattern must be shrunk to the nanometer scale.

This thesis work mainly focused on two aspects: (1) demonstrating the electric and magnetic responses of nano-scaled SRRs, which were previously done mostly for mm- or μm-scaled SRRs; (2) observing the scaling of the electric and magnetic

resonance frequency for nano-scaled SRRs. In the following sections, the design concepts of the nano-scaled SRR are presented in details.

3.1 Non-linear Scaling of SRR

Typically, SRR has a unit cell size that is $1/10^{th}$ [23] to $1/11^{th}$ [13] of the incident wavelength. However, as the operating frequency becomes higher and higher, non-linear scaling has been reported. Many approaches have been applied to study the physical reason and mechanism of this effect.

Ishikawa and T. Tanaka reported the effects of the surface resistivity and the internal reactance on the magnetic responses of the SRR by considering the delay of the current in the conductor [33]. The frequency dependence of the surface resistivity and internal reactance is depicted in Figure 3-1. As the frequency increases, both surface resistivity and internal reactance of the metals increase. The increase of the surface resistivity results in the decrease of the Q value of the SRR, and thereby, degrades the tunable range of the permeability μ. The increase of the internal reactance leads to the reduction of the SRR resonant frequency. The surface resistivity saturates at the inherent frequency of each metal about 10 THz. The saturation value of silver is remarkably smaller than those of gold and copper. The internal reactance, on the other hand, does not saturate and moves away from zero drastically as the frequency increases. As a result, in the optical frequency region, the effect of the internal reactance on the resonant frequency of the SRR was found to be more dominant than that of the surface resistivity. It can be seen in Figure 3-2 that as the geometric size of the SRR decreases, the magnetic response that is defined by the difference between maximum and minimum values of the effective μ decreases. And the resonant frequency shifts to a higher value. Note that the increase of the resonant

frequency is not linearly proportional to the sizes of the SRR due to the increase of the internal reactance.

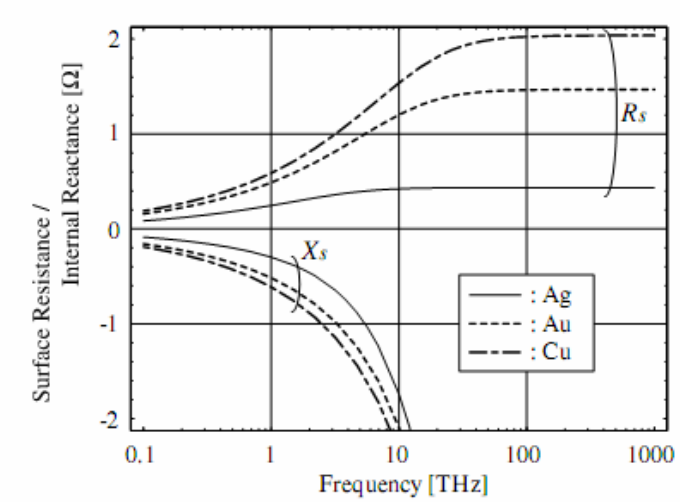

Figure 3-1 Dispersion curves of the internal impedance of silver, gold, and copper. In the frequency region exceeding THz, the internal reactance is more dominant than the surface resistivity, and this internal reactance decreases the resonant frequency. The figure is imaged from [33].

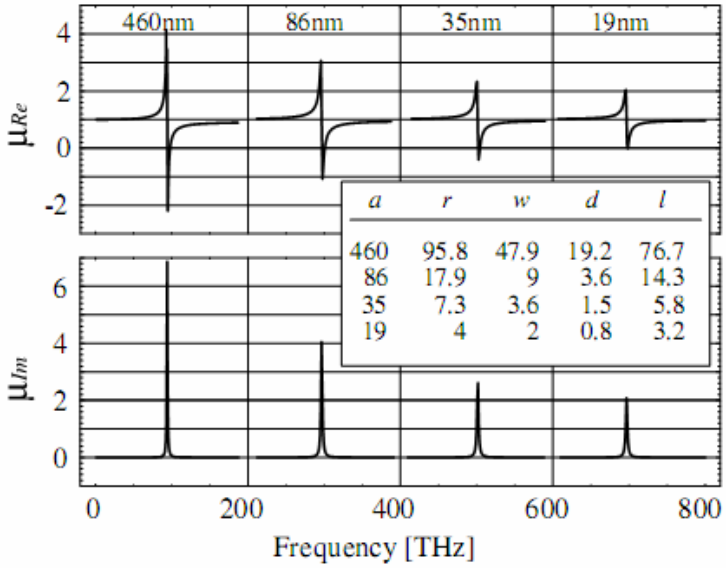

Figure 3-2 Real and imaginary parts of the effective permeability of the silver SRRs as a function of the SRR pattern size. The labeling in each case indicates the unit-cell size a. The inset shows the corresponding sizes of the SRR in nanometers. The figure is imaged from [33].

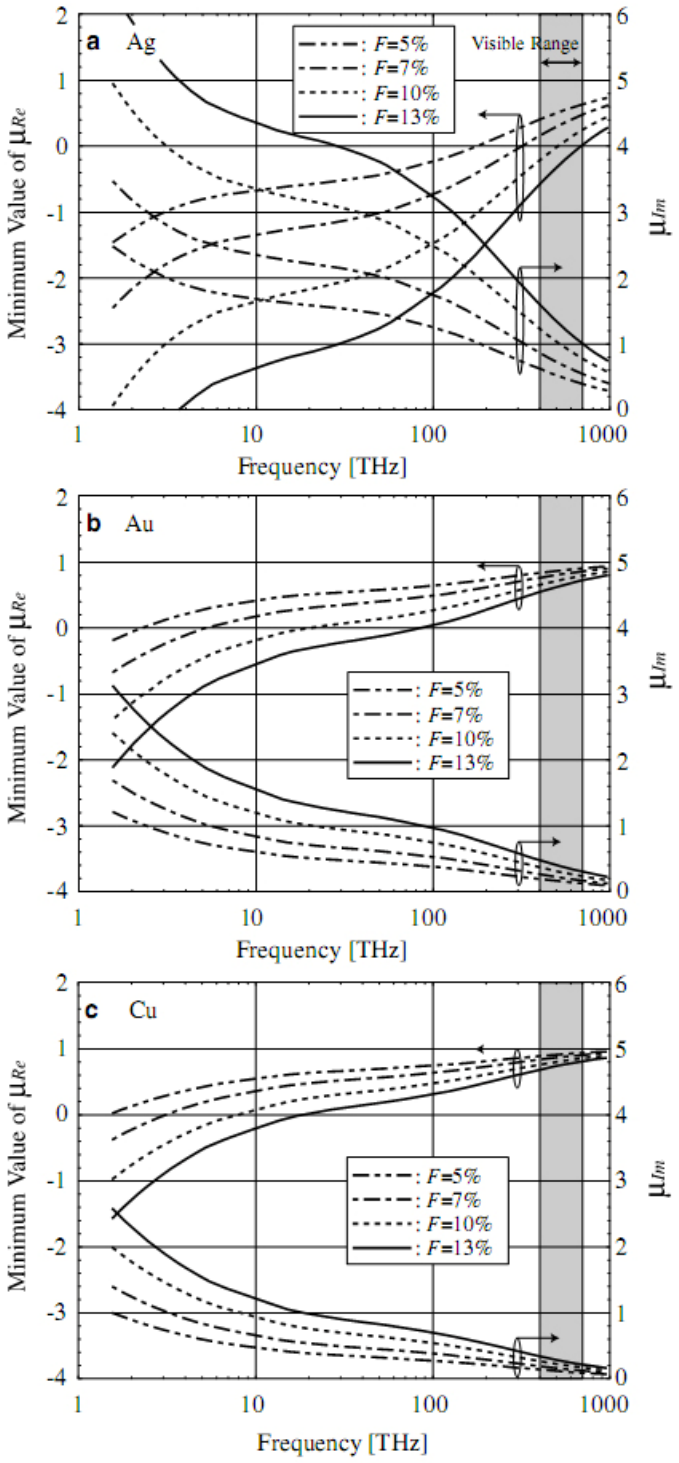

Figure 3-3 Frequency dependencies of the minimum value of Re(μ) of the SRRs made of (a) silver, (b) gold, and (c) copper, with the filling factor of F = 5%, 7%, 10%, and 13%, respectively. The frequency dependencies of the imaginary part of the effective permeability lRe whose real part has the minimum value are also shown. Only the silver SRR exhibits negative l in the visible range of 400–700 THz. The figure is imaged from [33].

The frequency dependence of the minimum value of Re(μ) of the SRR for three kinds of metals and four different filling factors were plotted in Figure 3-3. As the frequency increases, the minimum value of Re(μ) approaches unity asymptotically. Only the silver SRR exhibits negative Re(μ) in the visible light range, while the propagation loss of silver is higher than that of gold or copper. Note that the filling factor is also important for the realization of the negative μ in visible light range.

Further studies showed that above the linear scaling regime the resonance frequency saturates due to the free electron kinetic energy, which cannot be neglected any longer in comparison with the magnetic energy [34]. Although the presence of the magnetic resonance was reported to be observed with very small unit cells, such a weak resonance was unable to conduct negative values as Re(μ) approaches unity. The maximum resonance frequency (and thus the negative Re(μ) region) increases with the number of cuts in the SRR. The 4-cut SRR retains the negative Re(μ) region for higher frequencies up to about 550 THz. As a comparison, the 2- and 1-cut SRR could only reach up to 420 THz and 280 THz (unit cell size ~60 nm), respectively. The geometries of the 1-, 2-, and 4-cut single-ring SRR are schematically presented in Figure 3-4 (a). Note that the gap widths were designed to make the capacitance of the three types of SRR approximately the same, but the experimental result revealed that the three capacitances were indeed different. This is because the formula $C \sim \frac{wt}{d}$ is not valid when d is not much smaller than w. Moreover, the periodic boundary condition along the direction of the electric field only adds asymmetric side capacitances to the SRR, as which is represented by the equivalent circuit in Figure 3-4 (b). Therefore, the three types of SRR have inequivalent capacitances and thus different saturation frequencies. The scaling of the magnetic resonance frequency as a function of the unit cell size a is shown in Figure 3-5.

The electron kinetic energy adds an electron self-inductance L_e to the magnetic response which scales as $1/a$ while both the magnetic field inductance L_m and capacitance C of the SRR scale as a. The resonance frequency f_m thus has the following a-dependence:

$$f_m = \frac{1}{2\pi}\frac{1}{\sqrt{(L_m + L_e)C}} = \frac{1}{2\pi}\frac{1}{\sqrt{c_1 a^2 + c_2}} \tag{3.1}$$

where c_1 and c_2 are independent of a. Other factors that break the linear scaling and contribute to the increase of the Ohmic losses are (1) the increased scattering of electrons at the surface of the metal and (2) the larger skin depth (scales as $\frac{1}{\sqrt{a}}$) over metal thickness ratio. Both factors depend in a complicated way on the geometry and the surface smoothness, and thus require further experimental studies.

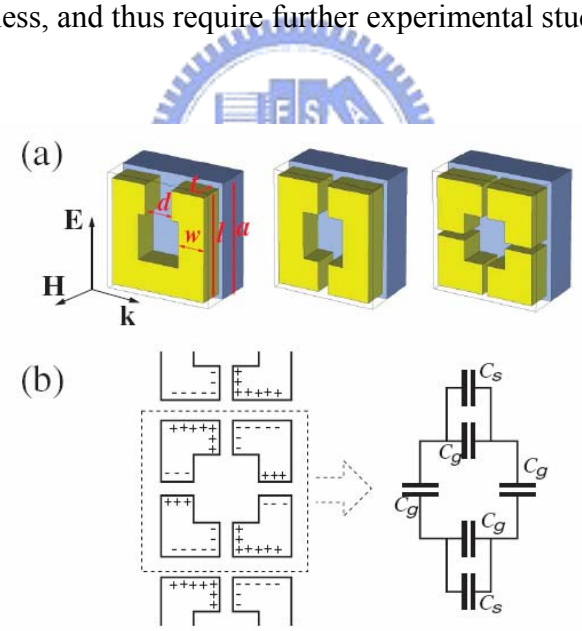

Figure 3-4 (a) The geometries of the 1-, 2-, and 4-cut single-ring SRR. The SRR is made of aluminum, simulated using Drude model (f_p=3570 THz, f_τ=19.4 THz). The parameters of the SRR are side length l=0.914a, width and thickness w=t=0.257a, and cut width d=0.2a, 0.1a, and 0.05a for the 1-, 2-, and 4-cut SRR, respectively. (b) The left panel shows the charge accumulation in a 4-cut SRR, as a result of the periodic boundary conditions in the ***E*** (and ***H***) direction. The right panel shows the equivalent LC circuit describing this SRR. C_g is the gap capacitance and C_s the side capacitance resulting from the interaction with the neighboring SRR. The figure is imaged from [34].

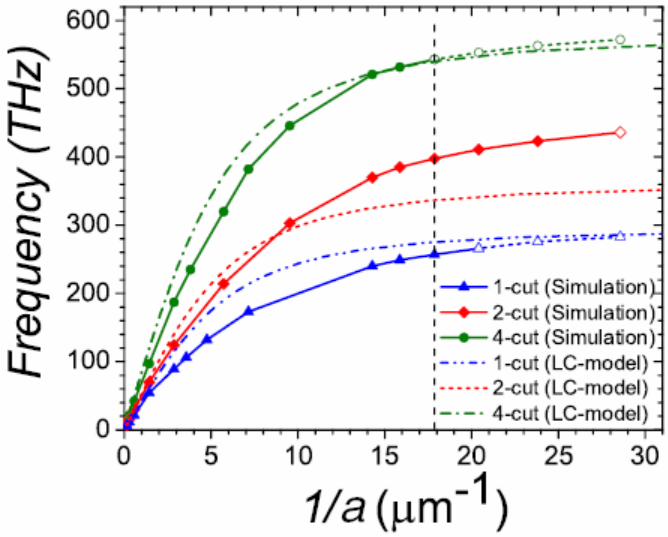

Figure 3-5 Solid lines with symbols shows the scaling of the simulated magnetic resonance frequency f_m as a function of the size of the unit cell a for the 1-, 2-, and 4-cut SRR, respectively. Up to the lower THz region, the scaling is linear, $f_m \propto 1/a$. The maximum attainable frequency is strongly enhanced with the number of cuts in the SRR ring. The hollow symbols as well as the vertical line at $1/a$ =17.9 μm^{-1} indicate that no $\mu<0$ is reached anymore. The nonsolid lines show the scaling of f_m calculated from Eq. 3.1 (*LC* circuit model). The figure is imaged from [34].

Despite the small line width that is theoretically required when scaling down the SRR, there are studies showing that the ratio of the effective sizes of the SRR to the wavelength of the incident beam is around 1, which suggests a wide scale independence [35]. This size tolerance is useful in realizing the metamaterials with negative n in the optical wavelength range.

In most experiments, the transmission is measured at a fixed incident angle for a certain range of wavelength. However, in [35], the incident angle was tuned while the wavelength was fixed by choosing different laser sources. Lasers with the output wavelength of 10.86 μm and 9.43 μm were used because the characteristic size of the SRR (10.48μm) was in between these two wavelengths. The transmission results were shown in Figure 3-6 (a) and (b). At 90° tile angle (in-plane incident) the transmission was expected to peak since the direct contribution of the incident beam to the detector

became dominant, as can be seen in the case of Al-coated planar Si (gray line). However, when the SRRs were patterned on the substrate, absorption at in-plane incident occurred (black line). Although the absorption of parallel polarization at 9.43 μm is less significant than that at 10.86 μm, it is still observable, showing a great size tolerance. The coherence of the laser may be critical to the onset of resonance. Moreover, an 808 nm laser was used to cross-check the rapid oscillation near the non-resonance region caused by the Fabry-Perot effect, as shown in Figure 3-6 (c). Here, neither the rapid oscillation nor the magnetic response appeared. The transmission through Si at wavelength below 1μm is extremely low due to high loss. And the incident wavelength is beyond size tolerance.

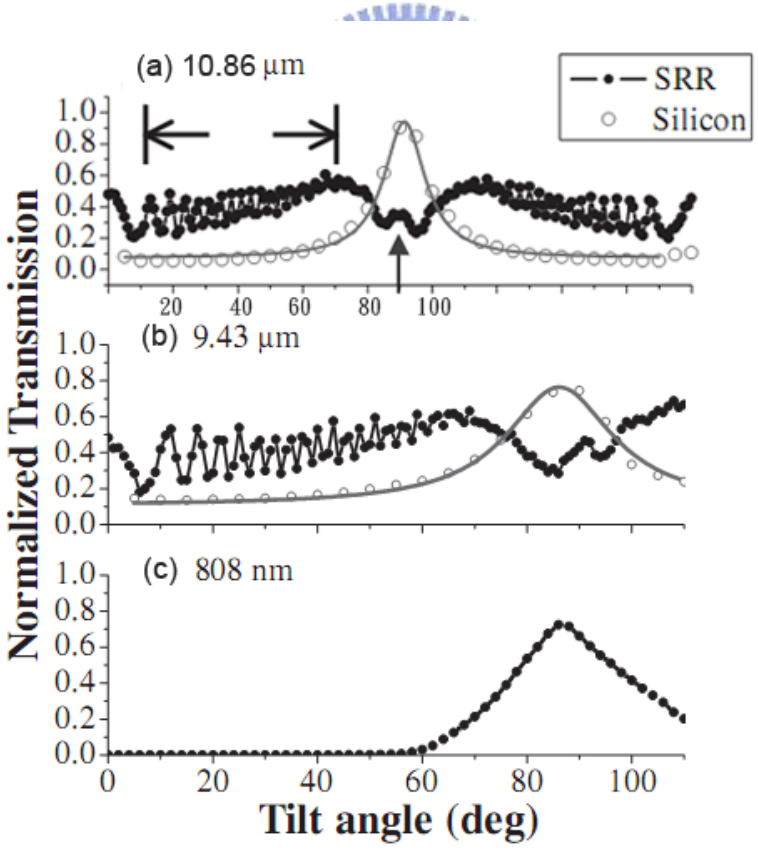

Figure 3-6 Normalized transmission of the SRRs. Data of the Al-coated planar Si is presented for reference. The operating wavelength is (a) 10.86 μm, (b) 9.43 μm and (c) 808 nm, and the laser power on the sample is ~100mW. The figure is imaged from [35] and edited

3.2 Patterns of SRR

3.2.1 Unit Cell Size of SRR

There are typically two interested frequency ranges when applying for bio-sensing. One is the visible light region and another is the middle infrared region (MIR) around 10 μm. The former is valuable due to its ease to observe. Also, the EM wave energy in this region (~2eV) is able to excite the transition between two orbital bands (e.g. HOMO and LUMO), such that fluorescence of bio-molecules might be enhanced when applied to periodic metal patterns. This so-called metal-enhanced fluorescence (MEF) has a promising potential in detecting bio-molecules. The later, on the other hand, induces energy approximately equal to that of molecular bonding (~0.1eV). This is helpful in "fingerprint" detection of bio-molecules. It would be rather difficult to design SRRs that operate in the visible light region using existing fabrication technology, since it requires really small line-width. Instead, by fabricating SRRs with the unit cell size about 1 μm, it is possible to obtain LH behavior at around 10 μm, which might further excite magnetism or change in bonding configuration, and thus achieve bio-sensing. Moreover, as mentioned at the beginning of this chapter, this thesis work aims at studying the scaling of the electric and magnetic resonance frequency for nano-scaled SRRs. Considering both intentions, five unit cell sizes have been chosen in our experiment: 600nm, 900nm, 1200nm, 1500nm, and 1800nm.

For a square single-ring SRR shown in Figure 3-7, ω_m is proportional to $1/l$ while ω_0 depends only on sides parallel to the electric field, following approximately the relation, $\omega_0 \propto a/\sqrt{l_E}$. Thus ω_0 shows a weaker dependence than ω_m on l in Figure 3-8 (a) and is constant in Figure 3-8 (b) where only l_k was tuned. The different dependence of ω_m and ω_0 on a/l allows the relative position of ω_m and ω_0 to be controlled.

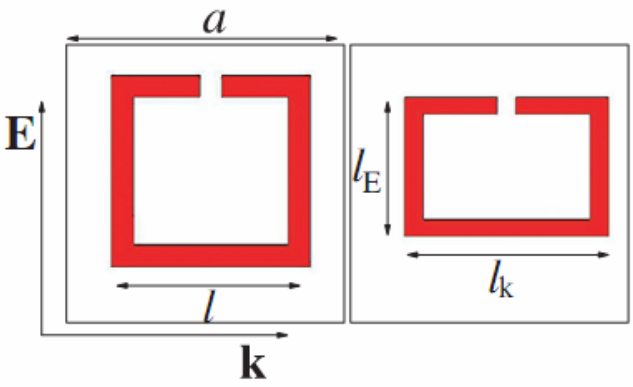

Figure 3-7 Two single-ring SRRs, a square one and an orthogonal one, are shown, together with the external electric field ***E***, propagation directions *k*, lattice constant *a*, side length of the unit cell *l*. The lengths, l_k and l_E, of the two sides of the orthogonal SRR are also shown. The figure is imaged from [20].

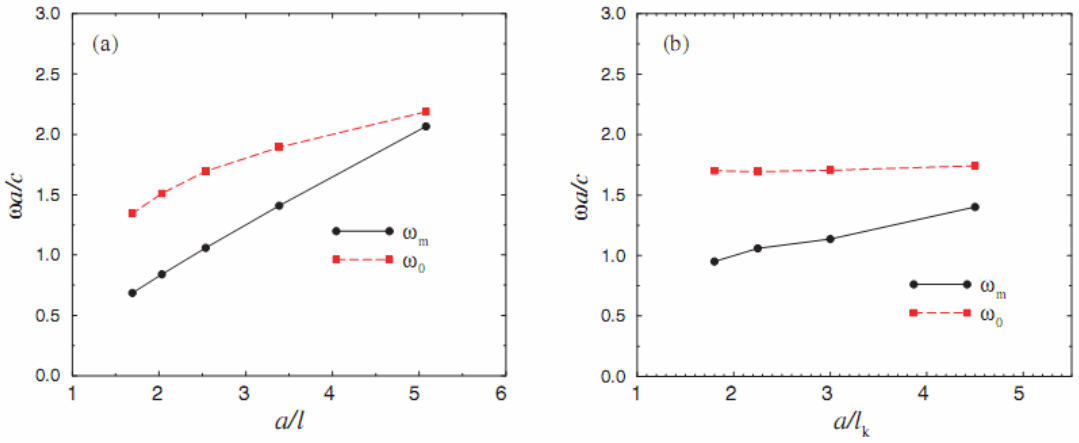

Figure 3-8 (a) ω_m and ω_0 (in units of c/a, where c is the vacuum light velocity and a is the lattice constant of the unit cell) versus a/l for a square single-ring SRR (see the left drawing of Figure 3-7). l is the SRR side length. (b) ω_m and ω_0 (in units of c/a) versus a/l_k for an orthogonal single-ring SRR (see Figure 3-7, right panel). l_k is the length of the SRR side which is perpendicular to the incident electric field, ***E***. The figure is imaged from [20].

3.2.2 Square Single-ring SRR

For circular and square single-ring SRRs with the same geometric size, metal characteristics, and gaps, the magnetic resonance frequency of the square SRR is a little lower than that of the circular one (Figure 3-9). Nevertheless, the ω_m and ω_0

dependences on the system parameters are the same in both cases [20]. However, for simplicity of both the nanofabrication and the corresponding transmission calculations, the square form was chosen in the present work.

To make a comparison between single- and double-ring SRRs, the transmission through the double-ring SRR and that through only its outer or its inner ring SRR are presented in Figure 3-10. It can be seen that the lower magnetic resonance frequency of the double ring is essentially due to the outer ring, but with a relatively small downwards shift. This shift is caused by the additional capacitance between the rings. The second dip of the double-ring corresponds essentially to the magnetic resonance of the inner ring with a small upwards shift. The strength of this resonance is sometimes very small, indicating that the magnetic response of the inner ring is screened by the presence of the outer one. This happens mainly in the case where the electric field is parallel to the continuous side of the SRR.

There are mainly two reasons why double-ring SRR has been the preferable form when studying LH behavior in microwave region. One advantage of the double-ring SRR compared with its outer single-ring SRR is that the magnetic resonance frequency occurs at a relatively lower frequency, thus there is a higher probability for the magnetic response to lie in the $\varepsilon<0$ regime in the combined system of SRRs and wires. Another advantage is that the array of double-ring SRRs possesses a stronger magnetic resonance, which might lead to a more robust LH peak. Although the desired condition is to make ω_m as low as possible, one has to pay special attention to that the lowering of ω_m is not associated with a weakening of the strength of the magnetic response of the SRR.

As the SRR size decreases, the actual capacitance becomes larger than estimation because Gupta's formula is valid only when the thickness of the ring is negligible. To reduce the geometrical capacitance of the structure, employing an SRR consisting of a

single ring is advantageous [33]. It has been shown that it is not necessary to use the conventional double-ring SRR proposed by Pendry *et al*., a single-ring SRR with a cut also behaves as a magnetic resonator. This simplifies the fabrication, especially for small structural sizes, and potentially reduces dielectric losses, since the fields get strong only around the cuts but not between the rings anymore [34]. Therefore, for nano-scaled unit size we focus our study on single-ring SRRs

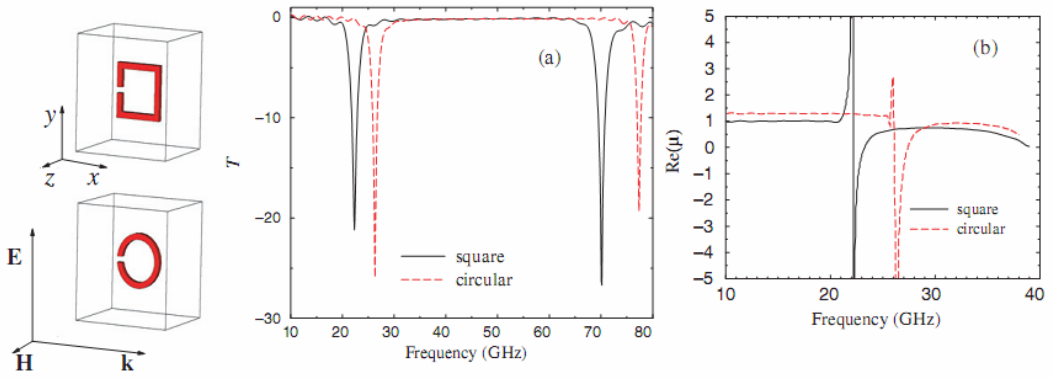

Figure 3-9 (a) Transmission (dB) versus frequency for one single-ring square (solid curve) and circular (dashed curve) SRR. The corresponding designs are shown on the left side of the panel. (b) Re(μ) as a function of frequency for the single-ring square (solid curve) and circular (dashed curve) SRR, at frequencies around the magnetic resonance frequency. The figure is imaged from [20].

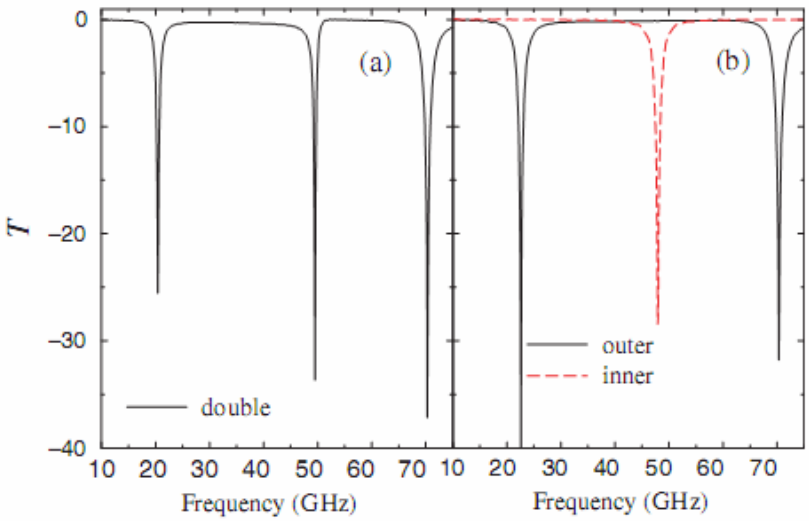

Figure 3-10 Transmission (dB) versus frequency for (a) the double-ring SRR and (b) its isolated outer and inner ring SRRs. The figure is imaged from [20].

3.2.3 Geometric Parameters of SRR

Previous parametric studies showed a rather weak dependence of EM response of SRRs on the metal width and gap width. Referring to the SRRs utilized in ref. 6, 36, and 37, a square single-ring SRR is designed to have a line width that is one fifth of the side length and a gap width equal to the line width for simplicity in layout. For example, for the smallest unit cell size 600 nm, its line width and gap width is then 120 nm. In addition, corresponding CRR and 2-cut SRR are designed to demonstrate the magnetic resonance and the electric coupling effect. The layout designs of 1-cut SRR, 2-cut SRR and CRR in our experiment are drawn in Figure 3-11.

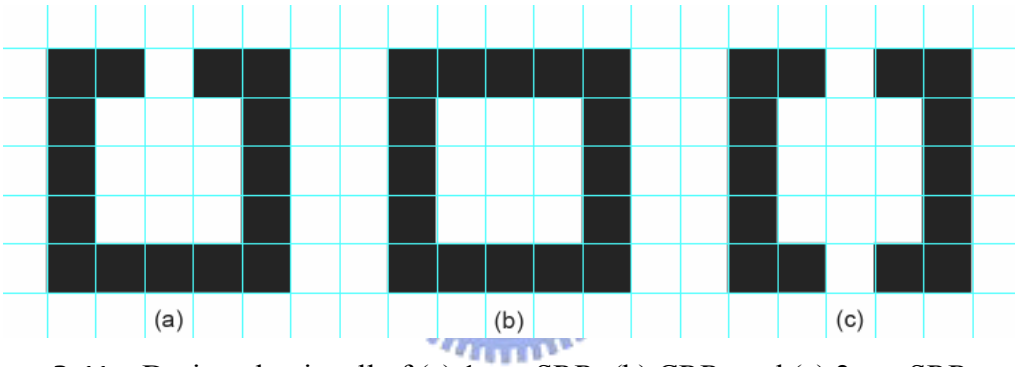

Figure 3-11 Designed unit cell of (a) 1-cut SRR, (b) CRR, and (c) 2-cut SRR.

3.3 Arrangement of SRR

With increasing lattice constant *a*, the resonances narrow to some extent because of the reduced interaction between the SRRs, but their spectral position remains essentially unchanged [4]. Figure 3-12 are the measured transmission and reflection spectra for different lattice constants. In each row of this figure, an electron micrograph of the sample is depicted on the right-hand side. The two polarization configurations are shown on top of the two columns. In the first row (A and B), the lattice constant of the SRRs is a = 450 nm; in the second row (C and D), a = 600 nm; and in the third row (E and F), a = 900 nm. In the last row (G and H), results for

CRRs with a = 600 nm are shown. Note that the combination of these spectra unambiguously shows that the magnetic resonance occurs at about 3 μm wavelength (highlighted by the gray areas).

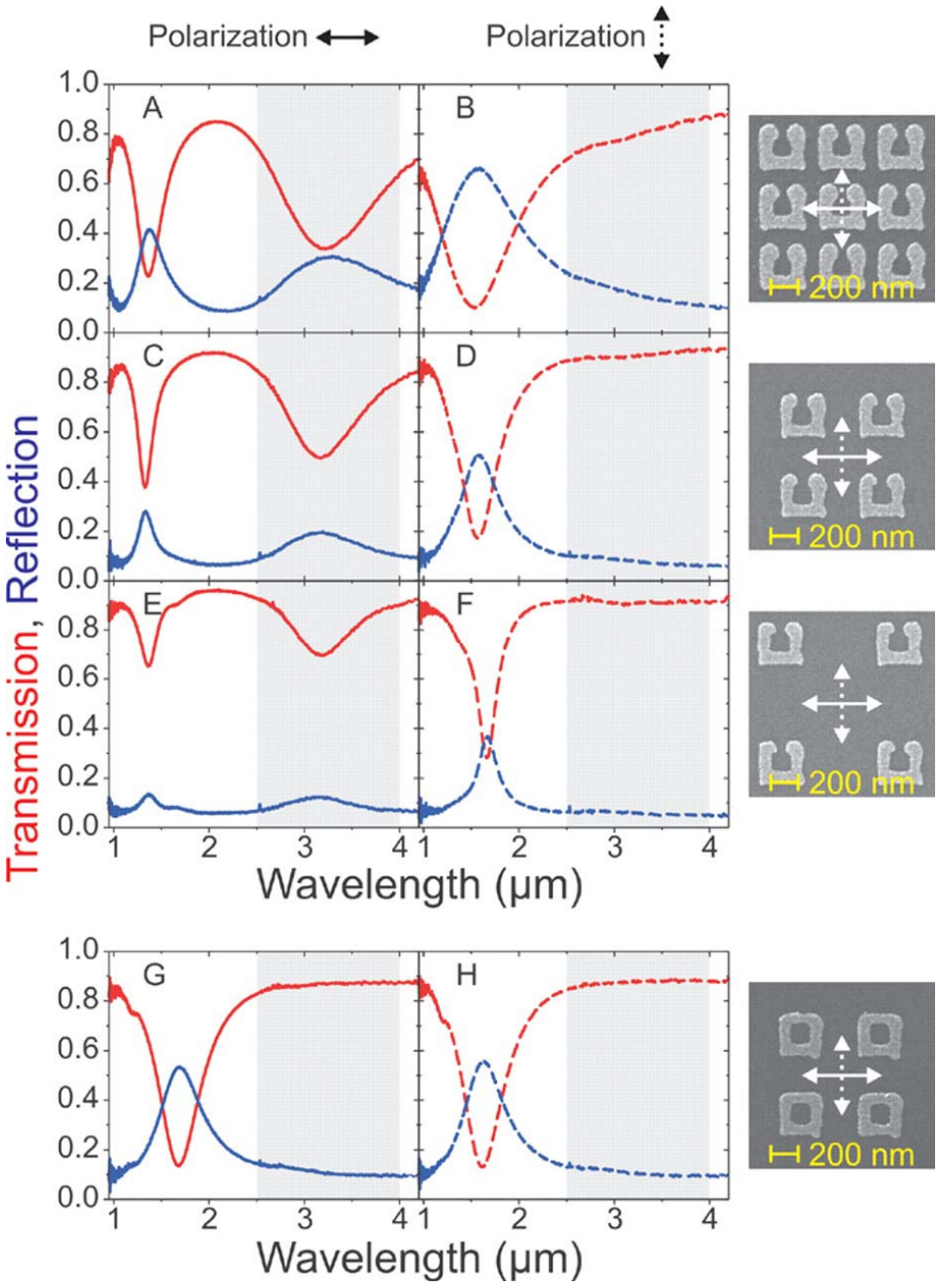

Figure 3-12 The measured transmission (red) and reflection (blue) spectra with two polarizations for (A) to (F) with different lattice constants of SRRs, and (G) and (H) of CRRs. The figure is imaged from [4].

Considering the unwanted side effect coming from outward area around the sample, the SRR array should be larger than the beam size of the incident light when measuring the transmission or reflection. The number of SRR elements gets huge, however, as the device size reduces to the nano-scale if the array area remains the same. This will cause difficulty in fabrication and induce defects easily. Usually, the SRR array has a separation distance smaller than one unit cell size. To enlarge the array size by "diluting" the SRR elements while maintaining adequate interaction among them, a separation distance equal to that of the unit cell size has been chosen. For example, for the smallest unit cell size 600 nm, the separation distance is also 600 nm, which implies a lattice constant of 1200 nm. This is also for simplicity in layout drawing and related calculations.

3.4 Material Used in SRR Design

For mm-scaled SRR, cupper is printed on the circuit board (so-called PCB) [13, 17, 19. 22. 26]. As scaling down, other metals have been utilized such as gold [4, 23, 38], silver [23, 36], aluminum [23, 35, 37], and nickel [38]. Aluminum is the most commonly chosen metal in silicon VLSI and has a higher bulk plasma frequency than gold or silver [23]. However, in this thesis work, gold is chosen to form the SRR array due to its low loss and acting closer to Drude model even at very high frequencies [34]. Moreover, it is widely utilized for its inertness, resistance to oxidation, capable of providing a platform for bio-molecular immobilization such as self-assembled monolayer (bio-compatible).

As mentioned before, LHMs were first fabricated on PCB. Later, silicon [23, 35, 37, 38] has been utilized as a common substrate. Recently, LHMs using cupper pattern on glass have been reported [39, 40]. In this thesis work, glass is chosen because it

enables transmission measurement in the interested frequency range, i.e. around 10 μm while silicon exhibits a strong absorption at 9 μm. Other ways to benefit transmission measurement include "releasing" pattern from the substrate [36, 38]. By choosing proper photo resist and sacrifice layer, SRRs can be embedded in a transparent sheet of PR.

Table 3-1 summarizes the design of the ring resonators in our experiment.

Table 3-1 The parameters of the square single-ring SRR designed for this thesis work. The metal is goal and the substrate is glass. For each SRR size, corresponding CRR and 2-cut SRR are also designed and studied.

unit cell size (nm)	600	900	1200	1500	1800
line width (nm)	120	180	240	300	360
gap size (nm)	120	180	240	300	360
lattice constant (nm)	1200	1800	2400	3000	3600
array size (μm)	90	90	90	90	90
array size (number)	75×75	50×50	38×38	30×30	25×25

Chapter 4

Fabrication and Results

4.1 Pre-patterning

The two sides polished 0.7 mm thick 4" Corning 1737 glass wafers were cut into 2×2 cm^2 pieces as the substrates. Each piece of glass was then cleaned through the following standard process:

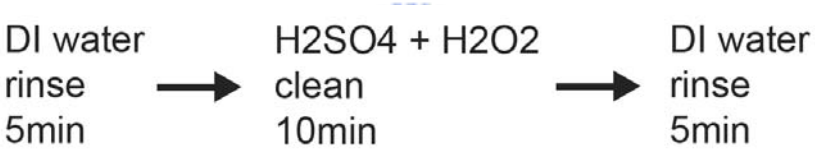

The positive photoresist (PMMA or ZEP520) was coated on the substrate by spin-coater. The glass was thereafter baked at 170-180° C for a while in order to enhance adhesion between the PR and the substrate. Because glass is nonconductor, a thin layer of E-spacer was coated on the PR after the bake for preventing the charging effect and thus enabled the successive e-beam exposure. The E-spacer is considered as a better choice for improving electrical conduction than the use of ITO because of its simple process and smooth surface achieved. Usually the aspect ratio of PR patterns should not exceed 5. If the aspect ratio value is too high, the pattern will collapse during the drying process after rinsing. For the line width of 120-360 nm, the resist thickness of 300-400 nm is reasonable. Three recipes were used for coating the PR and E-spacer layers, which are schemed as below:

(1) Resulted PR thickness: 400nm

(2) Resulted PR thickness: 300nm

(3) Resulted PR thickness: 300nm

The hot plate baking time in case (3) was extended to about 150sec for improving the adhesion and conformity of the PR layer.

4.2 Patterning with E-beam Lithography

Patterning was completed by e-beam lithography using an Elinoics ELS-7500EX high precision compact e-beam writing system. When the electron beam strikes a point on the resist that covers the specimen substrate, the spatial distribution g(r) of the electrical charge provided by the beam irradiation over the resist is approximated by the sum of the two Gaussian distribution functions as follows:

$$g(r) \propto g_f(r) + \eta g_b(r) \tag{4.1}$$

where $g_f(r) = 1/(\pi\sigma_f^2)\exp(-r^2/\sigma_f^2)$ is the forward scattering distribution mainly due to the resist, $g_b(r) = 1/(\pi\sigma_b^2)\exp(-r^2/\sigma_b^2)$ is the backward scatting distribution mainly due to the substrate, and η is the sensitivity ratio between the backward and forward scatting. For example, when a fine electron beam of V_{acc}=50keV strikes the

Si substrate covered with a 300nm thick resist, the mean square radii of the forward scattering and backward scattering will approximately be σ_f=13nm and σ_b=10μm respectively. This means that the term $g_f(r)$ changes sharply in relation to the distance r, whereas the term $g_b(r)$ constitutes a near-constant background in g(r). Accordingly, one only needs to consider σ_f when exposing nano-meter scaled patterns. Likewise, when exposing patterns of several micron-meters in size, one only considers σ_b. Due to this Gaussian beam feature, the designed pattern should not have the same width as the target pattern, or the resulted pattern would be wider than the target pattern (e.g. by 13 nm for the Si substrate) at each side.

The field size for the ELS-7500EX can be varied between 75-600 μm, which should be chosen according to the position resolution requirement and the exposure time limit. Namely, a smaller field size constitutes a finer position resolution, while demands a linger exposure time. Given the pixel size and resist sensitivity, the electric charge required for sensitizing the pattern could be calculated. For example, for a 600 μm field size with 60,000×60,000 scan steps, the pixel size is 10 nm. And for ZEP520, the resist sensitivity is 30-60 μC/cm^2 when being exposed with V_{acc}=50keV. It then needs $60\mu C/cm^2 \times (1\times10^{-6}\,cm)^2 = 6\times10^{-17}\,C$ of charge to sensitize the pixel of PR. The beam current and exposure time can then be assigned to achieve enough charges. When using a larger beam current, a shorter exposure time is needed, while the electron forward scattering will also be larger, resulting in a larger beam diameter, i.e. eventually a larger obtained line width. Test exposure should be done to find the suitable exposure time, which usually differs from the preliminary estimate. Factors that affect the optimum exposure time include: (1) substrate material, (2) background exposure distribution due to the backward scattering, and (3) pattern arrangement.

In order to optimize the exposure condition of this e-beam lithography system, exposure tests were made with several different conditions, i.e., two beam currents

(50/ 100 pA) and three field sizes (150/ 300/ 600 μm), while a scan steps of 60,000×60,000 was fixed. It was found that when the beam current and field size were both large, the position resolution was poor especially for a small line width, as shown in Figure 4-1 and Figure 4-2. There were certain shifts for both vertical and horizontal positions, which were more severe for smaller line widths and became less observable for larger line widths. This shift could be corrected by adjusting the pattern design. Figure 4-3(a) shows the modified layout for a SRR unit cell, and the improved exposure results are shown in Figure 4-3(b) and Figure 4-4. Notice that the sharper edges of large line width patterns (Figure 4-2 and Figure 4-4) compared with those of small ones (Figure 4-1 and Figure 4-3 (b)) revealed the resolution feature of e-beam lithography. Furthermore, overexposure was a serious problem for large beam current and field size. When the beam current and field size were small, the line width variation was small, as soon as reaching an enough dosage. This gives a better line width control of the target pattern. The chosen exposure recipe for our experiment is list in the following table:

Table 4-1 Exposure recipe

accelerate voltage	50 (keV)
field size	150 (μm)
scan step	60,000×60,000 (pixel)
beam current	50 (pA)
dose time	0.85 (μsec/dot)

During the exposure experiments, strips of copper tape were attached from the edge of the glass to the metallic holder for the ground connection, to ensure the elimination of charge accumulation.

After e-beam exposure, the specimens were first rinsed by DI water for removing

the E-spacer, and dried by blowing nitrogen gas. The developer used depended on the PR. For ZEP520, the specimen was soaked in N50 for 45 seconds, but for PMMA, the specimen was soaked in an organic solution of MIBK:IPA=1:3 for 70 seconds. The IPA rinsing was then used, followed by nitrogen blow for drying.

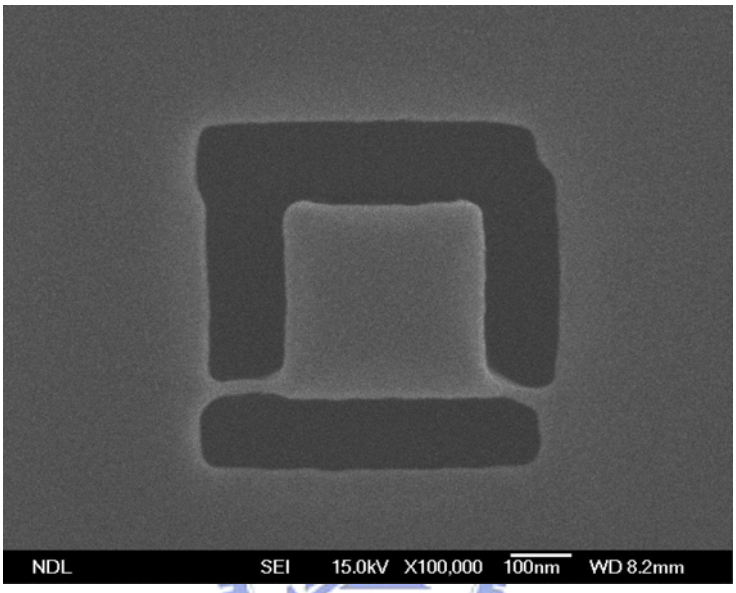

Figure 4-1 The SEM image of a shifted CRR with line width=120 nm, beam current=100 pA, field size=600 μm, dosage=1 μsec/dot, PR coating recipe (2).

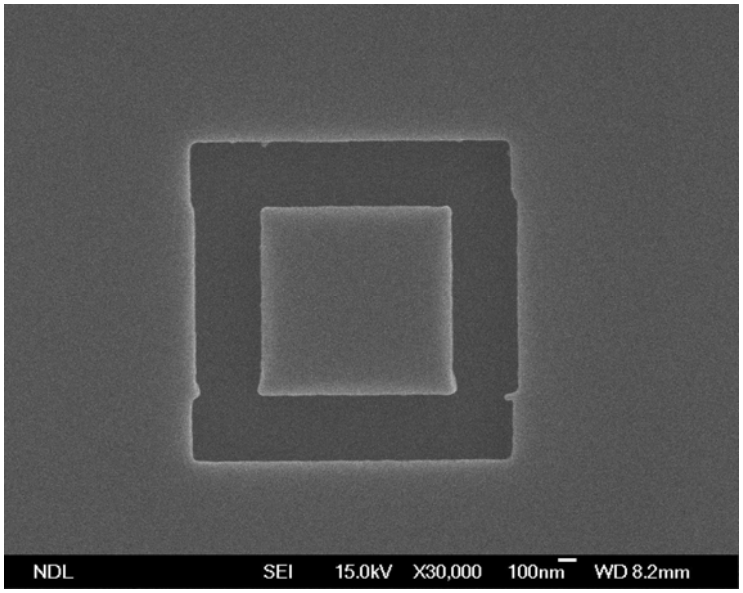

Figure 4-2 The SEM image of a shifted CRR with line width=360 nm, beam current=100 pA, field size=600 μm, dosage=1 μsec/dot, PR coating recipe (2).

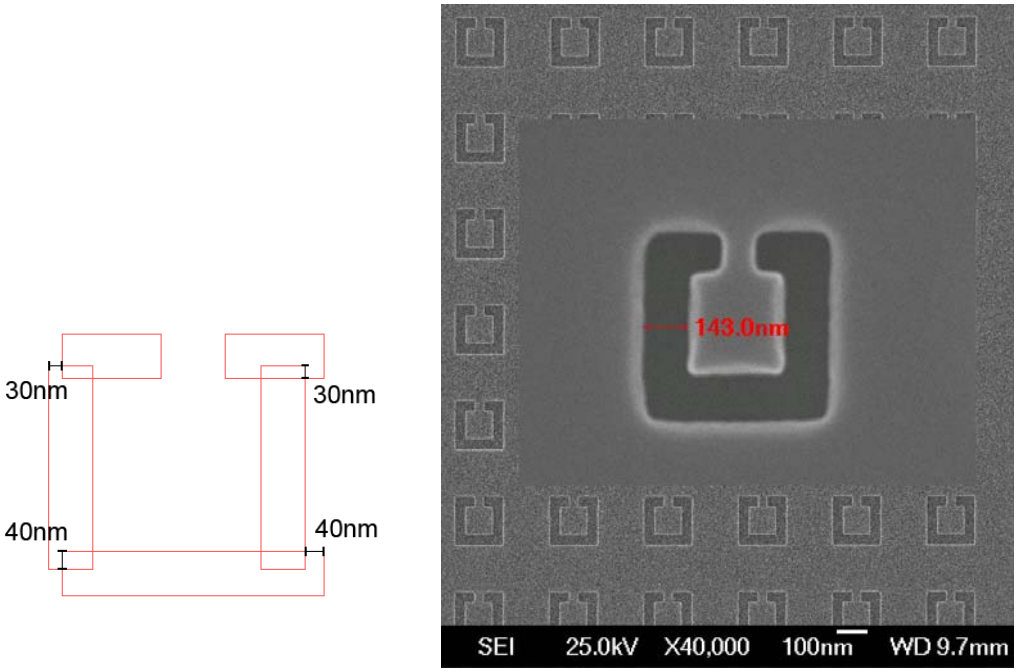

(a) (b)

Figure 4-3 (a) Adjusted layout for a SRR with line width=120 nm. (b) The SEM image of the adjusted SRR after development. Line width=120 nm, beam current=100 pA, field size=600 μm, dosage=0.9 μsec/dot, PR coating recipe (2).

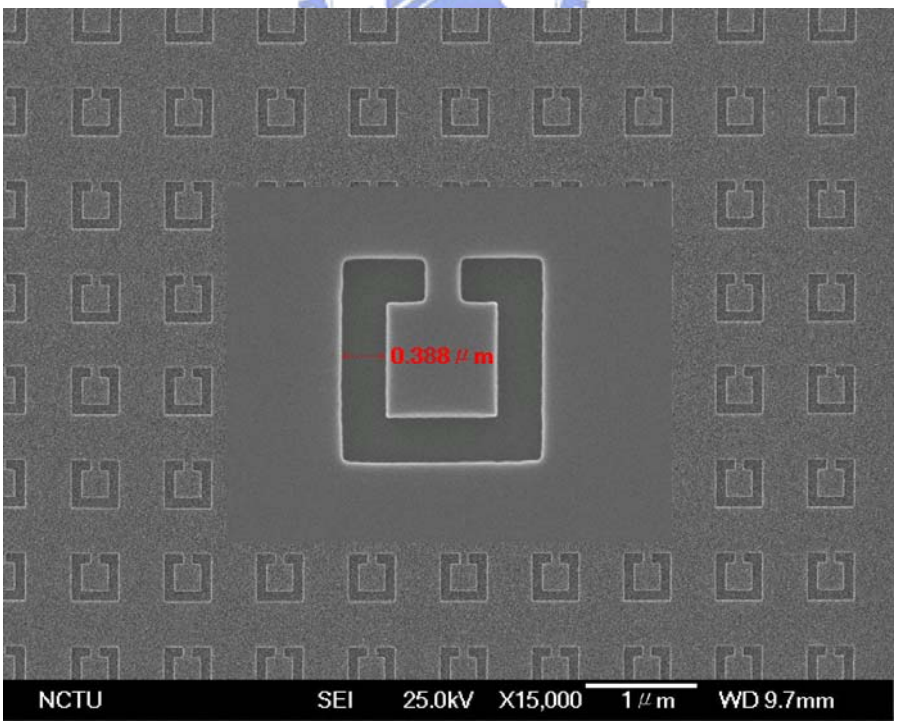

Figure 4-4 The SEM image of the adjusted SRR after development. Line width=360 nm, beam current=100 pA, field size=600 μm, dosage=0.9 μsec/dot, PR coating recipe (2).

4.3 Thermal Evaporation of Gold and Lift-off

A gold thin film was deposited on the resist-patterned glass substrate by thermal evaporation. Generally, the thickness ratio between the photo resist and the metal thin film (i.e. Au) must be larger than 10:1 to ensure the lift-off process. For the PR thickness of 300-400 nm, a metal thin film under 30 nm was required. Notice that the metal film can not be too thin, namely, it should be thicker than the skin depth. The bulk resistivity of Au is 2.44μΩ-cm, so that its skin depth at 30THz is about 10nm. Therefore a gold thin film of 30nm thickness should be suitable for our devices. For the Au deposition, the background pressure in the vacuum chamber was pumped down to 2×10^{-6} Torr prior to the process, and would be slightly increased to $2.6-2.7\times10^{-6}$ Torr during evaporation. To physically remove the unwanted residual PR in the pattern region after development, oxygen plasma treatment was engaged prior to the Au thin film deposition. For PMMA, the removal rate was about 10 nm/min, and the duration of oxygen plasma process was about 1-2 minutes without excessively decreasing the PR thickness. Au evaporation was achieved by resistive heating of the target when passing 100A current, and the deposition rate was about 0.14-0.15 nm/sec. The deposition time was controlled by a coating thickness gage, and during the process the temperature of the chamber was about 100°C.

The lift-off process was performed by soaking the specimens in the ZEP520 PR remover, ZDMAC for about 10 minutes, and then rinsed by IPA and DI water. A square was drawn around the patterned area by a tweezers prior to dipping in ZDMAC, and the specimens were gently shaken by hand during the lift-off process to accelerate the peeling of the PR. The results of the lift-off process were examined by both optical microscope and SEM. Our experiment showed that the quality of lift-off result varied according to different PR coating recipes. Figure 4-5 shows the

successful results of a lift-off process for recipe (1), in which only PR in the patterned region was removed, thus the Au layer above was lifted off. The charging effect induced by the uncovered glass can be seen evidently, this is a useful indication for a completed lift-off process. Figure 4-6 shows the results for a failed lift-off process for recipe (2). A possible reason was the residual PR in the patterned region caused by an incomplete development process, such that the Au pattern was partly peeled off during the lift-off process because of poor adhesion. Figure 4-7 to Figure 4-21 show the fifteen samples contained Au patterns that were processed using the above mentioned lift-off technique from recipe (3). Finally, Figure 4-22 is the 3D SEM image of a SRR array. The overall results were pretty good. Among thousands of patterns in each array, less than five were damaged. Some specimens were immersed in acetone and sonicated, in order to shorten the process time. This process however resulted in poorer completeness of the arrays, i.e. up to ten unit cells came off, which is a more than twice higher damage rate compared to the best one. To summary, our fabrication experience and results showed that Au thin film has adequate adhesion on glass that could be survived through the lift-off process, which thus is a feasible way to produce nano-scaled devices for bio-optical studies.

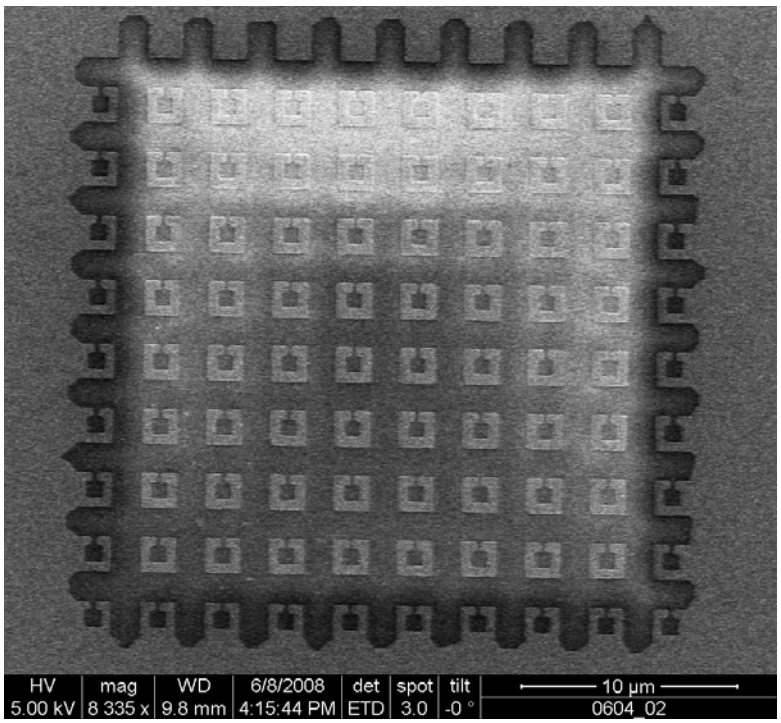

Figure 4-5 The SEM image of a SRR array after lift-off. Beam current=100 pA, field size=600 µm, PR coating recipe (1).

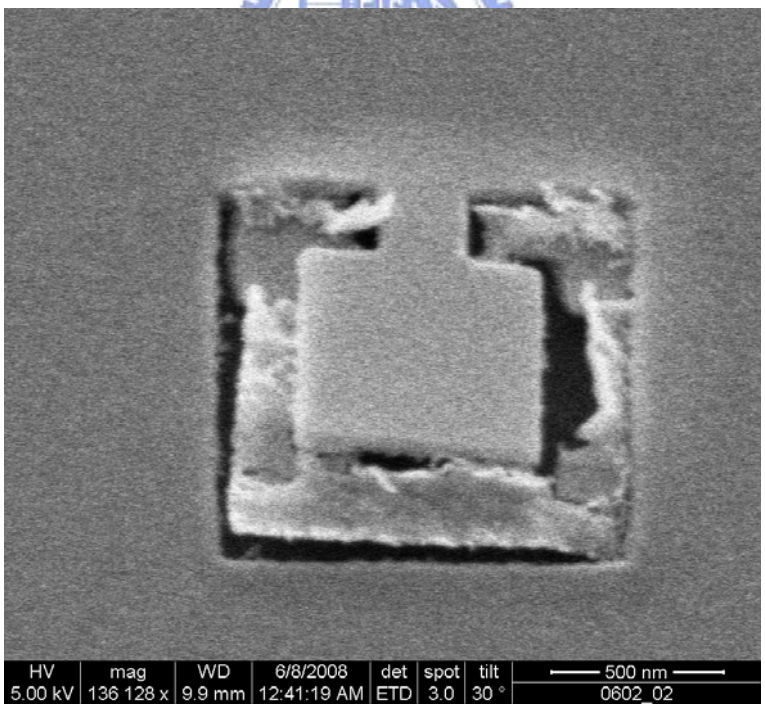

Figure 4-6 The SEM image of a SRR array after lift-off. Beam current=100 pA, field size=600 µm, dosage=0.9 µsec/dot, PR coating recipe (2).

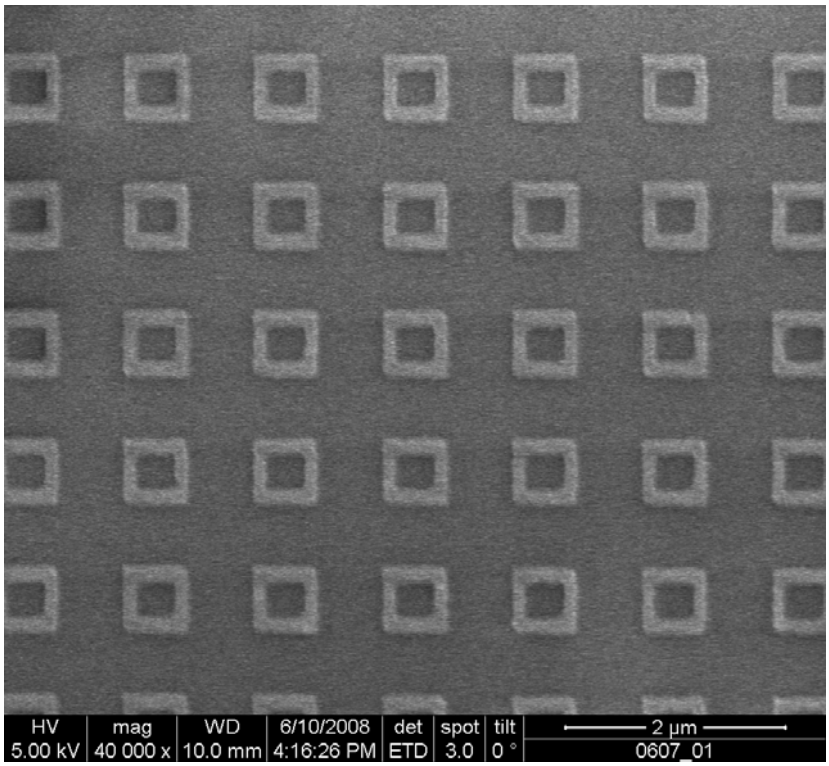

Figure 4-7 The SEM image of a CRR array after lift-off. Line width=120 nm, beam current=50 pA, field size=150 µm, dosage=0.85 µsec/dot, PR coating recipe (3).

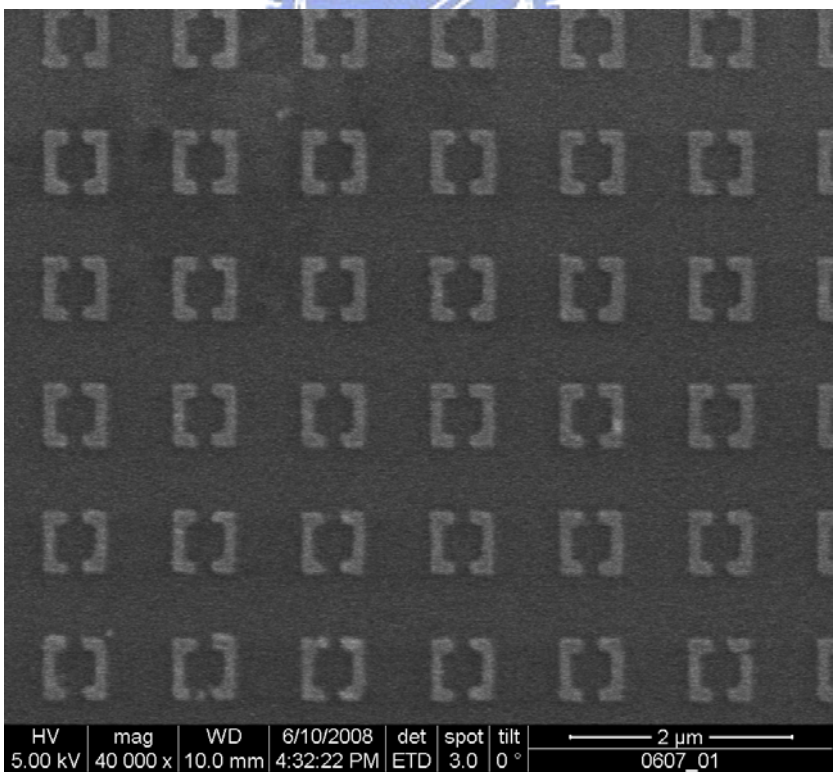

Figure 4-8 The SEM image of a 2-cut SRR array after lift-off. Line width=120 nm, beam current=50 pA, field size=150 µm, dosage=0.85 µsec/dot, PR coating recipe (3).

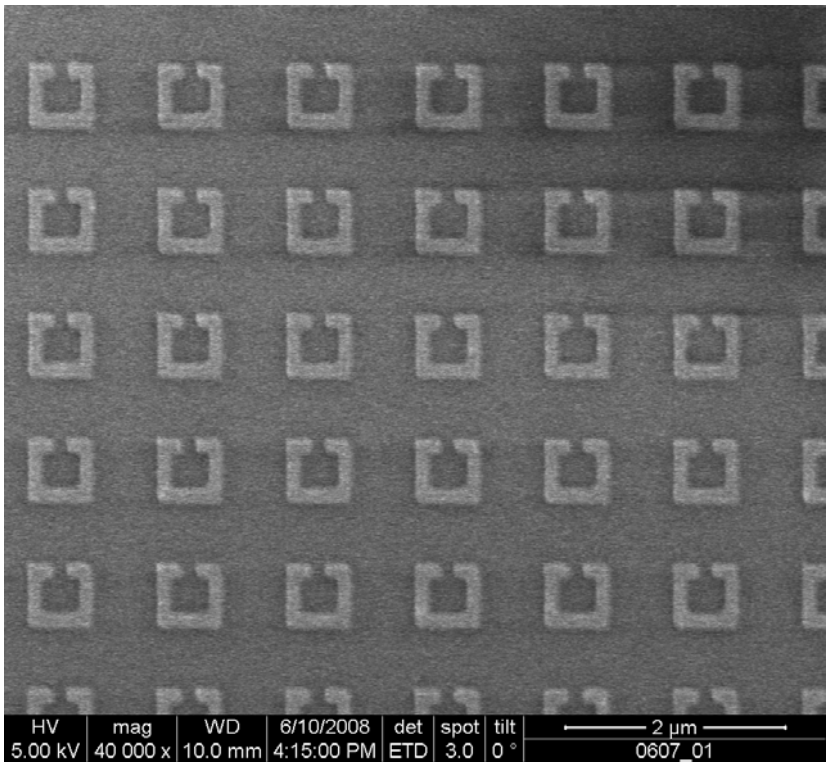

Figure 4-9 The SEM image of a SRR array after lift-off. Line width=120 nm, beam current=50 pA, field size=150 µm, dosage=0.85 µsec/dot, PR coating recipe (3).

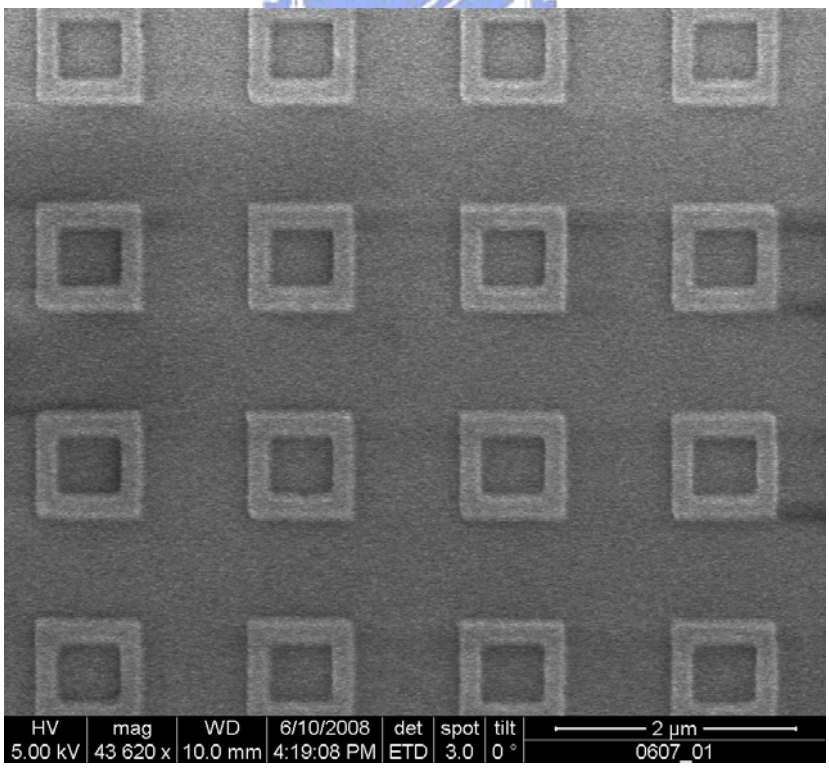

Figure 4-10 The SEM image of a CRR array after lift-off. Line width=180 nm, beam current=50 pA, field size=150 µm, dosage=0.85 µsec/dot, PR coating recipe (3).

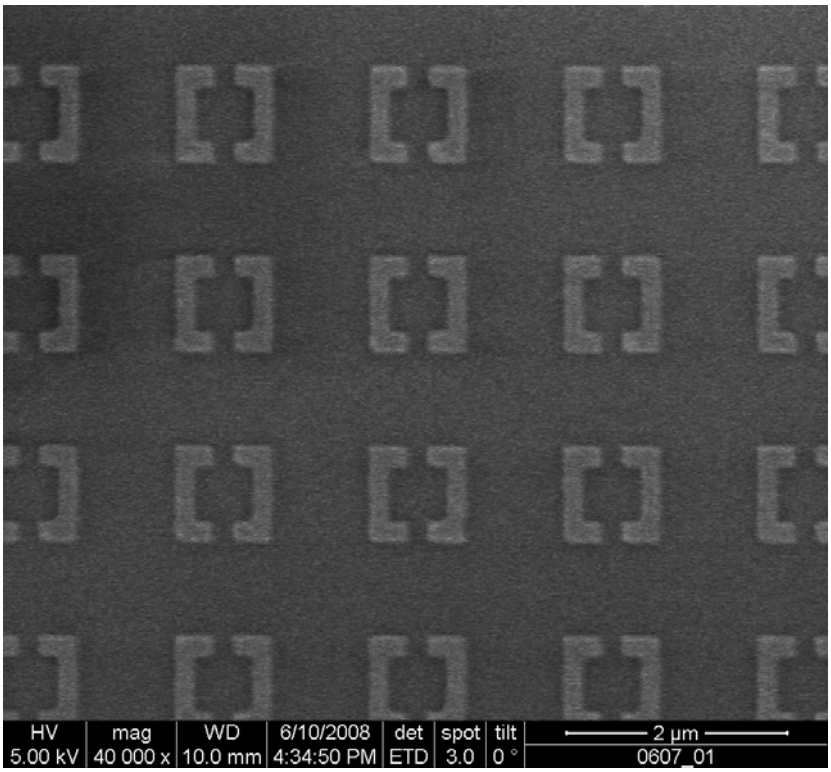

Figure 4-11 The SEM image of a 2-cut SRR array after lift-off. Line width=180 nm, beam current=50 pA, field size=150 µm, dosage=0.85 µsec/dot, PR coating recipe (3).

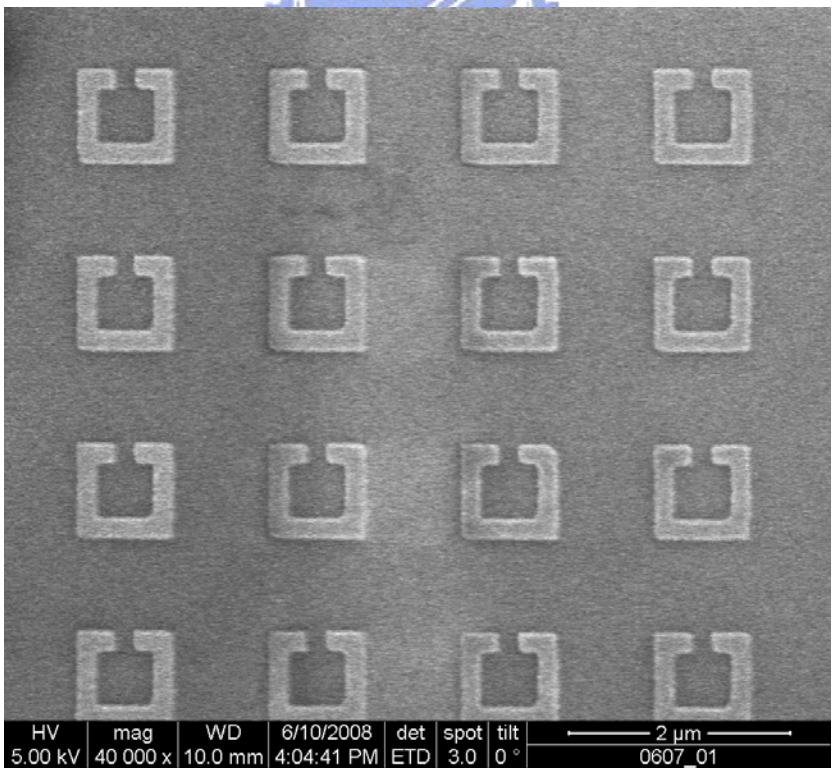

Figure 4-12 The SEM image of a SRR array after lift-off. Line width=180 nm, beam current=50 pA, field size=150 µm, dosage=0.85 µsec/dot, PR coating recipe (3).

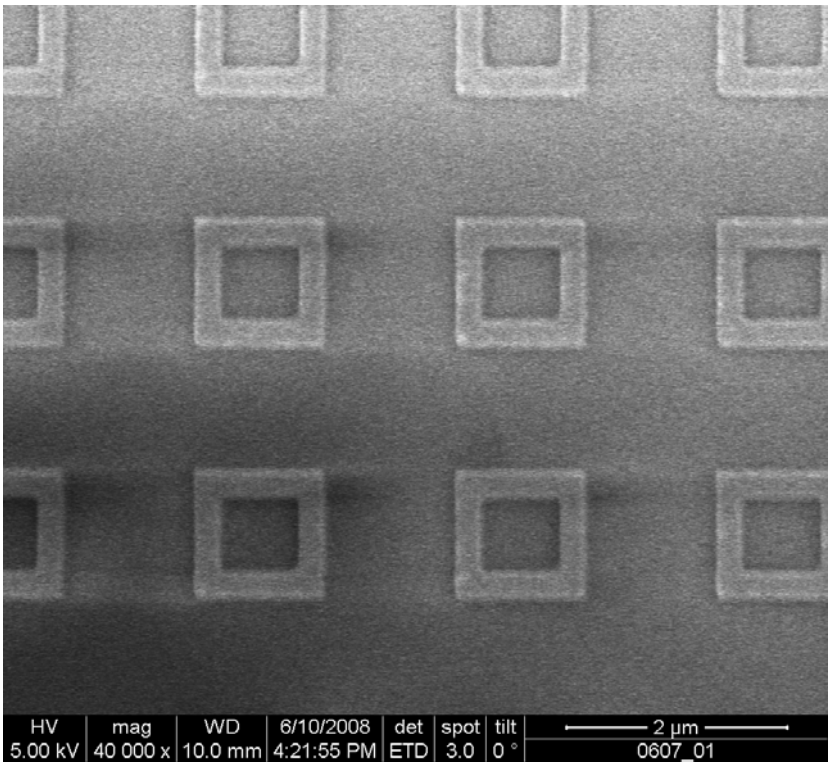

Figure 4-13 The SEM image of a CRR array after lift-off. Line width=240 nm, beam current=50 pA, field size=150 µm, dosage=0.85 µsec/dot, PR coating recipe (3).

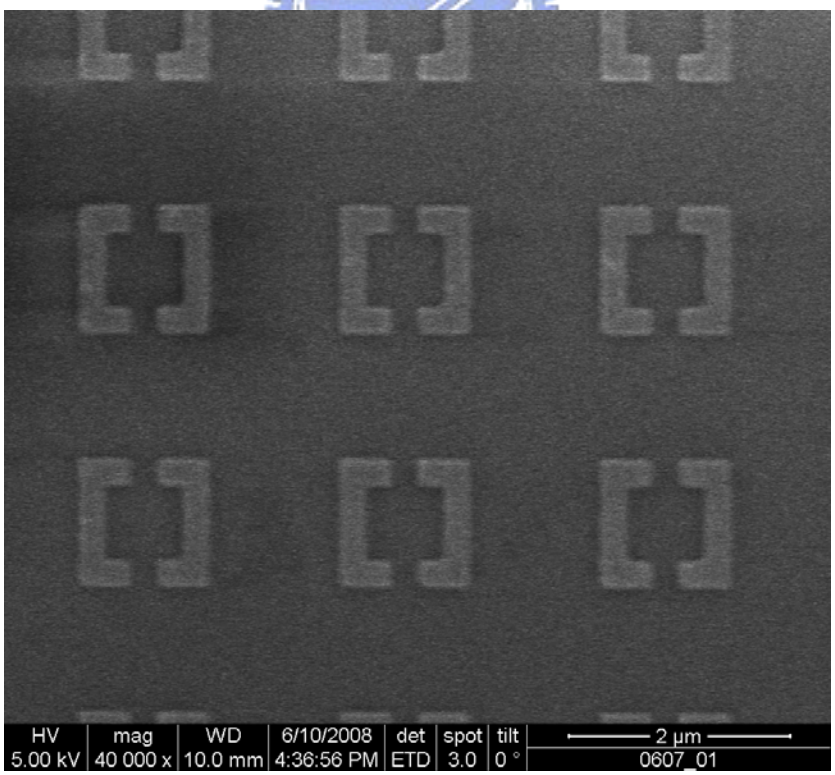

Figure 4-14 The SEM image of a 2-cut SRR array after lift-off. Line width=240 nm, beam current=50 pA, field size=150 µm, dosage=0.85 µsec/dot, PR coating recipe (3).

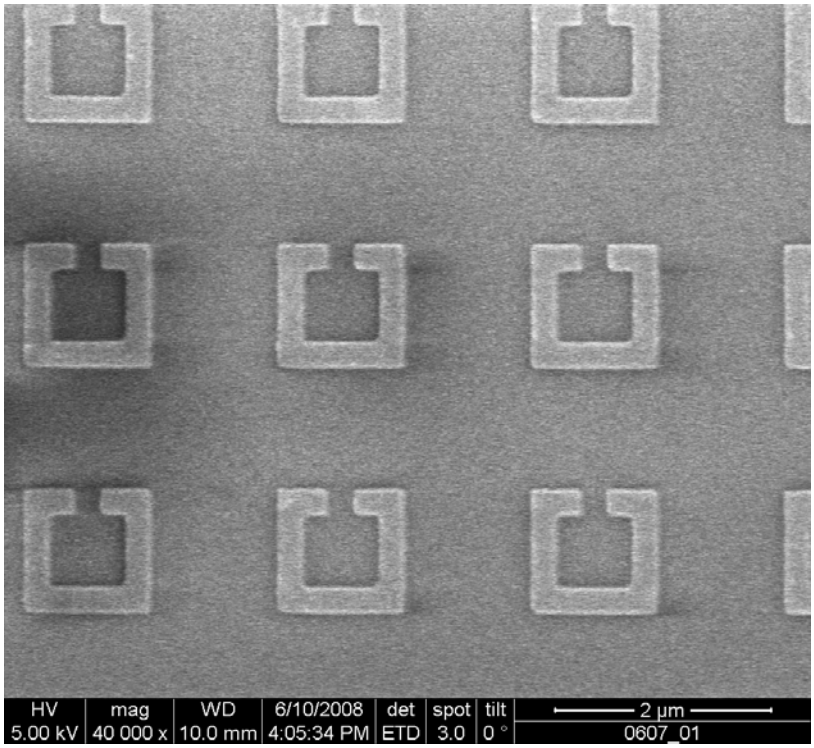

Figure 4-15 The SEM image of a SRR array after lift-off. Line width=240 nm, beam current=50 pA, field size=150 µm, dosage=0.85 µsec/dot, PR coating recipe (3).

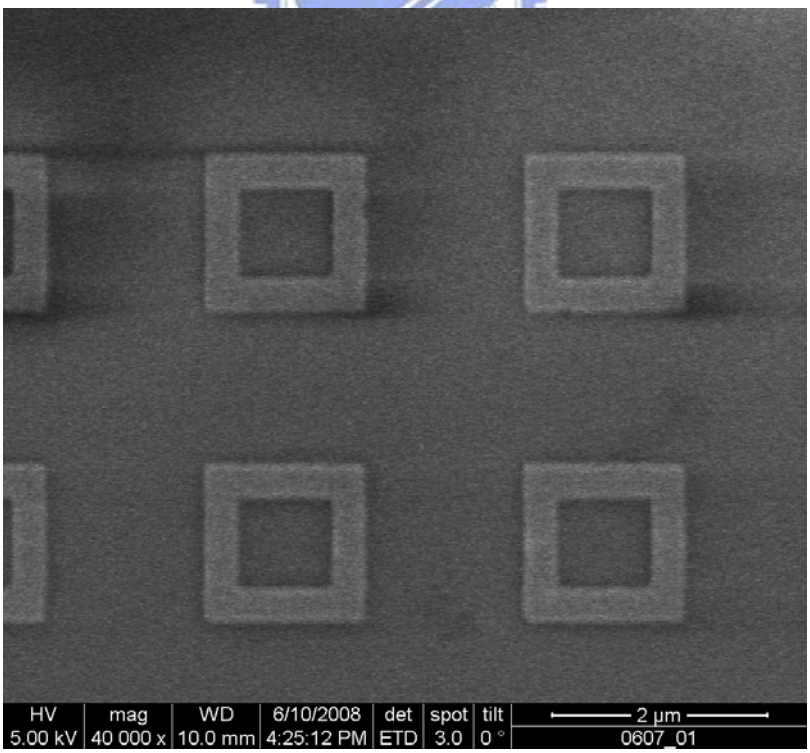

Figure 4-16 The SEM image of a CRR array after lift-off. Line width=300 nm, beam current=50 pA, field size=150 µm, dosage=0.85 µsec/dot, PR coating recipe (3).

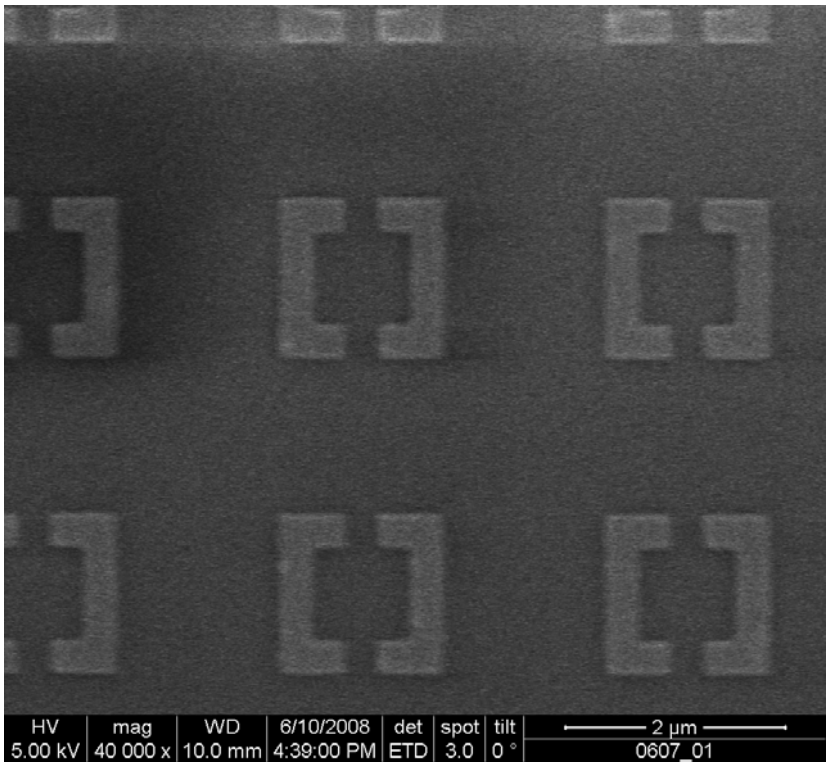

Figure 4-17 The SEM image of a 2-cut SRR array after lift-off. Line width=300 nm, beam current=50 pA, field size=150 µm, dosage=0.85 µsec/dot, PR coating recipe (3).

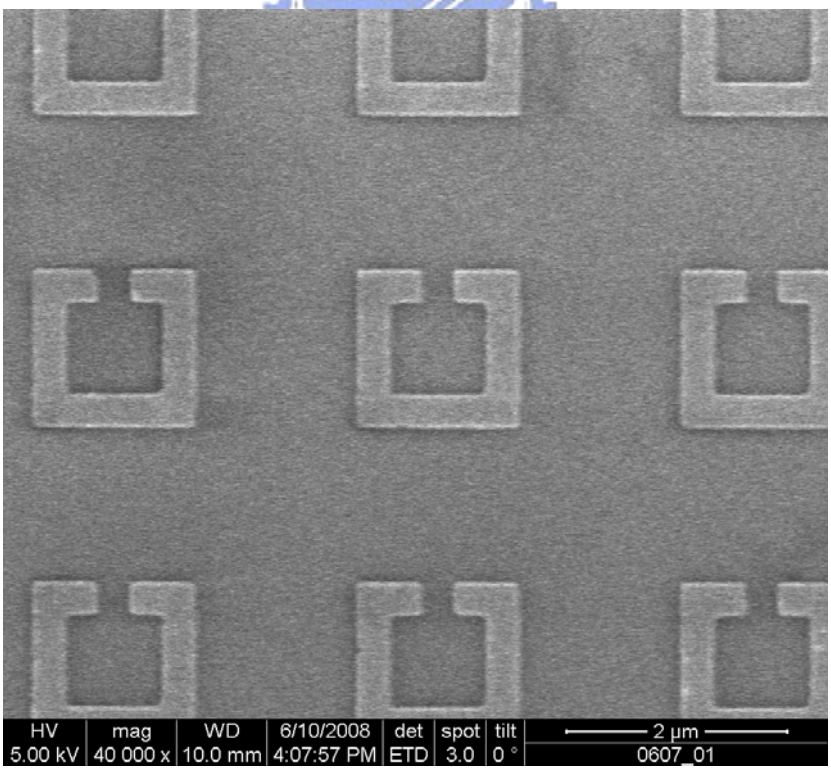

Figure 4-18 The SEM image of a SRR array after lift-off. Line width=300 nm, beam current=50 pA, field size=150 µm, dosage=0.85 µsec/dot, PR coating recipe (3).

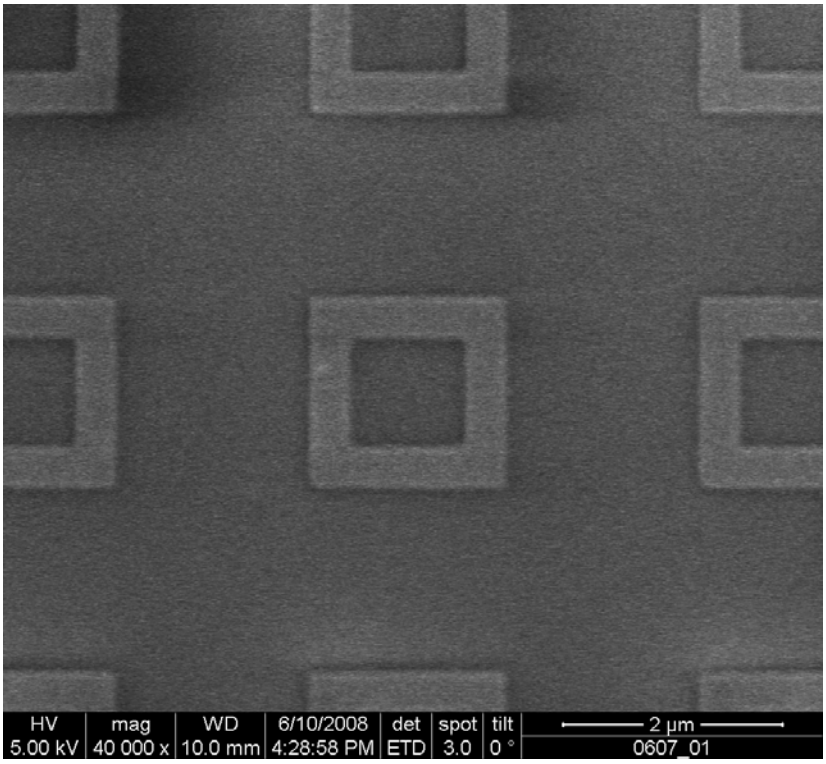

Figure 4-19 The SEM image of a CRR array after lift-off. Line width=360 nm, beam current=50 pA, field size=150 µm, dosage=0.85 µsec/dot, PR coating recipe (3).

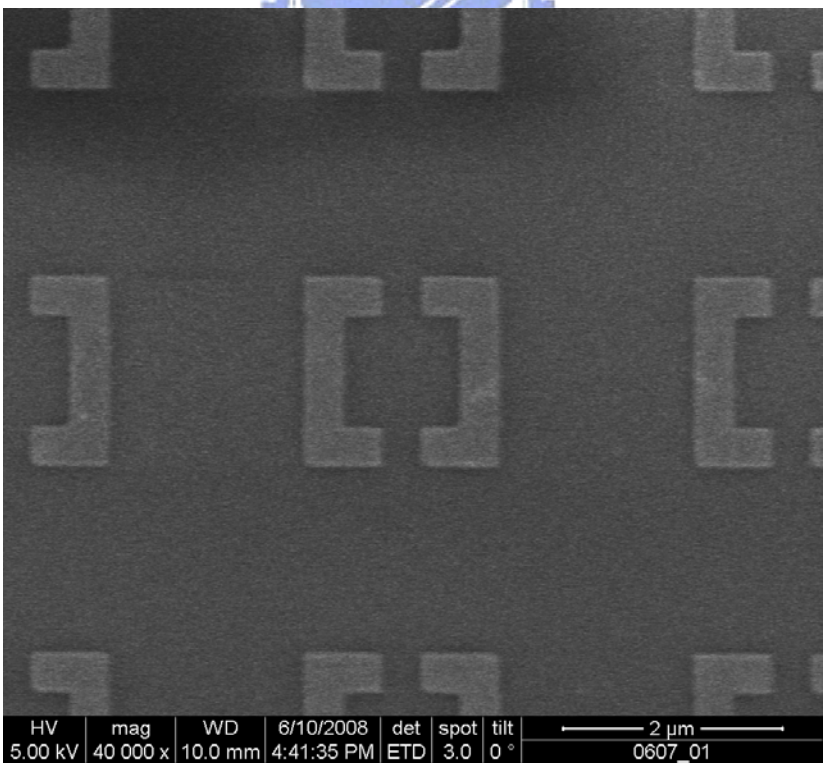

Figure 4-20 The SEM image of a 2-cut SRR array after lift-off. Line width=360 nm, beam current=50 pA, field size=150 µm, dosage=0.85 µsec/dot, PR coating recipe (3).

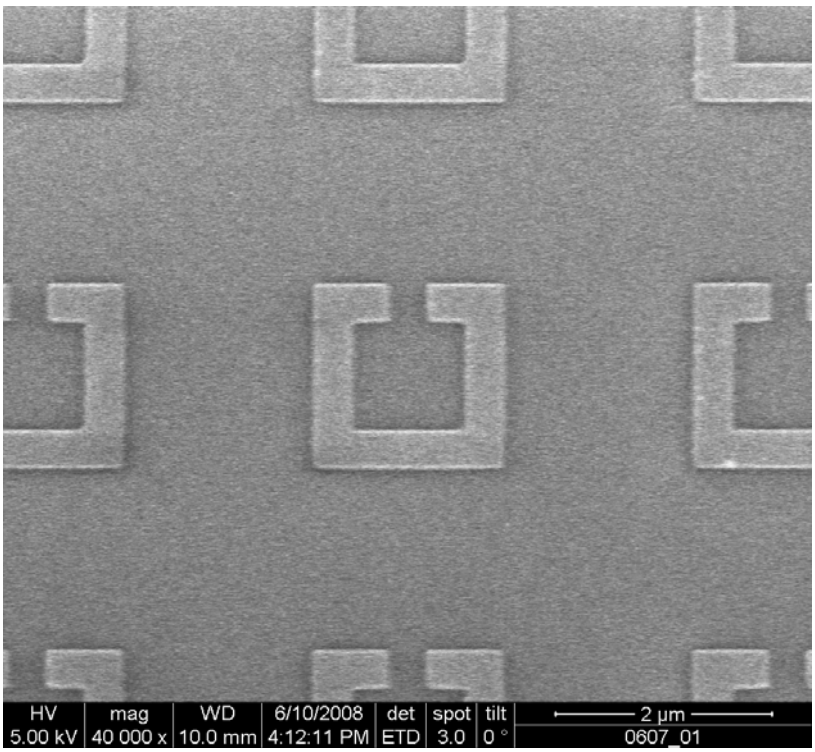

Figure 4-21 The SEM image of a SRR array after lift-off. Line width=360 nm, beam current=50 pA, field size=150 µm, dosage=0.85 µsec/dot, PR coating recipe (3).

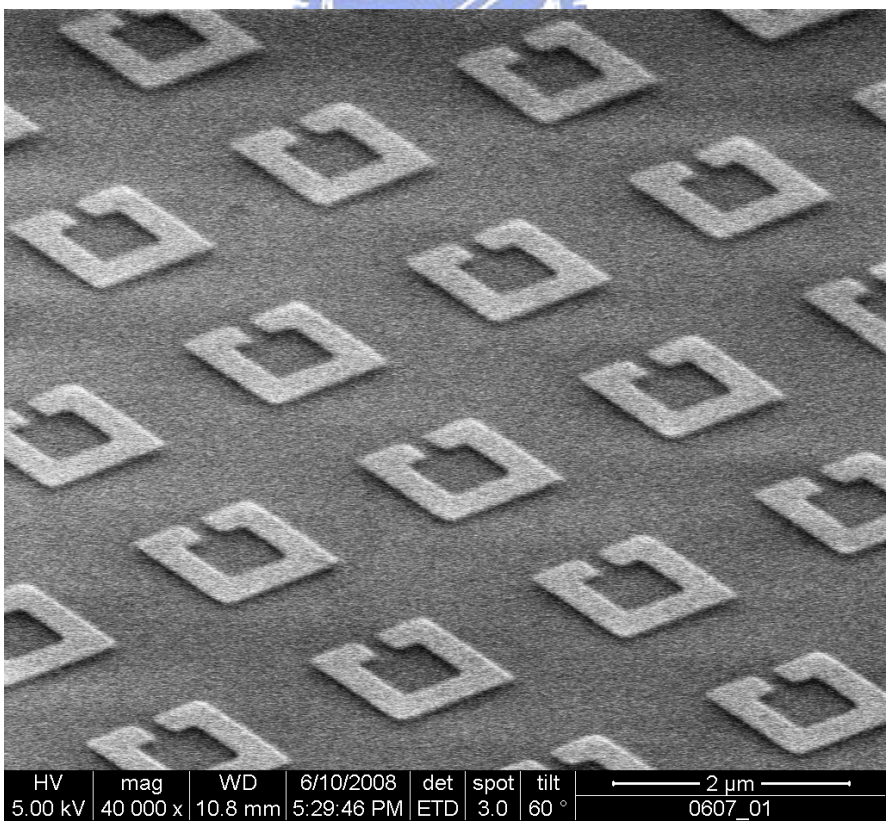

Figure 4-22 The 3D SEM image of a SRR array after lift-off. Line width=360 nm, beam current=50 pA, field size=150 µm, dosage=1.2 µsec/dot, PR coating recipe (3).

Chapter 5

Measurement and Results

5.1 Measurement

Most optic measurements of μm- or nm- scaled metamaterials were done by the FTIR (Fourier transform infrared spectrometer) [30, 36, 37, 38, 39]. In this thesis work, both reflection and transmission spectra of the specimens were measured carefully using the micro scoped-FTIR Hyperion 2000 manufactured by Bruker. The measurement range of this FTIR extends from k=370-25000 cm^{-1}, which covers the middle-infrared (MIR), near-infrared (NIR) and visible (VIS) region by using different beam splitter and detector materials listed in Table 5-1. The wavelengths and wave numbers specifying the three spectral ranges are listed in Table 5-2. The microscope provides optical image of the sample that allows the light to impinge on the desired area when the devices area was very small, for example, 90×90 μm^2 arrays in our experiment. Moreover, the Hyperion 2000 equips with a grazing incidence objective to allow the light impinged obliquely at a range of 52.2°-84.2° which is useful and convenient for reflection study. The light path of the grazing incidence objective is illustrated in Figure 5-1.

In Chapter 2, we introduced the four frequently studied orientation and polarization combinations of the SRR (Figure 2-5 that is presented here in Figure 5-2 again for convenience). Measurement geometries were designed to match these four types of combinations in Figure 5-3. Due to the mechanical limitation of our equipment,

in-plane incident is impossible. Instead, we used the grazing incidence objective to achieve horizontal quantity of the incident light and vertical quantity of the magnetic field (Figure 5-3 (a) and (b)). Polarization was set either 0° or 90° to fulfill the required direction of the electric field. Owing to the weak signal achieved by the grazing incidence objective, the measurement conditions were set differently for

Table 5-1 Beam splitter and detector materials used in Hyperion 2000 FTIR.

	beam splitter	detector
MIR	KBr	MCT/DLaTGS
NIR	CaF_2	InGaAs diode
VIS	quartz	Si Diode

Table 5-2 The wavelengths and wave numbers specifying the NIR, MIR, and VIS spectral ranges. Most of the present spectral analysis are located in the range k=4000-400cm^{-1}, i.e., the MIR region.

	λ(μm)	k(cm^{-1})
MIR	2.5-50	4000-200
NIR	0.78-2.5	12800-4000
VIS	0.4-0.7	25000-14300

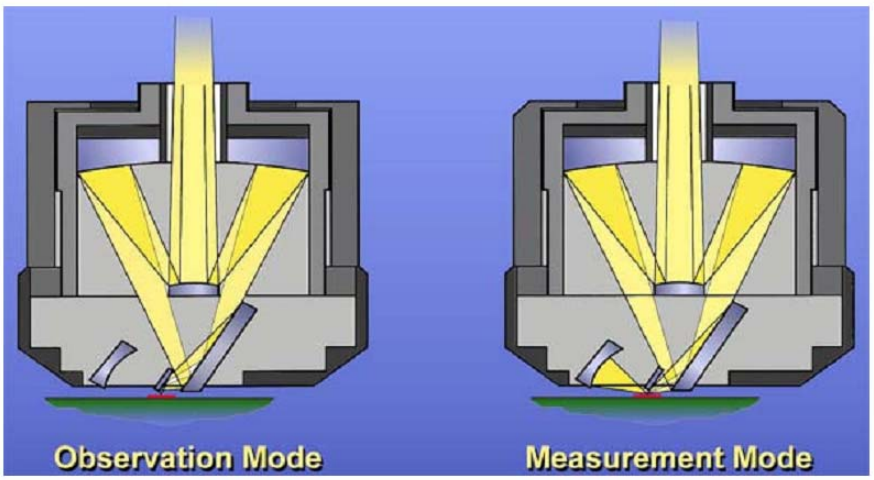

Figure 5-1 The light path of the grazing incidence objective in Hyperion 2000.

Table 5-3 Measurement conditions

	vertical incidence	oblique incidence
aperture	1.5 (mm)	8 (mm)
resolution	4 (cm^{-1})	8 (cm^{-1})
scan time	32 (time)	64 (time)

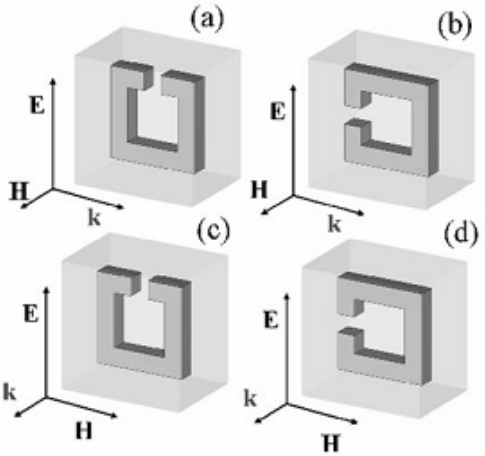

Figure 5-2 SRR in the four nontrivial EM field propagation directions and polarizations. The figure is imaged from [36].

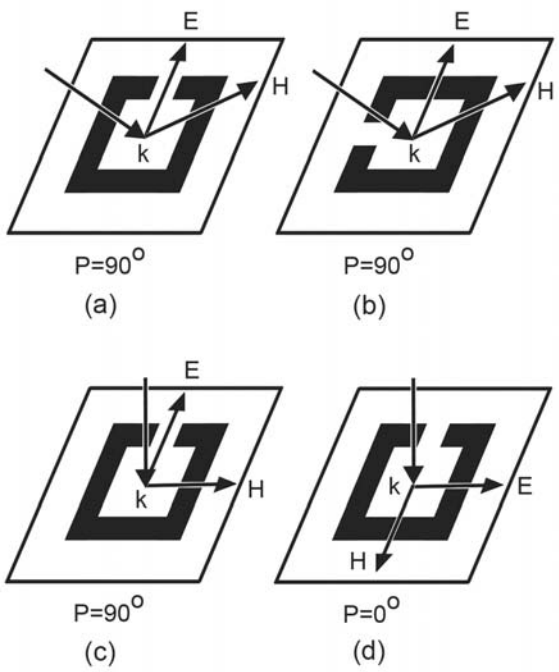

Figure 5-3 Measurement geometries that correspond to the four combinations in Figure 5-2, accordingly. Reflection was measured through (a)-(d), while transmission was measured only for (c) and (d).

oblique and vertical incidence as listed in Table 5-3. Despite the aperture set, the measurement window was narrowed down to approximately the array size, i.e. 90 μm, for both oblique and vertical incidence. Transmission measurements were done only for geometries (c) and (d) since it is not available for oblique incidence using our equipment.

5.2 Analysis procedure

Because the intensity of the incident light varies with the impinging and polarization angles, there is a need to calibrate and normalize the measured signal intensity, in order to facilitate a unified comparison among various spectra. This was done by drawing a slope from the lowest point to the highest point for each spectrum. The lower intensity then can be compared to the higher intensity with a meaningful reference.

To highlight the spectral features that are caused by interactions between the incident light and the patterns, the measured spectrum were divided by the background spectrum. The background of the reflectance was a gold-coated reference specimen, while the background of the transmittance was the glass located outside the patterned region. The reflection/ transmission spectra that have been normalized and divided by the proper background spectra are called normalized reflectance/ transmittance.

Expected EM responses for the three types of ring resonator patterns under different measurement geometries are listed in Table 5-4. The main factor that influences the response of the resonators is whether the magnetic field is perpendicular or parallel to the pattern surface. Another factor is the orientation of the pattern, i.e. the gap-bearing side of the resonators, with respect to the electric field.

Table 5-4 Expected responses for the three types of ring resonators, i.e., SRR, CRR, and 2-cut SRR, under the four measurement geometries depicted in Figure 5-2 and Figure 5-3. E stands for the electric resonance, M stands for the magnetic resonance and C stands for the electric coupling effect.

	(a)	(b)	(c)	(d)
SRR	E/M	E/M/C	E	E/C
CRR	E	E	E	E
2-cut SRR	E/M	E/M	E	E

5.3 Results and Discussion

The measurements were essentially carried out twice for each of the three samples, and the obtained spectra are rather identical, indicating a good experimental reproducibility. Figure 5-4 shows the normalized transmittance of the SRR array for geometry (c). The transmission dips correspond to the peaks of the normalized reflectance for the same SRR array and measurement geometry shown in Figure 5-7, while strong absorption occurred for frequency below about 60 THz. This might be a transmission property of the Conning glass wafer, namely, the glass is opaque for part of the MIR region. The expected magnetic resonance wavelength 6-18 μm, i.e. 16-50 THz in frequency, was blocked by this substrate absorption. Thus, we will present only the normalized reflectance spectra in the following discussion.

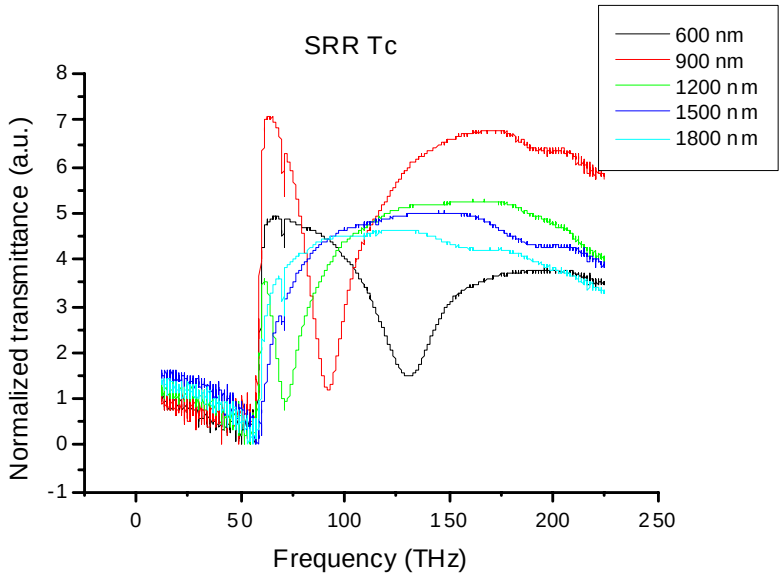

Figure 5-4 Normalized transmittance of the SRR array for geometry (c).

Figure 5-5 to 5-8 show the normalized reflectance of the SRR array for the four measurement geometries. For all measurement geometries, there is a reflection band from 24 to 36 THz, while at higher frequency, another reflection peak can be clearly seen and has a blue shift as the unit cell size decreases. Some of the reflection peaks split especially for small unit cell size (600nm and 900nm) and for oblique incidence ((a) and (b)). This might be due to the incapability of the machine to cover the entire spectral region smoothly. The orientation of the electric field influences the reflection spectra by changing the spectral configuration which can be seen when comparing (a) and (b) or (c) and (d). When the electric field was parallel to the gap-bearing side of the SRR, the reflection peak shifted to higher value.

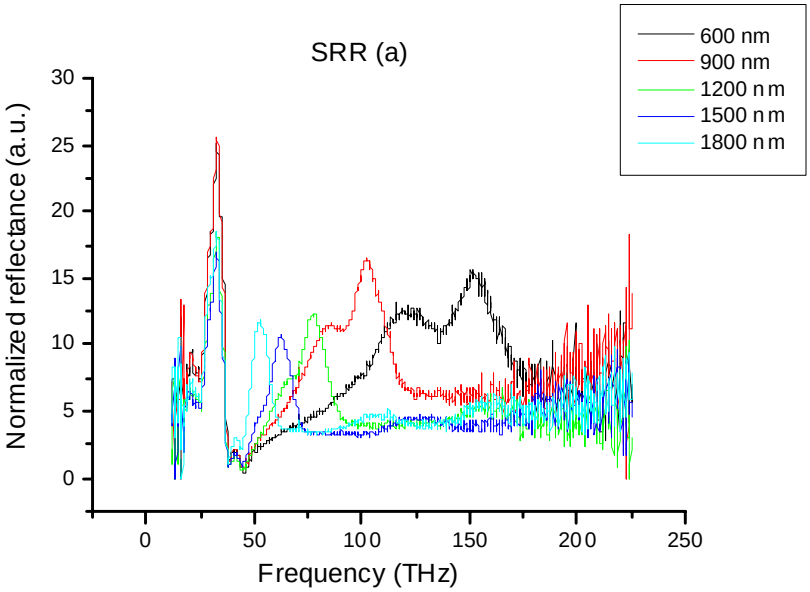

Figure 5-5 Normalized reflectance of the SRR array for geometry (a).

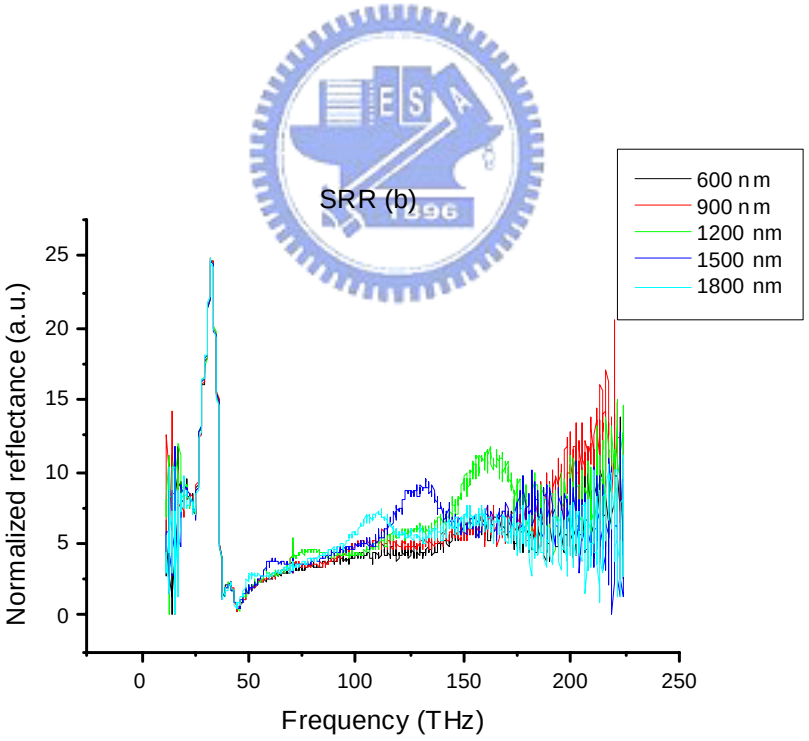

Figure 5-6 Normalized reflectance of the SRR array for geometry (b).

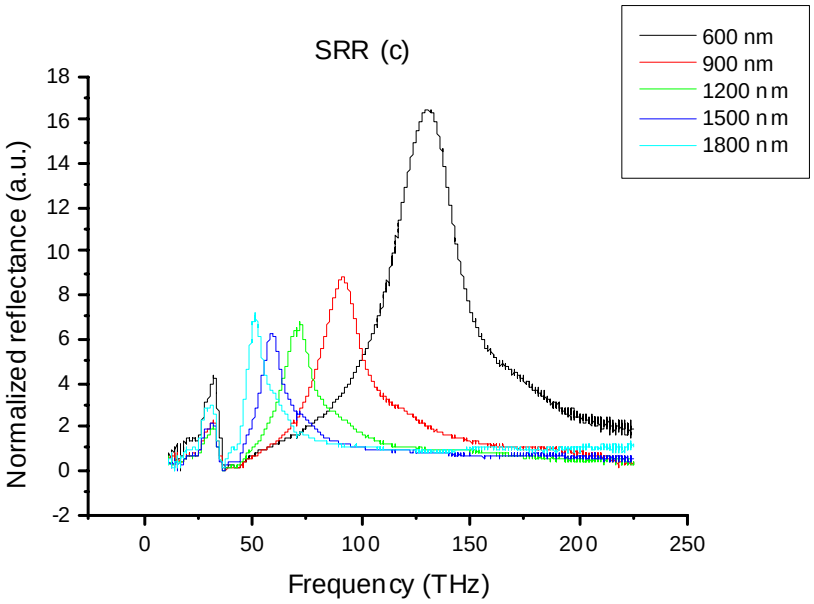

Figure 5-7 Normalized reflectance of the SRR array for geometry (c).

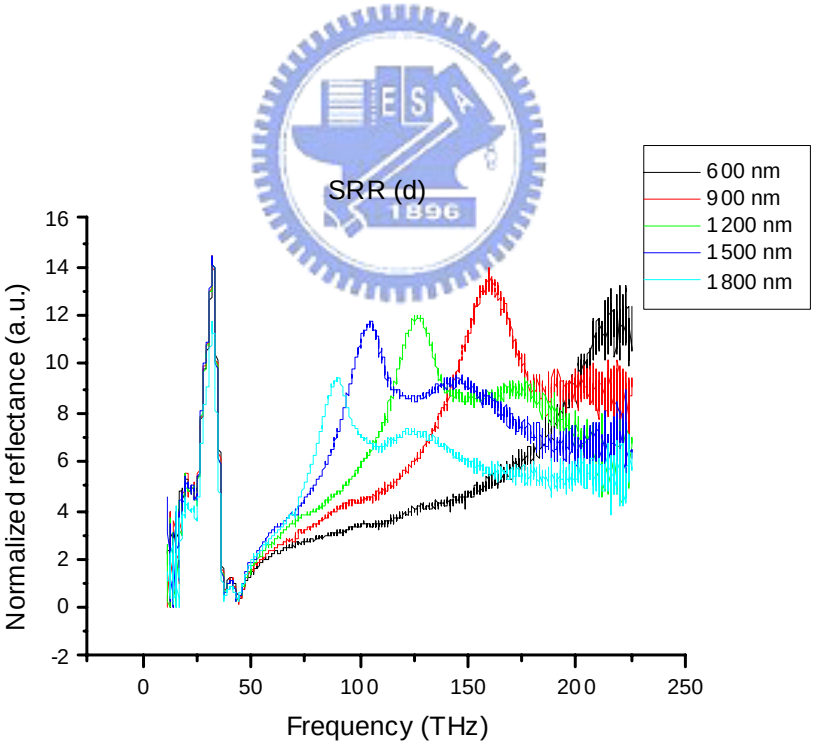

Figure 5-8 Normalized reflectance of the SRR array for geometry (d).

Figure 5-9 to 5-12 show the normalized reflectance of the CRR array for the four measurement geometries. Again, the reflection band between 24-36 THz is fixed in all measurement geometries. The reflection spectra of the CRR array are quite similar to that of the SRR array for geometry (a) and (c), while there is almost no difference between (a) and (b) or (c) and (d) which implies that the orientation of the electric field does not affect the EM response of the CRR array. This is reasonable and expected since the CRR is symmetric. Because the CRR does not have a capacitance, it is assumed to exhibit only the electric response. And since the spectrum of the CRR array for geometry (a) does not remove any peak when comparing with that of the SRR array, one may conclude that the reflection peaks occur beyond 50 THz should be an electric response rather than a magnetic one.

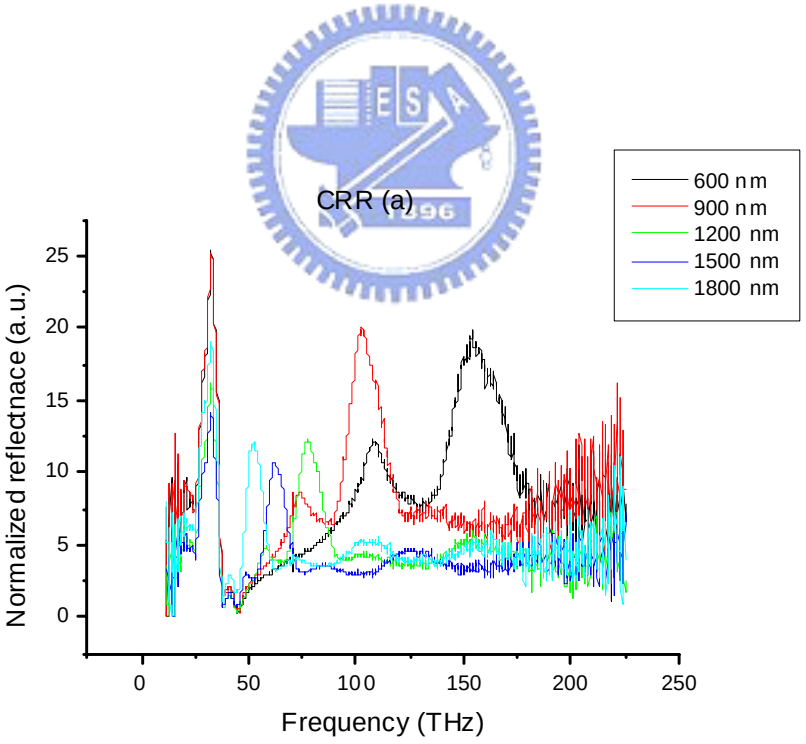

Figure 5-9 Normalized reflectance of the CRR array for geometry (a).

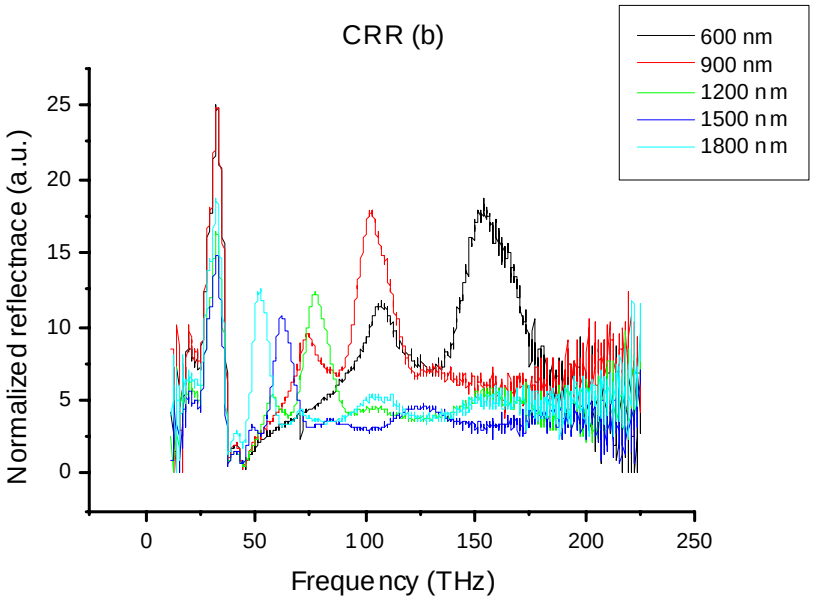

Figure 5-10 Normalized reflectance of the CRR array for geometry (b).

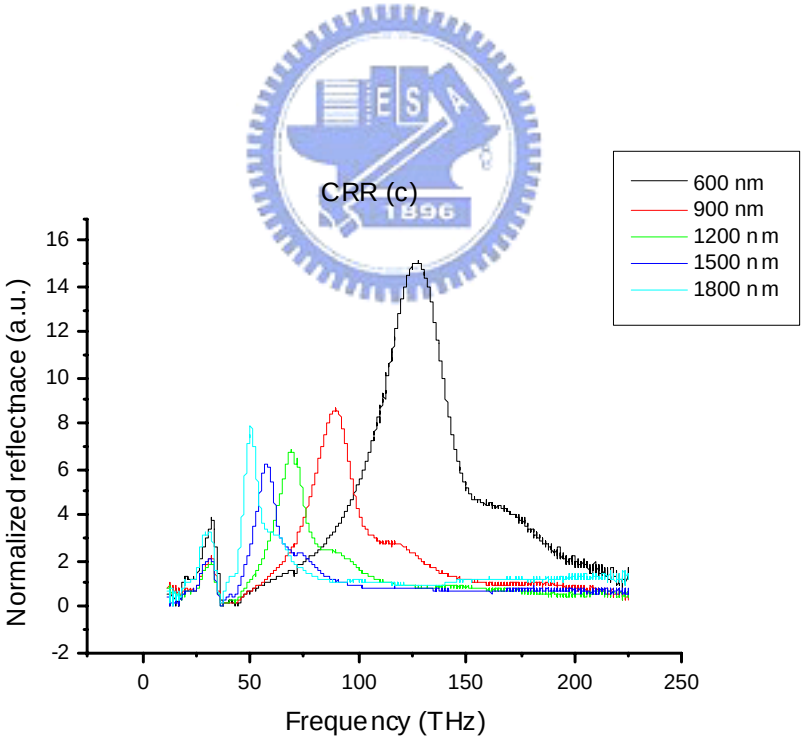

Figure 5-11 Normalized reflectance of the CRR array for geometry (c).

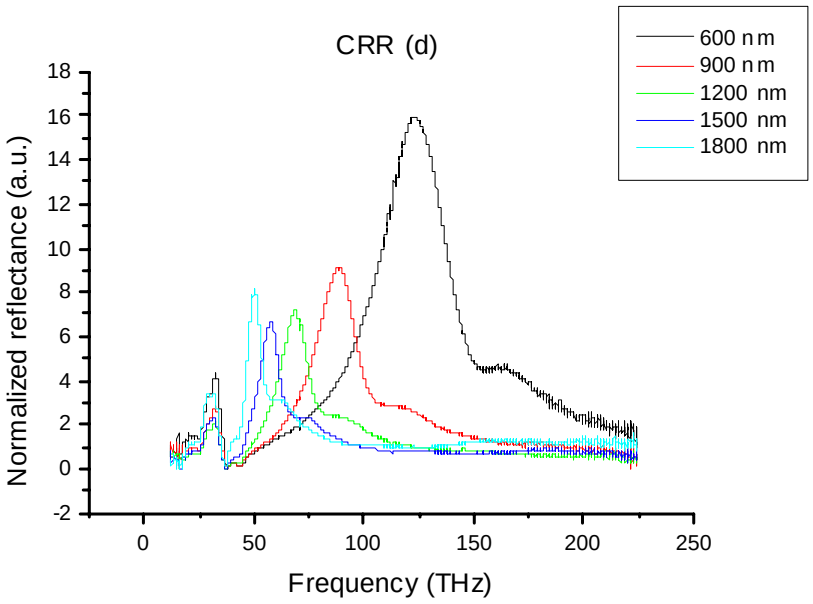

Figure 5-12 Normalized reflectance of the CRR array for geometry (d).

Figure 5-13 to 5-16 show the normalized reflectance of the 2-cut SRR array for the four measurement geometries. The fixed 24-36 THz reflection band is consistent with the previous SRR and CRR case. We may conclude that this unwanted reflection band is due to the feature of the glass substrate. The spectra for geometry (a) and (c) are also similar to that of the SRR and CRR, while in (b) and (d), the spectra vary in a different way from that of the SRR. In a nut shell, the three patterns show finger print spectra result for geometry (b) and (d).

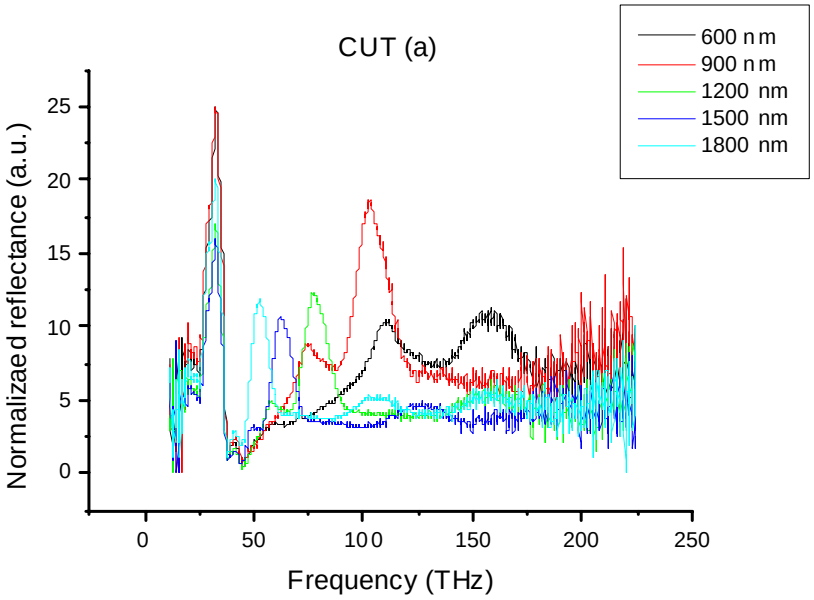

Figure 5-13 Normalized reflectance of the 2-cut SRR array for geometry (a).

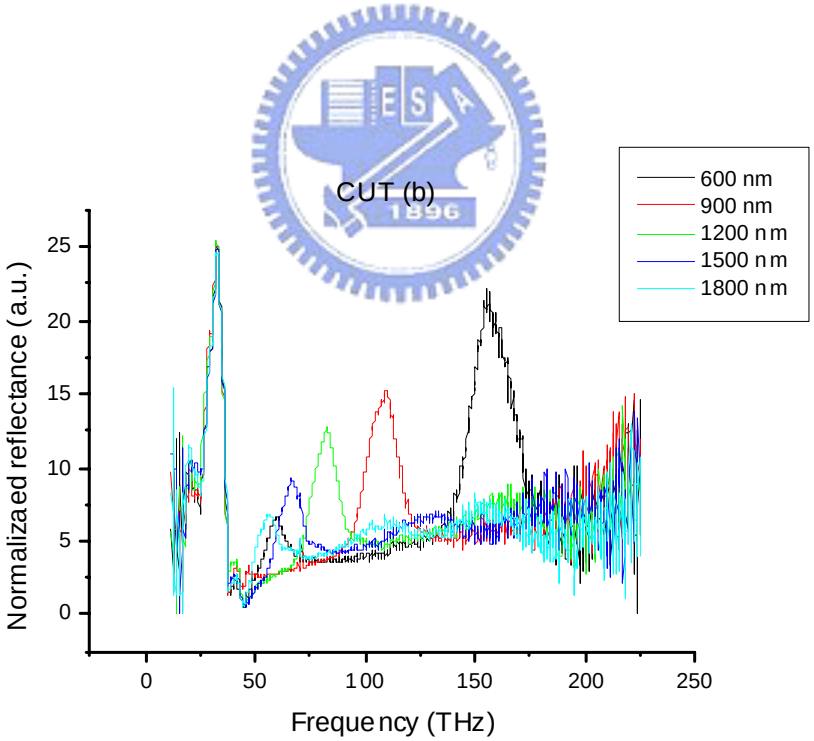

Figure 5-14 Normalized reflectance of the 2-cut SRR array for geometry (b).

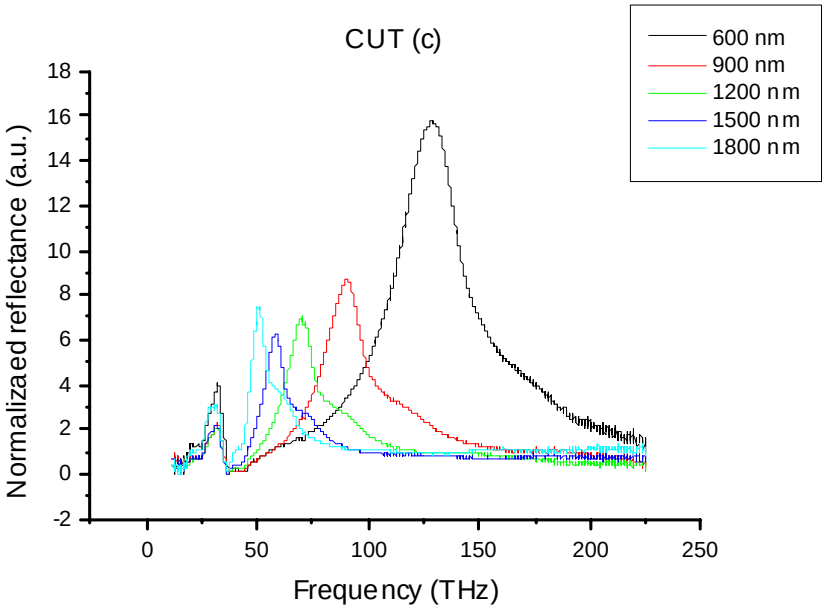

Figure 5-15 Normalized reflectance of the 2-cut SRR array for geometry (c).

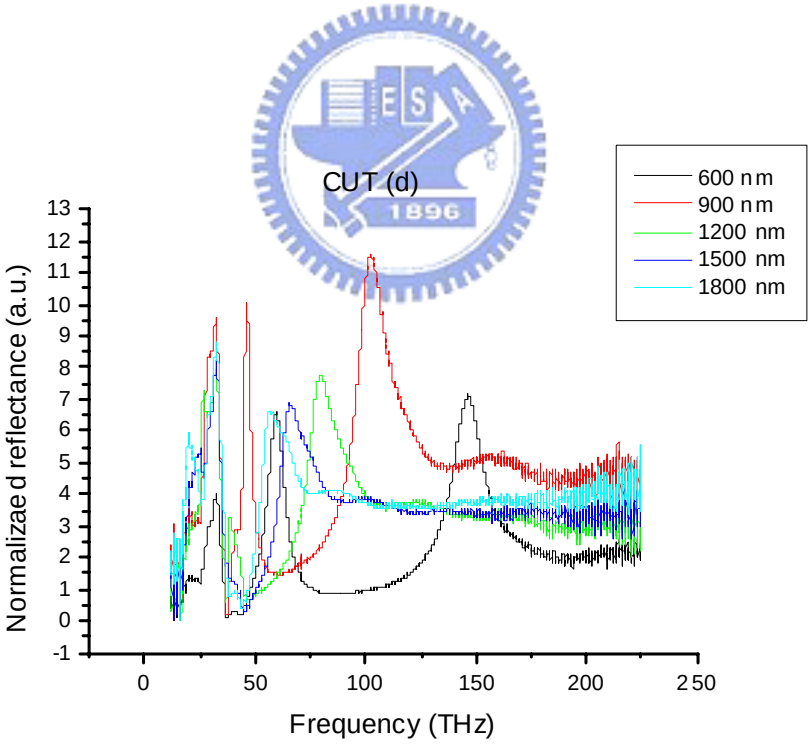

Figure 5-16 Normalized reflectance of the 2-cut SRR array for geometry (d).

To examine the scaling of the EM response with the unit cell size, the electric resonance wavelength (and its corresponding frequency and wave number) of the five SRR unit cell sizes measured from geometry (c) are listed in Table 5-5 and the λ_p–a relation is plotted in Figure 5-17 which shows a nearly linear scaling. Here we are unable to draw the scaling of the magnetic response since it was not observed in our measurement results.

Table 5-5 The numeral data of the electric response wavelength and corresponding frequency and wave number for different unit cell sizes.

a (nm)	λ_p (μm)	f_p(THz)	k_p (cm^{-1})
600	2.37635	126.24383	4208.12764
900	3.33239	90.02539	3000.84629
1200	4.17825	71.80045	2393.34849
1500	5.06863	59.18764	1972.92144
1800	5.79352	51.78196	1726.06519

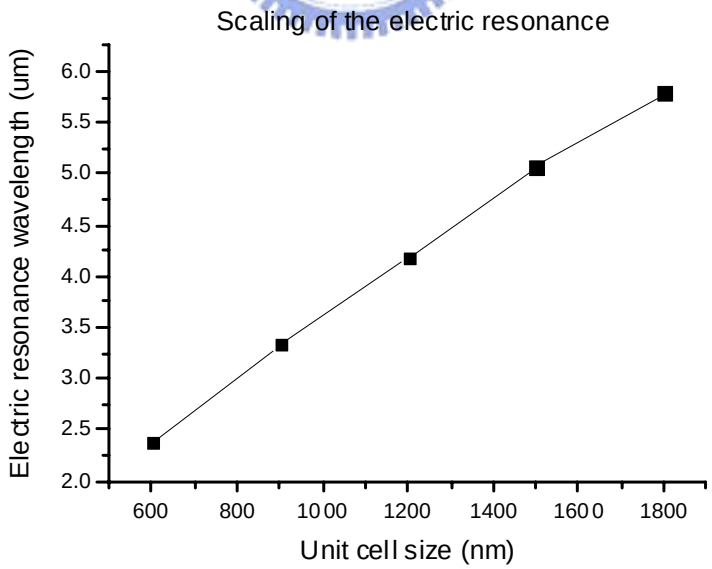

Figure 5-17 The scaling of the electric response wavelength with unit cell size for the SRR array measured by geometry (c).

To reveal the influence of the electric field orientation on the reflection spectrum, the measured spectra of geometry (a) and (b) were plotted in the same graph, while those of (c) and (d) were plotted in another one, i.e., with the same polarization but different beam impinging azimuths for comparison. Figure 5-18 summarizes the spectra of the three patterns for the smallest unit cell size, 600 nm. It can be clearly seen that the spectra of the CRR were not affected by the ***E*** orientation, while for SRR and 2-cut SRR, the electric resonance peaks shift to higher value in geometry (b) and (d). The degree of shift is larger for the SRR than that for the 2-cut SRR. This is expected since the 2-cut SRR is more symmetric than the SRR (but not as symmetric as the 4-cut SRR), it should be able to reduce, if not remove, the electric coupling effect. Namely, the electric resonance peaks are less influenced by the ***E*** orientation for more symmetric ring resonators. However, the reflection peak near the magnetic resonance frequency induced by the electric coupling effect was not observed in our measurement results except for the smallest 2-cut SRR where an additional reflection peak at about 60 THz occurred as shown in Figure 5-18 (F). One possible reason may be that the magnetic response frequency is smaller than expected, so only the peak of the smallest 600nm 2-cut SRR (which has smaller capacitance and thus higher magnetic response frequency then the 600 nm SRR) can survive the blocked region of the spectra. For the 900 nm 2-cut SRR, a secondary reflection peak is also observable at about 46 THz as shown in Figure 5-19.

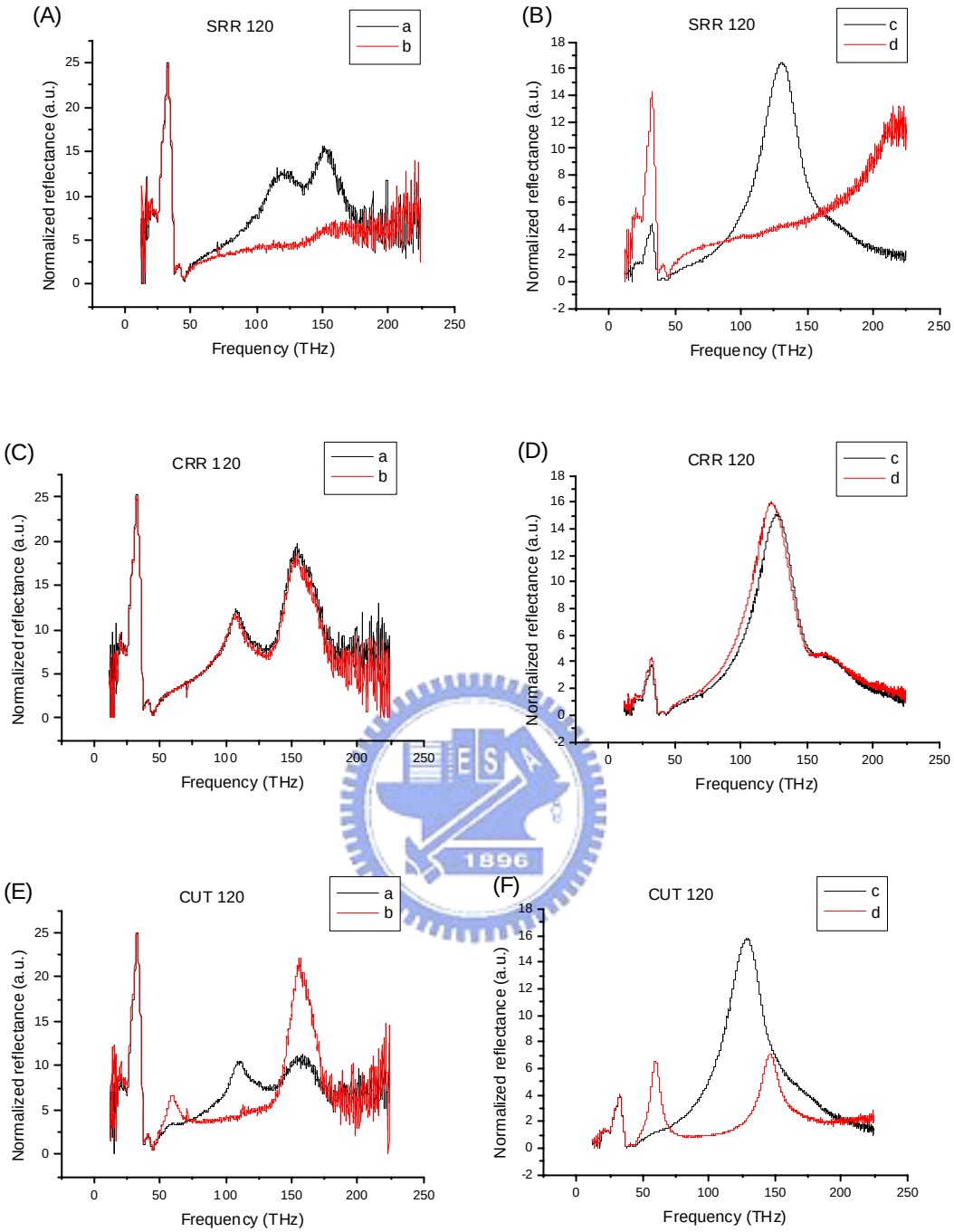

Figure 5-18 Comparison of the normalized reflectance for the (A) SRR arrays in geometry (a) and (b), (B) SRR arrays in geometry (c) and (d), (C) CRR arrays in geometry (a) and (b), (D) CRR arrays in geometry (c) and (d), (E) 2-cut SRR arrays in geometry (a) and (b), and (F) 2-cut SRR arrays in geometry (c) and (d). The unit cell size is 600nm.

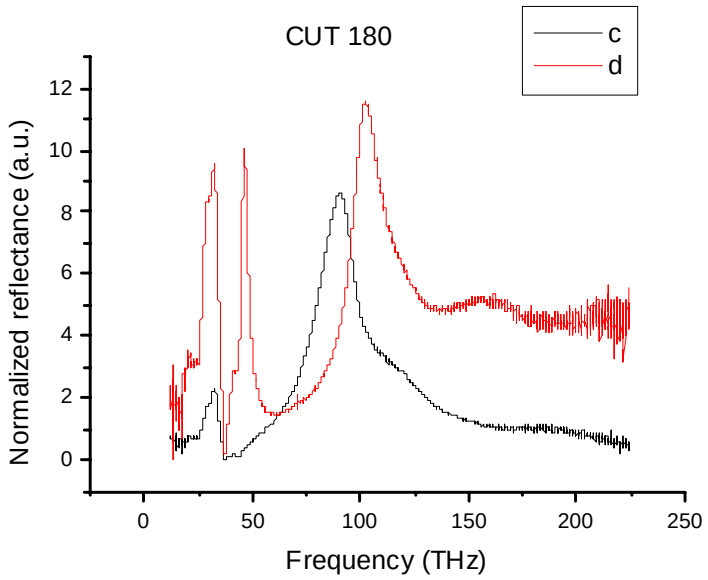

Figure 5-19 Comparison of the normalized reflectance for the 2-cut SRR arrays in geometry (c) and (d). The unit cell size is 900nm.

Chapter 6

Conclusion

Meta-materials were studied in this thesis work because of their resonance features. Three types of ring resonators: SRR, CRR, and 2-cut SRR were designed with five unit cell sizes, ranging from 600 nm to 1800 nm. The success in fabrication of Au pattern arrays indicates the feasibility to make nano-scaled gold devices on the glass substrate using the e-beam lithography together with the lift-off technique.

Optical measurements were carried out using the microscoped-FTIR for four nontrivial geometries. The magnetic resonance was not observed due to the overlapping of the interested frequency region with the substrate absorption, i.e. Si-O bond vibration, around 10 μm. This implies that glass may not be a suitable substrate for optical studies at the MIR region.

However, the electric resonance of these patterns showed clear trends with reproducibility. First, the electric resonance frequency was influenced by the orientation of the resonators with respect to the electric field. When the electric field is parallel to the non-gap-bearing sides of the resonators, the reflection spectra were similar for SRR, CRR, and 2-cut SRR. In contrast, when the electric field is parallel to the gap-bearing sides of the resonators, the reflection spectra of the three types of the resonators became different. The reflection spectra of the CRR remained almost unchanged while the electric resonance frequency shifted to much higher values for the SRR (blue shift). For 2-cut SRR, only slight shift of the peaks were observed

which implied that more symmetric resonators can effectively reduce the electric coupling effect. On the other hand, a linear scaling of the electric resonance with the unit cell size has been observed.

In order to demonstrate both electric and magnetic response of the ring resonators, it is useful to utilize different ring resonator designs with various unit cell sizes and measure the optical features for all possible geometries that induce the EM response and cross-check the spectra.

To study the magnetic resonance of the ring resonators at 10 μm, either the glass substrate should be replaced or the unit cell size should be tuned. Simulations prior to the experiment by CST Microwave Studio, a state-of-the-art electromagnetic field solver [1, 2, 25, 37, 43], will provide useful information and physic insights that may help and allow more reasonable design of the device. In the future, to adhere bio-molecules such as proteins with or without metallic ions or certain DNA sequences on the metal resonators is of interest to study how these bio-matters would perturb and alter the EM responses, which maybe an enabled technique for bio-sensing and manipulation.

Reference

[1] S. A. Ramamkrishna, “Physics of negative refractive index materials”, *Rep. Prog. Phys*., vol. 68, pp. 449-521, 2005

[2] V. G. Veselago, “Experimental demonstration of negative index of refraction”, *Sov. Phys. Usp.*, Vol. 10, pp. 509, 1968

[3] J. B. Pendry, “Negative refraction makes a perfect lens”, *Physical ReviewLletters*, vol. 85, no. 18, pp. 3966, 2000

[4] Stefan Linden, Christian Enkrich, Martin Wegener, Jiangfeng Zhou, Thomas Koschny, Costas M. Soukoulis, “Magnetic response of metamaterials at 100 terahertz”, *Science*, vol. 306, pp. 1351, 2004.

[5] J. B. Pendry, A. J. Holden, D. J. Robbins, W. J. Stewart, “Magnetism from conductors and enhanced nonlinear phenomena”, *IEEE Trans. Microwave Theory Tech.*, vol. 47, pp. 2075, 1999

[6] D. Smith, W. Padilla, D. Vier, S. Nemat-Nasser, S. Schultz, ”Composite medium with simultaneously negative permeability and permittivity”, *Physical Review Letters*, vol. 84, pp. 4184, 2000

[7] C. G. Parazzoli, R. B. Greegor, K. Li, B. E. C. Koltenbah, and M. Tanielian, “Experimental verification and simulation of negative index of refraction using Snell’s law”, *Physical Review Letters*, vol. 90, no. 10, pp. 107401, 2003

[8] Andrew A. Houck, Jeffrey B. Brock, and Isaac L. Chuang, “Experimental observations of a left-handed material that obeys Snell’s law”, *Physical Review Letters*, vol. 90, no. 13, pp. 137401, 2003

[9] D. R. Smith, S. Schultz, P. Markos, C. M. Soukoulis, ”Determination of effective permittivity and permeability of metamaterials from reflection and transmission coefficients”, *Physical Review B*, vol. 65, pp. 5, 2002

[10] D. R. Smith, D. C. Vier, T. Koschny, C. M. Soukoulis, “Electromagnetic parameter retrieval from inhomogeneous metamaterials”, *Physical Review E*, vol. 71,

pp. 617, 2005

[11] T. Koschny, P. Markos, E. N. Economou, D. R. Smith, D. C. Vier, C. M. Soukoulis, ”Impact of inherent periodic structure on effective medium description of left-handed and related metamaterials”, *Physical Review B*, vol. 71, pp. 22, 2005

[12] T. Koschny, P. Markos, D. R. Smith, C. M. Soukoulis, “Resonant and antiresonant frequency dependence of the effective parameters of metamaterials”, *Physical Review E*, vol. 68, pp. 065602, 2003

[13] K. Aydin, E. Ozbay, “Identifying magnetic response of split ring resonators at microwave frequencies”, *Opto-electron Review*, vol. 14, no. 3, pp. 193-199, 2006

[14] M. Zahn, “Electromagnetic field theory”, *John Wiley and Sons*, pp. 343, 1979

[15] F. W. Grover, “Inductance calculation, working formulas and tables”, *Dover*, pp. 35, 1946

[16] H. A. Wheeler, “Transmission-line properties of parallel strips separated by a dielectric sheet”, *IEEE Trans. Microwave Theory Tech.*, MTT 13, pp. 172, 1965

[17] K. Aydin, I. Bulu, K. Guven, M. Kafesaki, C. M. Soukoulis, E. Ozbay, “Investigation of magnetic resonances for different split-ring resonator parameters and designs”, *New Journal of Physics*, vol. 7, no.1, pp. 168, 2005

[18] Ilya V. Shadrivov, Steven K. Morrison and Yuri S. Kivshar, “Tunable split-ring resonators for nonlinear negative index metamaterials”, *Optics Express*, vol. 14, no. 20, pp. 9344, 2006

[19] N. Katsarakis, T. Koschny, M. Kafesaki, “Electric coupling to the magnetic resonance of split ring resonators”, *Applied Physics Letters*, vol. 84, pp. 2943-2945, 2004

[20] M. Kafesaki, T. Koschny, R. S. Penciu, T. F. Gundogdu, E. N. Economou, C. M. Soukoulis, “Left-handed metamaterials: detailed numerical studies of the transmission properties”, *Journal of Optics A: Pure and Applied Optics*, vol. 7, pp. S12, 2005

[21] Ricardo Marques, Francisco Medina, Rachid Rafii El Idrissi, “Role of

bianisotropy in negative permeability and left-handed metamaterials", *Physical Review B*, vol. 65, no. 144440, 2002

[22] V. D. Lam, J. B. Kim, S. J. Lee, D. F. Wang , Y. P. Lee, "Experimental observation of the electric coupling effect in split ring resonators and the prevention", *Phys. Stat. Sol*., vol. 204, pp. 3975, 2007

[23] N. P. Johnson, A. Z. Khokhar, H. M. H. Chong, R. M. DeLaRue, S. McMeekin, "Characterization at infrared wavelengths of metamaterials formed by thin-film metallic split-ring resonator arrays on silicon", *Electronics Letters*, vol. 42, no. 19, 2006

[24] T. Koschny, M. Kafesaki, "Effective medium theory of left-handed materials", *Physical Review Letters*, vol. 93, no. 10, 2004

[25] Philippe Gay Balmaz, Olivier J. F. Martin, "Electromagnetic resonances in individual and coupled split-ring resonators", *Journal of Applied Physics*, vol. 92, pp. 2929, 2002

[26] K. Aydin, K. Guven, "Effect of disorder on magnetic resonance band gap of split ring resonator structures", *Optics Express*, vol. 12, pp. 5896, 2004

[27] Jiangfeng Zhou, Thomas Koschny, Costas M. Soukoulis, "Magnetic and electric excitations in split ring resonators", *Optics Express*, vol. 15, pp. 17881, 2007

[28] Hongsheng Chen, Lixin Ran, Jiangtao Huangfu, Xianmin Zhang, Kangsheng Chen, Tomasz M. Grzegorczyk, Jin Au Kong, "Left handed materials composed of only S-shaped resonators", *Physical Review Letters* , vol. 70, no. 057605, 2004

[29] J. Zhou, T. Koschny, L. Zhang, G. Tuttle, and C. M. Soukoulis, "Experimental demonstration of negative index of refraction", *Appl. Phys. Lett*., vol. 88, no. 221103, 2006

[30] Atsushi Ishikawa, Takuo Tanaka, Satoshi Kawata, "Magnetic excitation of magnetic resonance in metamaterials at far infrared frequencies", *Applied Physics Letters*, vol. 91, no. 113118, 2007

[31] J. Zhou, L. Zhang, T. Koschny, G. Tuttle, and C. M. Soukoulis, "Negative index

materials using simple short wire pairs", *Phys. Rev. B*, vol. 73, no. 041101(R), 2006

[32] Z. G. Dong, S. Y. Lei, Q. Li, M. X. Xu, H. Liu, T. Li, F. M. Wang, and S. N. Zhu, "Non-left-handed transmission and bianisotropic effect in a π-shaped metallic metamaterial", *Phys. Rev. B*, vol. 75, no. 075117, 2007

[33] Atsushi Ishikawa, Takuo Tanaka, "Negative magnetic permeability of split ring resonators in the visible light region", *Optics Communications*, vol. 258, pp. 300-305, 2006

[34] J. Zhou, T. Koschny, M. Kafesaki, E. N. Economou, J. B. Pendry, C. M. Soukoulis, "Saturation of the magnetic response of split ring resonators at optical frequencies", *Physical Review Letters*, vol. 95, no. 223902, 2005

[35] A. C. Hsu, Y. K. Cheng, K. H. Chen, J. L. Chern, S. C. Wu, C. F. Chen, H. Chang, Y. H. Lien, J. T. Shy, "Far-infrared resonance in split ring resonators", *Japanese Journal of Applied Physics*, vol. 43, pp. 176, 2004

[36] N. Katsarakis, G. Konstantinidis, A. Kostopoulos, R. S. Penciu, T. F. Gundogdu, M. Kafesaki, E. N. Economou, Th. Koschny, C. M. Soukoulis, "Magnetic response of split ring resonators in the far-infrared frequency regime", *Opt. Lett.*, vol. 30, pp. 1348, 2005

[37] S. C. Wu, "Optical behaviors studying in nano-scale left-handed metamaterial patterns", *5th IEEE Conference on Nanotechnology*, vol. 1, pp. 421, 2005

[38] H. O. Moser, B. D. F. Casse, O. Wihelmi, B. T. Saw, "Terahertz response of a microfabricated rod-split-ring-resonator electromagnetic metamaterial", *Physical Review Letters*, vol. 94, no. 063901, 2005

[39] T. J. Yen, W. J. Padilla, N. Fang, D. C. Vier, D. R. Smith, J. B. Pendry, D. N. Basov, X. Zhang, "Terahertz magnetic response from artificial materials", *Science*, vol. 303, pp. 1494, 2004

[40] R. A. Shelby, D. R. Smith, S. Schultz, "Experimental verification of a negative index of refraction", *Science*, vol. 292, pp. 77, 2001

Vita

Min-chen Wu was born in Hsinch, Taiwan on October 26th, 1983. She received the B.S. degree in the Electronics Engineering Department from National Chiao Tung University (NCTU) in June, 2006. She entered the Institute of Electronics, National Chiao Tung University (NCTU) in September, 2006. Her major research interests are focused on nanotechnology, meta-materials and bio-sensing. She received the M.S. degree from NCTU in July 2008.